Formation and dynamics of defects in pure and ion implanted α-Titanium studied by quantum simulations

Abdulrafiu Tunde Raji

UCT, 2010

Formation and dynamics of defects in pure and ion implanted α-Titanium studied by quantum simulations

Dissertation submitted to the University of Cape Town for the Degree of Doctor of Philosophy in Physics

Supervisors

Prof. David. T. Britton

Prof. Margit Härting

February 2010

Table of Contents

List of Publications

The thesis consists of overview and the following publications:

1. *Ab initio* pseudopotential study of vacancies and self-interstitials in hcp titanium, A. T. Raji, S. Scandolo, R. Mazzarello, S. Nsengiyumva, M. Härting, D. T. Britton, *Phil. Mag.* **89**, 1629 (2009).

2. *Ab initio* study of Kr in hcp Ti: diffusion, formation, and stability of small Kr-vacancy Clusters, A. T. Raji, S. Scandolo, R. Mazzarello, S. Nsengiyumva, M. Härting, D.T.Britton, *Nucl. Instrum. and Meth. in Phys. Res. B* **267,** 2991(2009).

3. Intrinsic defects and krypton impurity atoms in hcp-titanium: A first-principles study, A. T. Raji, R. Mazzarello, S. Scandolo, S.Nsengiyumva, M. Härting, D. T. Britton (*submitted to Physical Review B*).

4. Electronic structures of intrisic and krypton defects in h.c.p titanium from first principles, A. T. Raji, R. Mazzarello, S. Scandolo, S. Nsengiyumva, M. Härting, D. T. Britton (*Submitted to Solid State Communications*).

ABSTRACT

Density-functional theory calculations have been performed to study energetics of defects formation and diffusion in pure and krypton implanted hexagonal closed-packed (h.c.p) titanium. We employed the *ab initio* electronic structure calculations to study the formation energies of Ti vacancies and divacancies, Kr interstitials, and the binding of Kr atoms and Ti vacancies to form defect complexes. In addition, we present results on the diffusion of vacancies, divacancies, as well as the substitutional and interstitial krypton atom in h.c.p Ti. The calculated monovacancy formation energy is 1.97eV, which is in excellent agreement with other theoretical calculations, and agrees qualitatively with published experimental results. Two divacancy configurations have been shown to be equally stable, and the divacancy migration energy barrier is found to be lower than that of a monovacancy. Of the Ti interstitial configurations, the octahedral and basal-octahedral have relatively low formation energies and are, thus the most likely stable configurations. However, we found small energy differences between all of the configurations, suggesting their possible co-existence. The formation energies for the vacancy and self-interstitial are comparable. In addition, the migration energy barrier for diffusion of self-interstitial titanium atoms is lower than that of vacancies. This may suggest that self-diffusion in h.c.p Ti may be dominated by the interstitial mechanism. As for the incorporated Kr atoms, the substitutional Kr site is the most preferred, and the octahedral is the more stable of the two interstitial sites. Interstitial Kr atoms have been shown to have attractive interactions and a low migration barrier, suggesting that Kr bubble formation in the form of cluster is possible, even in the absence of vacancies. However, krypton clusters atoms are energetically unstable, until stabilized by an increasing number of vacancies.

CHAPTER 1

Introduction

The effects of energetic-particle irradiation on pure elements and alloys have received significant attention for decades because of its relevance in the development of fusion and fission reactors [*1,2*]. Most recent applications is the use of energetic rare gas atoms to manipulate directly the structure of solid at high pressures, and to induce nanoscale modifications that results in the stabilization of high-pressure phase at ambient conditions [*3,4*]. Ion implantation technique [*5*] is a common method of introducing foreign atoms in a material matrix. Depending on the material, many microstructural changes have been observed for implantation at ambient conditions. These include the creation of defects such as vacancies, interstitial atoms and their complexes [*6,7,8*], amorphization of host lattice structure [*9,10*], introduction of additional stresses [*11,12*], or crystalline-to-crystalline phase transitions [*13*].

Rare gas atoms are non-reactive with other elements, and when incorporated in metals via ion implantation, often cluster together in lattice defects to form nanometre-size precipitates (often referred to as solid inert gas bubbles) [*14,15*]. In order to characterise the structures and effects of noble gas inclusion, experimental techniques such as the electron microscopy [*16,17*], positron annihilation spectroscopy (PAS) [*18,19*], ion channelling method [*20*] and X-ray diffraction technique [*21,22*], are commonly used. In addition to experimental approaches, another means of understanding the properties of noble gas in metals is by computational simulations [*23*], especially at the atomic scale. Atomic-scale computation [*24*] provide an important method to gain insight into atomic-level processes, which would have been otherwise

difficult to identify from experiments, and which controls microstructural evolution and structural stability in materials [*25*]. For instance, the inherent limitations in spatial and time resolution of experimental techniques do not permit direct evidence of impurity diffusion paths [*26*], not to mention the difficulty associated with searching for transition states in solid state materials [*27*]. Computer simulations techniques are thus essential to obtain such data. With regards to noble-gas atoms in metals, there have been previous computational studies which employed empirical potentials (EPs) to determine interactions between the atoms. Notably, Anderman and Gehman [*28*] investigated the stability of xenon-vacancy clusters in copper and Rimmer and Cottrell [*29*] reported on the energetics of solution of inert gas atoms of krypton, neon and argon, also in copper. However, findings from empirical models often depend strongly on the potential used [*30,31*], and the reliability of such studies have been questioned in several studies [*32,33*]. Parameter-free, *ab initio* calculations are in principle more accurate [*34*], and can therefore provide reliable energetics of self- and foreign defects [*35,36*], as well as their complexes, in solids [*37*]. The impurity-defect energetics is of great importance since they can serve as inputs in more sophisticated models, in order to make quantitative predictions for the macroscopic properties of solids containing the impurity atoms [*38,39*]. *Ab initio* density functional theory (DFT) [*40*] studies on rare gas impurity atoms in metals have been reported in recent times. In particular, DFT studies on energetics of helium defects in metals [*41*], such as, α-Fe [*33,42*], Al [*43,44*], and W [*45*], have been reported.

Noble gas atoms inclusions in cubic metals have been extensively researched [*33,42-49*]. However, there have been rather few experimental [*50*] and theoretical investigations on hexagonal closed-packed (h.c.p) metals. Yet, electronic structures and physical properties of cubic and h.c.p metals, especially transition *d*- metal such as titanium, differ [*51,52*]. Thus,

further studies on rare gas atom in h.c.p metals are clearly necessary. Our research group is motivated partly by this, and partly because previous investigations [*53*,*54*] have shown that ion irradiation induces stress modification in solids. The displacement cascades triggered by the interaction of irradiated atoms with the host lattice results in the formation of many vacancies and interstitials, as well as the introduction of foreign implanted atoms at interstitial or substitutional positions. These defects play important role in modifying the pre-existing stress state in the implanted solid [*54*]. Thus, we recently started a programme to investigate, experimentally, the change in residual stress due to implanted krypton ions in h.c.p titanium [*54*], and also to study the different equilibrium point defect configurations resulting from the implantation. In this framework, and by using krypton incorporated in h.c.p titanium as our model system, we investigate the energetics of formation of simple point defects, such as the vacancy, divacancy, self- and foreign (krypton) impurity atoms, and their binding to form complexes. We also investigate the migration of the defects, in particular, the diffusion mechanisms governing the mobility of the implanted species. We focus on the atomic-scale calculations, in the framework of DFT using the plane wave pseudopotential (PP) approach [*55*].

The thesis is thus organized as follows: First, we present, in Chapter 2, theoretical concepts underlying much of the calculations. In Chapter 3, we present calculations on the physical and electronic properties of pure phase of α-Titanium as a step to ascertain the reliability of our pseudopotential and the exchange-correlation functional, and we compare our calculated parameters with other theoretical and experimental results. We then focus on the structure, energetics and the migration of simple point defects in titanium, using the supercell approach [*56*], in Chapter 4. In Chapter 5, possible krypton impurity sites in α-Titanium, its migration paths, the stability or binding of small interstitial krypton–vacancy complexes, as well as the

stability of clusters of substitutional krypton atoms and vacancies, are investigated. Important outcomes of this work are summarized in Chapter 6.

CHAPTER 2

Theoretical Concepts

2.1 Density functional theory (DFT)

Density functional theory (DFT) [*57*] addresses the problem of generating adequate representations of the electronic structure of atoms, molecules, and solids without explicit recourse to many-electrons wavefunctions. Instead, electron densities and first-order density matrices are used directly from ground state variational calculations [*58*]. DFT is based on the famous theorem of Hohenberg and Kohn [*59*] who demonstrated that the total energy, *E*, of an interacting non-spin polarised many-electron system in an external potential (such as Coulomb potential due to the nuclei of the solid) is a unique functional of the electron density, and that this functional has its minimum at the ground state electronic density, ρ_0, that is [*60*],

$$E = E[\rho_0]. \tag{2.1}$$

It was further shown that other ground state properties are also functionals of the ground state density. In electronic theory of solids, all the observables that can possibly be known about a given system are contained in the system's wavefunction, ψ. Therefore when solving the Schrödinger equation (SE), one specifies the system by choosing a potential $v\,(r)$, and then solves the equation for the wavefunction. The observables are determined by taking the expectation values of operators with respect to the wavefunction. Thus,

$$v\,(r) \rightarrow \psi(\boldsymbol{r_1}, \boldsymbol{r_2}, \boldsymbol{r_3}, \ldots \boldsymbol{r_N},) \rightarrow \langle\psi| \ldots |\psi\rangle \rightarrow \{\text{observables}\}, \tag{2.2}$$

where $\boldsymbol{r_1}$, $\boldsymbol{r_2}$, $\boldsymbol{r_3}$...$\boldsymbol{r_N}$ are electronic coordinates. One of the many observables that is calculated after obtaining the wave function is the particle density, $\rho(\boldsymbol{r})$, often expressed as

$$\rho(\boldsymbol{r}) = N \int d^3 r_2 \int d^3 r_3 \ldots \int d^3 r_N \, \psi^*(r_1, r_2, r_3 \ldots r_N)\psi(r_1, r_2, r_3 \ldots r_N). \quad (2.3)$$

Here, $\psi(\boldsymbol{r_1}, \boldsymbol{r_2}, \boldsymbol{r_3}, \ldots \boldsymbol{r_N})$ is the many-body wave function and N is the number of electrons. The problem with finding the many-body wavefunction is that it is computationally demanding, and it is almost impossible to solve the SE for large and complex systems. The advantage of the DFT is that Eqn. 2.3 can be inverted. Given the ground state density $\rho_0(r)$, it is possible, in principle, to determine the ground state wavefunction $\psi_0(\boldsymbol{r_1}, \boldsymbol{r_2}, \boldsymbol{r_3}, \ldots \boldsymbol{r_N})$. The implication of this is that ψ_0 is now a functional of ρ_0,

$$\psi_0(\boldsymbol{r_1}, \boldsymbol{r_2} \ldots \boldsymbol{r_N}) = \psi_0[\rho_0]. \quad (2.4)$$

Consequently, all ground state observables are functional of the ground state density ρ_0. The ground state wave function ψ_0 must reproduce the ground-state density ρ_0, and also minimize the energy, that is

$$E_{0,v} = min_{\psi_0 \to \rho_0} \langle \psi_0 | \hat{H} | \psi_0 \rangle. \quad (2.5)$$

Here, $\hat{H} = \hat{T} + \hat{U} + \hat{V}$, where $\hat{T}, \hat{U}$, and $\hat{V}$, are respectively, the kinetic energy, electron-electron and electron-nucleus operators. $E_{0,v}$ denotes the ground state energy in the potential $v(\boldsymbol{r})$. For an arbitrary density $\rho'(r)$, we may define the functional

$$E_v[\rho'] = min_{\psi' \to \rho'} \langle \psi' | \hat{H} | \psi' \rangle \ , \quad (2.6)$$

such that ρ' is a density, different from the ground-state density ρ_0 in potential $v(\boldsymbol{r})$. Then the wavefunction ψ' that produce this ρ' are different from the ground-state wavefunction ψ_0. According to the variational theorem, the minimum obtained from $E_v[\rho']$ is higher or equal to the ground state energy, that is

$$E_v[\rho_0] \leq E_v[\rho'].$$ (2.7)

This is analogous to the variational principle for the determination of wavefunctions, that is, a calculation of the expectation value of a Hamiltonian with a trial wave function ψ' that is different from its ground-state wavefunction ψ_0. One can never obtain an energy that is below the true ground-state energy

$$E_{0,v} = E_v[\psi_0] = \langle \psi_0 | \hat{H} | \psi_0 \rangle \leq \langle \psi' | \hat{H} | \psi' \rangle = E_v[\psi'] \quad (2.8)$$

Therefore, the energy functional $E_v[\rho']$ is minimized by the ground-state density ρ_0, and its value at minimum is $E_{0,v}$. The total energy functional can be written as

$$E_v[\rho'] = \min_{\psi' \to \rho'} \langle \psi' | \hat{T} + \hat{U} | \psi' \rangle + \int d^3r \rho'(\boldsymbol{r})\, v(\boldsymbol{r}) \equiv F[\rho'] + V[\rho'], \quad (2.9)$$

where $F[\rho'] = \min_{\psi' \to \rho'} \langle \psi' | \hat{T} + \hat{U} | \psi' \rangle$ is the internal energy functional, which is independent of the potential $v(\boldsymbol{r})$ describing a given particle-particle interaction, and is only determined by the form of the operators $\hat{U}$ and $\hat{T}$. It is often called the *universal functional* in the literature [*58*]. Eqns. (2.6-2.9) is the *constrained proof* of the Hohenberg-Kohn theorem as stated by Levy [*61*] and Lieb [*62*]. Eqn. (2.9) is minimized under the constraint that the total particle number *N* is an integer, and this is taken into account by means of a Lagrange multiplier λ,

$$\delta\{E_v[\rho'] - \lambda N\} = 0, \quad (2.10)$$

where $N = \int d^3r \rho'(\boldsymbol{r})$. Thus, minimization of Eqn. 2.10 with respect to ρ leads to

$$\frac{\delta E_v[\rho']}{\delta \rho'(\boldsymbol{r})} = \lambda = \frac{\partial E}{\partial N}, \quad (2.11)$$

and λ is seen to be the constant chemical potential of the electronic system. However, the original Hohenberg-Kohn theorem provides no guidance as to the form of $E_v[\rho']$. Therefore for DFT to be useful for practical applications, sufficiently accurate approximations (to be discussed in the following section) have to be found. Assuming that $v(\boldsymbol{r})$ for our system is known, and we have reliable approximations for $U[\rho]$ and $T[\rho]$, one only has to minimize the sum of the kinetic (*T*), interaction (*U*) and the potential energies (*V*). The energy corresponding to $v(\boldsymbol{r})$ at certain arbitrary density ρ is defined as

$$E_v[\rho] = T[\rho] + U[\rho] + V[\rho], \tag{2.12}$$

where $V[\rho]$ can be written as

$$V[\rho] = \int d\boldsymbol{r}\rho(\boldsymbol{r})\, v(\boldsymbol{r})\,. \tag{2.13}$$

It is apparent that $V[\rho]$ is non-universal as it depends on $v(\boldsymbol{r})$ which defines the system under study. However, an accurate scheme for treating the kinetic energy functional $T[\rho]$ is based on separating it into the kinetic energy of noninteracting particles of density ρ, that is, $T_s[\rho]$, the single particle kinetic energy, and a term that represents the remainder, denoted as $T_c[\rho]$. Likewise for $U[\rho]$, the full interaction energy can also be approximated. Thus,

$$T[\rho] = T_s[\rho] + T_c[\rho]\,, \tag{2.14a}$$

$$U[\rho] = U_H[\rho] + unknown\,, \tag{2.14b}$$

$T_s[\rho]$ is expressed in terms of single particle orbitals $\phi_i(r)$ of a noninteracting electronic system with density ρ

$$T_s[\rho] = -\frac{\hbar^2}{2m}\sum_i^N \phi_i^*(\boldsymbol{r})\frac{\partial^2\phi_i(\boldsymbol{r})}{\partial \boldsymbol{r}^2}d\boldsymbol{r}. \tag{2.15}$$

Eqn. 2.15 represents the fact that for noninteracting particles, the total kinetic energy is the sum of the individual kinetic energies. All orbitals $\phi_i(r)$ are functionals of ρ, thus making $T_s[\rho]$ an explicit orbital functional, but also an implicit density functional,

$$T_s[\rho] = T_s[\{\phi_i[\rho]\}]. \tag{2.16}$$

Approximating $U[\rho]$ by

$$U_H[\rho] = \frac{q^2}{2}\int d\boldsymbol{r}\int d\boldsymbol{r}'\frac{\rho(\boldsymbol{r})\rho(\boldsymbol{r}')}{|\boldsymbol{r}-\boldsymbol{r}'|}\,, \tag{2.17b}$$

the classical electrostatic energy of the charge distribution $\rho(\boldsymbol{r})$. Eqn. 2.12 can be rewritten as

$$E[\rho] = T[\rho] + U[\rho] + V[\rho] = T_s[\{\phi_i[\rho]\}] + V[\rho] + U_H[\rho] + E_{xc}[\rho]. \tag{2.18}$$

$E_{xc}[\rho]$ is called the *exchange-correlation functional* and contains all that that we are ignorant of about $T[\rho]$ and $U[\rho]$, that is, $T_c[\rho]$ and $U[\rho] - U_H[\rho]$. It is unknown, is density functional, and can now be formally defined as

$$E_{xc}[\rho] = T[\rho] + U[\rho] - T_s[\rho] - U_H[\rho]\,. \tag{2.19}$$

The minimization procedure proceeds by minimizing Eqn. 2.18 with respect to the density ρ, that is [*63*],

$$\frac{\delta E[\rho]}{\delta \rho} = 0\ , \tag{2.20}$$

and

$$\frac{\delta T_s}{\delta \rho(\boldsymbol{r})} + v(\boldsymbol{r}) + v_H(\boldsymbol{r}) + v_{xc}(\boldsymbol{r}) = 0\,. \tag{2.21}$$

Here, $v(r) = \delta V[\rho]/\delta\rho,$ is the external potential acting on the electrons, while

$$v_H(\boldsymbol{r}) = \int d^3r' \, \frac{\rho(\boldsymbol{r}')}{|\boldsymbol{r} - \boldsymbol{r}'|} \, , \tag{2.22}$$

is the Hartree potential, and $v_{xc}(r) = \delta E_{xc}/\delta\rho$ is often calculated once the expression for the E_{xc} has been chosen. If we now consider a system of non-interacting particles with total energy $E_T[\rho] = T_s[\rho] + V_s[\rho]$, under the influence of a potential $v_s(\boldsymbol{r})$, the minimization condition is according to the Euler's condition,

$$\frac{\delta E_T[\rho]}{\delta\rho(\boldsymbol{r})} = \frac{\delta T_s[\rho]}{\delta\rho} + v_s(\boldsymbol{r}) = 0, \tag{2.23}$$

where $v_s(\boldsymbol{r}) = \delta V_s[\rho]/\delta\rho$. Taking $\rho_s(r)$ as the solution to the equation and comparing Eqn. 2.23 with 2.21, then

$$\rho_s(\boldsymbol{r}) = \rho(\boldsymbol{r}) \, , \tag{2.24a}$$

and

$$v_s(\boldsymbol{r}) = v(\boldsymbol{r}) + v_H(\boldsymbol{r}) + v_{xc}(\boldsymbol{r}) \, . \tag{2.24b}$$

This implies that one can solve the Schrödinger equation for the density of many-body system in potential $v(\boldsymbol{r})$ by solving the equations on a noninteracting system in a potential $v_s(\boldsymbol{r})$. The SE for this auxiliary system is

$$\left[-\frac{\hbar^2}{2m}\nabla^2 + v_s(\boldsymbol{r})\right]\phi_i(\boldsymbol{r}) = \epsilon_i\phi_i(\boldsymbol{r}) \, . \tag{2.25}$$

The solution of Eqn.2.25 gives orbitals that reproduce the density of a system $\rho(r)$, that is,

$$\rho_s(\boldsymbol{r}) \equiv \rho(\boldsymbol{r}) = \sum\nolimits_i^N \xi_i \, |\phi_i(\boldsymbol{r})|^2, \tag{2.26}$$

where ξ_i is the occupation of the *i*'th orbital. Eqns. (2.24b, 2.25-2.26) are the Kohn-Sham (K-S) equation, and they have to be solved self-consistently. This is known as Kohn-Sham scheme of density functional theory. The K-S orbitals are

$$\phi_i(\boldsymbol{r}) = \sum_{p=1}^{P} c_{ip}\,\varphi_\gamma(\boldsymbol{r}), \tag{2.27}$$

where the $\varphi_\gamma(\boldsymbol{r})$ are the basis functions and c_{ip} are the expansion coefficients. The wavefunctions $\phi_i(\boldsymbol{r})$ belong to a function space which has an infinite dimension *P* and is therefore in principle, infinite. In practice however, one works with a limited set of basis function. Such a finite basis set cannot exactly describe $\phi_i(\boldsymbol{r})$, but one tries to find a basis that can generate a function that is close to it. Given the choice of basis, the coefficients c_{ip} are the only variables in the problem. The solution to KS equations amounts to determining the c_{ip} for the occupied orbitals that minimize the total energy. If we define

$$-\frac{\hbar^2}{2m}\nabla^2 + v_s(r) = H_s\,, \tag{2.28}$$

as the single particle Hamiltonian. Eqn 2.25 may be treated as an eigenvalue problem [*64,65,66*] of the form

$$(H_s - \varepsilon_i S_{mk})c_{ip} = 0\,, \tag{2.29}$$

which when expanded gives

$$\begin{bmatrix} \cdots & \cdots & \cdots \\ \vdots & \langle\phi_m|H_s|\phi_k\rangle - \epsilon_i\langle\phi_m|\phi_k\rangle & \vdots \\ \cdots & \cdots & \cdots \end{bmatrix}\begin{bmatrix} c_1 \\ \vdots \\ c_P \end{bmatrix} = \begin{bmatrix} 0 \\ \vdots \\ 0 \end{bmatrix}\,, \tag{2.30}$$

obtained by inserting Eqns. (2.27) in (2.25), and then left multiply with $\langle \phi_m \mid (m = 1, \ldots P)$ for a given *i*. Eqn. 2.28 is solved at each *k*-point in the irreducible wedge of the Brillouin zone (BZ) using appropriate routines such as LAPACK *[67*], for instance. By noting that

$$V[\rho] = \int d^3 r v(\boldsymbol{r})\rho(\boldsymbol{r}) = \int d^3 r \, [v_s(\boldsymbol{r}) - v_H(\boldsymbol{r}) - v_{xc}(\boldsymbol{r})]$$
$$= V_s[\rho] - \int d^3 \, r[v_H(\boldsymbol{r}) + v_{xc}(\boldsymbol{r})]\rho(\boldsymbol{r}), \qquad (2.31)$$

and once the ground state density ρ_0 is obtained, the total energy is calculated as

$$E_0 = \sum_{i=occ}^{N} \varepsilon_i - \frac{q^2}{2} \int d^3 \, r \int d^3 r' \frac{\rho_0(\boldsymbol{r})\rho_0(\boldsymbol{r}')}{|\boldsymbol{r} - \boldsymbol{r}'|} - \int d^3 \, r v_{xc}(\boldsymbol{r})\rho_0(\boldsymbol{r}) + E_{xc}[\rho_0] \qquad (2.32)$$

where $\sum_i^N \varepsilon_i = T_s + V_s = E_s$ and the summation is over the occupied states.

2.2 DFT approximation: Exchange-correlation functional

It was noted earlier that E_{xc} is defined as the difference between the exact energy and other contributions that may be evaluated numerically exactly, so that it contains all the unknown energy quantities. In practice, the total energy calculation requires approximations to be made for the exchange-correlation energy E_{xc}. The correct description of chemical system lies in the accuracy of the approximation of E_{xc} [*68,69*]. The adequacy of E_{xc} approximations may be discussed in term of exchange-correlation hole, that is, the depletion of electron charge around a particular electron due to the Coulomb repulsion and Fermi statistics [*57*]. The exchange-correlation energy can be interpreted as the interaction between an electron and its exchange-correlation hole charge. Kohn-Sham showed that the local density approximation (LDA) of the form,

$$E_{xc}^{LDA}[\rho] = \int d^3 r \, \rho(\boldsymbol{r}) \varepsilon_{XC}^{unif} \, ([\rho(\boldsymbol{r})]) \qquad (2.33)$$

could be applied to the limiting cases of slowly varying density and very high densities. $\varepsilon_{XC}[\rho(\boldsymbol{r})]$ is the exchange-correlation energy per particle of a homogenous electron gas at point $\boldsymbol{r}$ with density ρ. In a spin polarized system [*66*], $\varepsilon_{XC}([\rho(\boldsymbol{r})])$ incorporates information on the spin densities, and $\varepsilon_{XC}^{unif} = \varepsilon_X^{unif} + \varepsilon_C^{unif}$. ε_X^{unif} is known exactly [*57,70,71*],

$$\varepsilon_X^{unif}[\rho] = -\frac{q^2}{4\pi}(3\rho)^{4/3}. \tag{2.33a}$$

The LDA correlation formula with all the parameters are stated by Perdew and Wang [*72*] as

$$\varepsilon_C^{unif} = -2a\rho(1+\alpha_1 r_s)\log(\omega), \tag{2.33b}$$

where

$$\omega = 1 + \frac{1}{2a(\beta_1 r_s^{1/2} + \beta_1 r_s^{3/2} + \beta_4 r_s^2 + \beta_2 r_s}, \tag{2.33c}$$

and $a = 0.0310907, \alpha_1 = 0.21370, \beta_1 = 7.5957, \beta_2 = 3.5876, \beta_3 = 1.6382, \beta_4 = 0.49294$, and $r_s = \left(\frac{3}{4\pi\rho}\right)^{1/3}$. The LDA assumes that at each point $\boldsymbol{r}$, the exchange-correlation energy density is that of a uniform electron gas whose density is equal to the local density $\rho(\boldsymbol{r})$. The exchange and correlation potential is simply deduced as follows [*70*]

$$v_{XC}^{LDA} = \frac{\delta E_{XC}^{LDA}[\rho]}{\delta\rho(r)}. \tag{2.34}$$

$E_{XC}^{LDA}[\rho]$ has been remarkably successful even when applied to a non-homogenous system [*73*], and this has been attributed to systematic error cancellation. Furthermore, LDA underestimates ε_C and overestimates ε_X, resulting in a good value for the exchange-correlation energy [*74*].

The LDA, by construction hardly represents correct description of real electronic systems, and thus may not accurately describe the chemical bonding in molecules and solids. This is because any real

system is spatially inhomogeneous, with a spatially varying density [*70*]. The gradient expansion approximation (GEA) is a way to include this information in the functional. The term generalized gradient approximation (GGA) denotes a variety of ways that has been proposed for functions that modify the behaviour at large gradients in such a way as to preserve the desired properties. The (GGA) functional for spin-unpolarized system is of the general form [*75*]

$$E_{XC}^{GGA}[\rho] = \int d^3r f\big(\rho(\boldsymbol{r}), \nabla\rho(\boldsymbol{r})\big). \tag{2.35}$$

Different GGAs exist, where the difference is mainly in the choice of the function $f(\rho(\boldsymbol{r}), \nabla\rho(\boldsymbol{r})$. When constructing a GGA, one usually tries to incorporate a number of known properties of the exact functional into the restricted functional form of the approximation.

One of the early forms of GGA functional is due to Perdew and Wang (PW91) [*76*]. The PW91 functional is an analytical fit to a second-order gradient expansion for the exchange-correlation hole surrounding the electron in a system of slowly varying density, such that the spurious long-range contribution has been cut-off. Because the PW91 is a second–order gradient expansion for density variations that are small or slowly varying, it is less satisfactory in describing the linear response of the density of a uniform electron gas, compare to the local spin-density (LSD) approximation. Although, under Levy's uniform [*77*] scaling to the high- density limit, the GGA correlation energy functional behaves properly, its analytical parameterization in the form of PW91 does not. In the later formulation of exchange-correlation energy by Perdew et al. [*78*], the correlation energy scales properly in the high density limit, and the local spin density approximation, which is well suited to describe the linear response of the spin-unpolarized uniform electron gas, can be recovered. In this later formulation, the exchange-correlation functional $E_{XC}^{GGA}[\rho\uparrow, \rho\downarrow]$ for the spin-unpolarized system is [*78*]

$$E_{XC}^{GGA}[\rho\uparrow,\rho\downarrow] = \int d^3r\rho\varepsilon_X^{unif}(\rho)F_{XC}(r_s,\tau,s), \tag{2.36}$$

where $\varepsilon_X^{unif}(\rho) = -(3k_F/4\pi)$, is the exchange energy per particle for a uniform gas of densityρ, and $k_F = (3\pi^2\rho)^{1/3}$, is the local Fermi wave vector. $F_{XC}(r_s,\tau,s)$ is the enhancement factor over local exchange, $r_s(\rho = k_F^3/3\pi^2 = 3/4\pi r_s^3)$ is the local Wigner-Seitz radius; $\tau = |\nabla\rho|/2\,\phi k_s$ is a dimensionless density gradient; $k_s = \sqrt{4k_F/\pi a_0}$, and $\phi(s) = [(1+s)]^{2/3} + /[(1-s)]^{2/3}/2$ are Thomas-Fermi wave screening wave number and spin-scaling factor respectively; $a_0 = \hbar^2/m\,e^2$, and $s = (\rho\uparrow - \rho\downarrow/\rho)$ is the relative spin polarization. For real physical systems,$0 \lesssim \zeta \lesssim 3$ and $0 \lesssim r_s/a_0 \lesssim 10$, where $\zeta = |\nabla\rho|/(2k_F)\rho$ is a scaled density gradient. In the high density limit, $r_s \to 0$, the exchange dominates,

$$F_{XC}(r_s,\tau,s) = F_X(s,\zeta)\,. \tag{2.37}$$

$F_X(s,\zeta)$ is then found from the scaling relationship

$$E_X[\rho\uparrow - \rho\downarrow] = (E_X[2\rho\uparrow] + E_X[2\rho\downarrow])/2\,, \tag{2.38}$$

where $E_X[\rho]$ is the exchange energy of an unpolarized system of density $\rho(\boldsymbol{r})$, and the exchange energy is

$$E_X^{GGA} = \int d^3r\rho\varepsilon_X^{unif}(\rho)F_X(\zeta), \tag{2.39}$$

where $\varepsilon_X^{unif}(\rho) = -3\,e^2k_F/4\pi$. The correct uniform gas limit can be recovered if $F_X(0) = 1$. For small density variation around the density, LSD is the appropriate approximation to the exchange-correlation energy. To recover the LSD approximation

$$F_X(\zeta) \to 1 + 0.21951\zeta^2 \text{ as } \zeta \to 0\,. \tag{2.40}$$

The GGA correlation energy has the form

$$E_C^{GGA}[\rho\uparrow,\rho\downarrow] = \int d^3r\rho\left[\varepsilon_C^{unif}(r_s,s) + H(r_s,s,\tau)\right], \tag{2.41}$$

where $H(r_s,s,\tau)$ represents the gradient contributions. H is given by variation in the density as indicated by τ. H is such that in the slowly varying limit, that is, $\tau \to 0$, it is given by the second-order gradient expansion, and in the rapidly varying limit, $\tau \to \infty, H \to -\varepsilon_c^{unif}$, thus making the correlation vanish. It also cancels logarithmic singularity of $-\varepsilon_c^{unif}$, in the high density limit. The form of *H* and the values of different parameters contained therein are stated in the reference [*79*]. In comparison with local density functional (LDA, LSDA), the GGA tends to improve the total energies [*80*], energy barriers [*81,82*] and structural energy differences [*83*] among other properties of atoms and solids.

An improvement on the GGA is the new class of functionals, often referred to as the 'meta-GGA' [*84*]. In addition to the density $\rho(\boldsymbol{r})$, and the first gradient $\nabla\rho(\boldsymbol{r})$, the meta-GGA functional depends on the kinetic energy density τ (**r**) of the K-S orbitals,

$$E_{xc}^{M-GGA}[\rho] = \int d^3r h\big(\rho(\boldsymbol{r}),\nabla\rho(\boldsymbol{r}),\tau(\boldsymbol{r})\big), \tag{2.42}$$

where

$$\tau(\boldsymbol{r}) = \frac{1}{2}\sum_i^{occ}|\nabla\psi_i(\boldsymbol{r})|^2.$$

The new additional degree of freedom in the form of τ (**r**) may be exploited to include more of the exact properties into the approximation. Another form [*85*] of approximations to the exchange-correlation energy is the hybrid functional which mixes a fraction of the exact exchange with the GGA exchange,

$$E_x^{hyb}[\rho] = \alpha E_x^{EXX}[\rho] + (1-\alpha)E_x^{GGA}[\rho], \tag{2.43}$$

where α is the empirical mixing parameter. This exchange functional is then combined with some GGA for correlation. Hybrid functionals, though successful in quantum chemistry are less popular in solid-state physics.

2.3 Pseudopotential (PP) approach

2.3.1 Plane-waves and pseudopotentials

The eigenstates of the single particle Schrödinger (SE) equation can be chosen such that a wavevector k is associated with each wavefunction ϕ is and the relation [*86*]

$$\phi(r + R) = e^{ikR}\phi(r), \tag{2.44}$$

holds for every lattice vectors R. Alternatively, we may state that all eigenfunctions ϕ_{kn} where n labels the band index of the single-particle SE with a periodic potential, can be written as a periodic function w_{kn} modulated by a plane-wave with a wavevector k (Bloch's Theorem). Thus,

$$\phi_{kn}(r) = e^{ikr}\, w_{kn}(r). \tag{2.45}$$

Since the functions $w_{kn}(r)$ are periodic, they can be expanded as plane waves. Thus Eqn. 2.45 may now be rewritten as

$$\phi_{kn}(\boldsymbol{r}) = \sum_{G} e^{i(k+G)\boldsymbol{r}}\, c_{kn}(G)\,, \tag{2.46}$$

where G are reciprocal lattice vectors. The K-S equation of density functional theory using the Bloch states as the eigenfunctions [*87*]

$$\left(\frac{\hbar^2}{2m}\nabla^2 + v_{eff}(\boldsymbol{r})\right)\phi_{kn}(\boldsymbol{r}) = \varepsilon_{kn}\phi_{kn}(\boldsymbol{r}), \tag{2.47a}$$

with

$$v_{eff}\ (\boldsymbol{r}) = \ v_{ext}\,(\boldsymbol{r}) + v_H[\rho(\boldsymbol{r})] + v_{xc}[\rho(\boldsymbol{r})], \tag{2.46b}$$

and

$$\rho(\boldsymbol{r}) = \frac{\Omega_{BZ}}{2\pi} \sum_{n,\ BZ} \int |\phi_{kn}(\boldsymbol{r})|^2 \delta(\epsilon_F - \varepsilon_{kn}) d^3k\ , \tag{2.47c}$$

where $v_{ext}(\boldsymbol{r})$, $v_H[\rho(\boldsymbol{r})]$, $v_{xc}[\rho(\boldsymbol{r})]$ are the external potential of the nuclei, the Hartree, and the exchange-correlation potential, respectively. Ω_{BZ} is the volume of the first Brillouin Zone, and $\delta(\epsilon_F - \varepsilon_{kn})$ is a step function such that

$$\delta(\epsilon_F - \varepsilon_{kn}) = \begin{cases} 1, & \varepsilon_{kn} < \varepsilon_F \\ 0, & \varepsilon_{kn} > \varepsilon_F \end{cases}\ . \tag{2.48}$$

ε_F is the Fermi energy, which is defined as the highest energy up to which single-particles states are be occupied. We can restrict the calculation of the eigenfunctions to within one unit cell. By convention, this unit cell is usually taken to be the first Brillouin zone (BZ). The number of electron (n_E) in the unit cell is the integral of Eqn. 2.47c,

$$\int \rho(\boldsymbol{r}) d^3\, r = n_E\ . \tag{2.49}$$

In order to solve the Kohn-Sham equation, one usually expresses the KS orbitals in terms of a suitable finite basis set. The dimension of the plane-wave basis set is determined by fixing the kinetic energy cut-off, E_C, through the condition [*88*]

$$|k + G|^2 \leq E_C \tag{2.50}$$

The number of plane-waves n_{PW} is related to E_c through the relationship [*88*]

$$n_{PW} \approx \frac{4\pi}{3\Omega_{BZ}} (E_c)^{\frac{3}{2}} \tag{2.51}$$

If all the electrons are treated explicitly in many-electrons calculations, a large number of plane waves would be needed to describe the strongly localized core electrons, and the rapid oscillations

(wiggles) of the valence wave functions in the core region [*60*]. *Pseudopotentials* (PP) are constructed to obtain a fairly accurate description of a chemical system with a reasonably low number of planewaves. In PP, the core states are frozen [*55*], and only the valence states which are relevant in bonding are treated explicitly. In addition, the orthogonalization wiggles in the valence wavefunction are removed, and the resulting pseudo-wavefunctions are therefore smooth. The PP describes the interaction between the valence electrons and the ionic cores (nuclei + core electrons) such that its ground state wavefunction mimics the all-electron wavefunction outside a selected radius. This frozen core approximation is generally reliable, but may fail for some elements with extended core states [*55*].

2.3.2 Norm-Conserving Pseudopotentials

The pseudopotential replaces the all-electron potential within a given sphere of radius r_C with a much weaker new potential with a nodeless smooth ground state wavefunction to the same energy eigenvalue as the original all-electron state. The nodeless smooth ground state wavefunction matches exactly the all-electron wavefunction outside r_C. Good and reliable pseudopotential must satisfy the following conditions as stated by Hamann, Schluter and Chiang (HSC) [*89*]:

1. The pseudo-valence and all-electron eigenvalues agree for the chosen atomic reference configuration.
2. The pseudo-atomic and the all-electron wavefunctions must agree beyond a chosen core radius r_C.
3. The integrated charge density from 0 to r_C must agree for both pseudo and all-electron wavefunctions. Inside r_C, the all-electron wavefunction $\psi_{AE}(r)$ and the potential $V_{AE}(r)$, differ from their pseudo counterparts, i.e. $\psi_{PS}(r)$ and $V_{PS}(r)$, respectively, but the integrated charge density must be the same for a given angular momentum *l*, that is,

$$\int_0^{r_C} |\psi_{l,AE}(r)|^2 \, r^2 dr = \int_0^{r_C} |\psi_{l,PS}(r)|^2 \, r^2 dr = \varrho_l \ . \tag{2.52}$$

The conservation of ϱ_l insures that in the core region ($r_C \to 0$), the total charge is correct. Both wavefunctions, that is, $\psi_{AE}(r)$ and $V_{AE}(r)$, must generate identical electron densities in the outside region, i.e. $r > r_C$. This is called *norm conservation*.

4. The logarithmic derivatives, with respect to *r*, of the all-electron and the pseudo wavefunction agrees at r_C and thus at $r \geq r_C$. This is because a wavefunction $\psi_{l,AE}(r)$ and its radial derivative, $\psi'_{l,AE}(r)$, are continuous at r_C for any smooth potential,

$$L_l(\varepsilon) = \frac{d}{dr} ln\, \psi_{l,AE}(r;\varepsilon) = \frac{\psi'_{l,AE}(r;\varepsilon),}{\psi_{l,AE}(r;\varepsilon)} \ , \tag{2.53}$$

at $r = r_C$.

5. The first energy derivative of the logarithmic derivative of the pseudo and all-electron wavefunction must agree at the cut-off radius r_C, and the energy chosen for the construction of pseudopotential of angular momentum l. This ensures that the scattering properties of the pseudo and all-electron agree, with minimum error, to linear order around the chosen energy. That is, at $r = r_C$,

$$\frac{dL_l(\varepsilon, r_C)}{d\varepsilon} = \int_0^{r_C} (\psi_{l,AE}(r))^2 \, dr, \tag{2.54}$$

where $L_l(\varepsilon, r_C)$ is as defined in Eqn. (2.53).

The HSC pseudopotential is semilocal, that is, it is local in the radial variable but non-local (*l* dependent) in the angular variable. Thus, it is usually written as an operator in spherical coordinates $\boldsymbol{r}(r, \theta, \vartheta)$ and $\boldsymbol{r}'(r', \theta', \vartheta')$

$$V_{PS}^{(sl)}(\boldsymbol{r},\boldsymbol{r}') = V^{loc}(r)\delta(\boldsymbol{r}-\boldsymbol{r}') \quad + \sum_{l=0}^{l_{max}} \delta V_l(r)\delta(r-r')\,\widehat{P}_l(\hat{\boldsymbol{r}},\hat{\boldsymbol{r}}'). \tag{2.55}$$

Here, $V^{loc}(r)$ is the local potential and $\delta V_l(r) = V_l^{PS}(r) - V^{loc}(r)$, is a localized function which is zero for $r > r_C$ where $V_l^{PS}(r)$ is the original *l*-dependent pseudopotential. The non-locality is mainly due to the projector $\widehat{P}_l$ on the angular momentum *l*, and this is defined as $\widehat{P}_l(\hat{\boldsymbol{r}},\hat{\boldsymbol{r}}') = \sum_{m=-l}^{l} |Y_l^m\rangle\langle Y_l^m|$, where $|Y_l^m\rangle$ are normalized spherical harmonics. The projector operator picks out the *l*-angular momentum from the subsequent wavefunction, so that when the full pseudopotential operator is applied to a general wavefunction, each angular momentum component of the wavefunction experiences only its corresponding part $V_l^{PS}(r)$ of the potential. If we define the semilocal operator of Eqn. 2.54 as

$$V^{SL} = \delta V_l(r)\delta(r-r')\widehat{P}_l(\hat{\boldsymbol{r}},\hat{\boldsymbol{r}}'), \tag{2.56}$$

when it operates on states φ_i and φ_j, the integral is proportional to [*73*]

$$\langle\varphi_i|V^{SL}|\varphi_j\rangle = \int dr\varphi_i(r,\theta,\vartheta)\left[V^{SL}\varphi_j\right]_{r,\theta,\vartheta}, \tag{2.57}$$

and $\left[V^{SL}\varphi_j\right]_{r,\theta,\vartheta}$ is proportional to

$$\int d(cos\theta')d\vartheta' Y_{lm}(\theta',\vartheta')\varphi_j(r,\theta',\vartheta'). \tag{2.58}$$

Therefore for each pair of functions, φ_i and φ_j, a radial integral is involved, leading to high computational cost for large number of $\boldsymbol{k}$ points in the Brillouin Zone. To address the problem of computation cost, Kleinman and Bylander [*90*] (to be henceforth referred to as K-B) proposed an alternative form of ionic pseudopotential. K-B recognized that, it possible to construct a *norm-*

conserving separable pseudopotential by re-writing $\delta V_l(r)\delta(r-r')\widehat{P}_l(\hat{\boldsymbol{r}},\hat{\boldsymbol{r}}')$ in Eqn. 2.55 as a product

$$\delta V_l(r)\delta(r-r')\widehat{P}_l(\hat{\boldsymbol{r}},\hat{\boldsymbol{r}}') \rightarrow \delta V_{NL}(\boldsymbol{r},\boldsymbol{r}') = \frac{\left|\varphi_{lm}^{ps}\delta V_l\right\rangle\left\langle\delta V_l\varphi_{lm}^{ps}\right|}{\left\langle\varphi_{lm}^{ps}\left|\delta V_l\right|\varphi_{lm}^{ps}\right\rangle}, \tag{2.59}$$

where φ_{lm}^{ps} is the HSC reference pseudo-wavefunction of angular momentum *l*, and $\varphi_{lm}^{ps} = \varphi_{lm}^{ps}(\boldsymbol{r})$ and $\delta V(\boldsymbol{r},\boldsymbol{r}')$ has the desired separable form. When Eqn. 2.59 operates on wavefunctions, it becomes

$$\left\langle\varphi_i\left|\delta V_{NL}\right)\right|\varphi_j\right\rangle = \sum_{lm}\left\langle\varphi_i\left|\varphi_{lm}^{ps}\delta V_l\right\rangle\frac{1}{\left\langle\varphi_{lm}^{ps}\left|\delta V_l\right|\varphi_{lm}^{ps}\right\rangle}\left\langle\delta V_l\varphi_{lm}^{ps}\right|\varphi_j\right\rangle, \tag{2.60}$$

where the function

$$\left\langle\delta V_l\varphi_{lm}^{ps}\left|\varphi_j\right\rangle\right. = \int d\boldsymbol{r}\,\delta V_l(r)\varphi_{lm}^{ps}(\boldsymbol{r})\varphi_j(\boldsymbol{r}) \tag{2.60a}$$

so that a separable potential is a sum of projectors. Equations (2.59-2.60) should be contrasted with Equations (2.56-2.57), so that it is apparent that a K-B separable potential leads to reductions in numerical efforts. Finally, the KB pseudopotential should be used with caution, as their usage may sometimes give unphysical results. This is due to the appearance of additional eigenstates with nodes below the zero-node state, or even the zero-node states may be followed directly by additional $n \geq 2$ states. Methods of avoiding such spurious states, otherwise known as *ghosts* are discussed in relevant literatures [*91*, *92*].

2.3.3 Ultrasoft Pseudopotentials (USPP)

In Vanderbilt's pseudopotential formalism [*93*], it is possible to construct a fully nonlocal potential directly from atomic all-electron calculations, thus bypassing the construction of semilocal type pseudopotential entirely. The main thrust of this formalism is the radical departure from the concept

of norm-conservation. The pseudo-wavefunctions are required to be equal to the all-electron wavefunctions at the cut-off radius r_C. However, r_C can be chosen to be well beyond the maximum of the radial wave function, that is, the pseudopotential can be made as *soft* as possible. This additional freedom in choosing r_C enables the number of planewaves used in the calculations to be reduced, especially since large values of r_C may be used. The generalized requirement for norm conservation can be stated as follows

$$\varrho_{\alpha\beta} = \langle\phi_\alpha|\phi_\beta\rangle_{r_c} - \langle\varphi_\alpha|\varphi_\beta\rangle_{r_c} \quad , \tag{2.61}$$

where $|\phi_\alpha\rangle$ and $|\varphi_\beta\rangle$ are all-electron and pseudo-wavefunctions, respectively. Vanderbilt shows that the condition $\varrho_{\alpha\beta} = 0$, is unnecessary. The consequence of this is the inclusion of a non-local overlap operator *S* into the secular equation, which then transforms into the *generalized eigenvalue problem*

$$(H - \varepsilon_i S)|\varphi_\alpha\rangle = 0, \tag{2.62}$$

where

$$S = I + \sum_{\alpha,\beta} \varrho_{\alpha\beta} \, |\chi_\alpha\rangle\langle\chi_\beta| \, , \tag{2.63}$$

is non-diagonal, and I denotes the identity operator. Defining the fully non-local potential operator

$$V_{NL}^{US} = \sum_{\alpha,\beta} D_{\alpha\beta} \, |\chi_\alpha\rangle\langle\chi_\beta| \quad , \tag{2.64}$$

and

$$D_{\alpha\beta} = B_{\alpha\beta} + \varepsilon_j \varrho_{\alpha\beta} \quad , \tag{2.65}$$

while imposing the condition

$$\langle\varphi_\alpha|S|\varphi_\beta\rangle = \langle\phi_\alpha|\phi_\beta\rangle_{r_c} \quad , \tag{2.66}$$

the generalized eigenvalue problem is solved accordingly. It should be noted that ϱ and D are Hermitian matrices, while B is not. H and S are therefore Hermitian operators. The pseudopotential is characterized by the functions $\langle\chi_\beta|$, the coefficients $D_{\alpha\beta}$, and the local component of the pseudopotential. The functions $\langle\chi_\beta|$ are represented in angular representation, that is, spherical harmonics multiplied by the radial functions which vanish outside the cut-off radius. The solution of the generalized eigenvalue problem has to be normalized according to

$$\langle\varphi_{nk}|S|\varphi_{n'k}\rangle = \delta_{nn'} \quad . \tag{2.67}$$

Equations (2.66-2.67) ensure that the pseudosolutions ϕ_{nk} have the same norm as the all-electron wavefunction at and beyond the cut-off radius r_C. To make up the charge deficit that is associated with a pseudo-wavefunction in the core region, an augmentation term needs to be added to the valence charge density n_v. Thus,

$$n_v(\boldsymbol{r}) = \sum_{n,k}^{occ} \varphi_{nk}^*(\boldsymbol{r})\varphi_{nk}(\boldsymbol{r}) + \sum_{\alpha,\beta} \zeta_{\alpha\beta}\, \varrho_{\alpha\beta}(\boldsymbol{r}) \quad , \tag{2.68a}$$

where

$$\zeta_{\alpha\beta} = \sum_{n,k} \langle\chi_\alpha|\varphi_{nk}\rangle \langle\varphi_{n'k}|\chi_\beta\rangle \, , \tag{2.68b}$$

and

$$\varrho_{\alpha\beta}(\boldsymbol{r}) = \phi_\alpha^*(\boldsymbol{r})\phi_\beta(\boldsymbol{r}) - \varphi_\alpha^*(\boldsymbol{r})\varphi_\beta(\boldsymbol{r}) \ . \tag{2.68c}$$

The total number of valence electrons, N_v , is given as

$$\int d^3r\, n_v(\boldsymbol{r}) = N_v \tag{2.69}$$

The augmentation functions $\varrho_{\alpha\beta}(\boldsymbol{r})$ are strictly localized in the core regions. Thus, the electron density in Eqn.2.66 is the same as in NCPP, but is now separated into a soft delocalized contribution given by the square moduli of the wavefunctions, and a new hard contribution localized at the cores. The USPP is fully determined by the local part of the PP, $V_{ion}^{loc}(\boldsymbol{r})$, the augmentation function, $\varrho_{\alpha\beta}(\boldsymbol{r})$, the ionic position dependent functions, $\chi_\alpha(\boldsymbol{r}) = \chi_\alpha(\boldsymbol{r} - \boldsymbol{R})$, with $\boldsymbol{R}$ being the atomic coordinate, and finally, the coefficients $D_{\alpha\beta}$ which characterize the PP and are unique for different atomic species. The total energy E_T of N_v valence electrons described by the wavefunction φ_{nk}

$$E_T[\{\varphi_{nk}\},\{\boldsymbol{R}\}] = \sum_{n,k}\left\langle \varphi_{nk}\left|\left(-\nabla^2 + V_{ion}^{loc}(\boldsymbol{r})\right) + \sum_{\alpha\beta} D_{\alpha\beta}^{ion}\,|\chi_\alpha\rangle\langle\chi_\beta|\right|\varphi_{nk}\right\rangle + E_H(n_v) + E_{xc}[n_v + n_c] + E_{ii}(\boldsymbol{R}) \tag{2.70}$$

is to be minimized subject to the condition of Eqn. 2.67. $E_{ii}(\boldsymbol{R})$ is the ion-ion interaction energy as a function of atomic coordinate only, and it therefore vanishes. The non-linear core correction n_c [*94*] is usually included in E_{xc} to improve transferability of the pseudopotential. The secular equation to be solved becomes [*93*]

$$(-\nabla^2 + V^{loc} + V_{NL}^{US} - \varepsilon_{nk} S)|\varphi_{nk}\rangle = 0 \quad . \tag{2.71}$$

V_{NL}^{US} and S are as defined in Eqns. (2.64-2.66). The bare ion pseudopotential V_{ion}^{loc} and $D_{\alpha\beta}^{ion}$ must be *descreened* as follows

$$V_{ion}^{loc} = V^{loc} - V_{Hxc} \quad , \tag{2.72a}$$

and

$$D_{\alpha\beta}^{ion} = D_{\alpha\beta} - D_{\alpha\beta}^{Hxc} \quad , \tag{2.72b}$$

where

$$V_{Hxc}(\boldsymbol{r}) = V_H[\boldsymbol{r}; n_v] + V_{xc}[\boldsymbol{r}; n_v + n_c] \, , \tag{2.72c}$$

and

$$D_{\alpha\beta}^{Hxc} = \int d\boldsymbol{r}\, V_{Hxc}(\boldsymbol{r}) \varrho_{\alpha\beta}(\boldsymbol{r}) \quad . \tag{2.72d}$$

Finally, the Vanderbilt ultrasoft pseudopotential scheme is good for treating elements with nodeless valence states, such as 3*d* valence electrons. For these elements, the pseudo and the all-electron wavefunctions are almost identical. Since these valence electrons are strongly localized in the ionic core region, many plane waves are required to accurately represent their wavefunction. Thus calculations involving such elements are sometimes prohibitively expensive. However, by allowing a relatively large cut-off ('smoothness') compared to the norm-conserving pseudopotential, the number of basis functions needed to describe the plane wave is reduced, and the computational cost is reduced. In USPP, the construction of the pseudofunction can be made as smooth as possible, hence the name 'ultrasoft. In norm-conserving PP, the electron density is defined as in Eqn. 2.66, excluding the second term on the right hand side. Therefore, the energy cut-off required to describe fully the electron density $E_c^{e\rho}$, is four times the energy cut-off for the pseudo wavefunctions, E_c^{pwf}. Thus [*95*]

$$E_c^{e\rho} = 4E_c^{pwf} \quad . \tag{2.73}$$

However, this relationship does not hold in the ultrasoft PP formulation due to the presence of augmentation functions $\varrho_{\alpha\beta}(\boldsymbol{r})$ in the electron density. It is therefore appropriate to introduce two independent energy cut-offs: one to describe the augmentation functions, and the other in which Eqn. (2.69) holds. The former is usually of higher energy cut-off E_c^{ae} than the latter. In the latter case, however, by modifying $\varrho_{\alpha\beta}(\boldsymbol{r})$ within the inner core region defined by r_{in}, the charge cut-off $E_c^{e\rho}$ can be reduced. The charge density defined by this pseudo $\varrho_{\alpha\beta}(\boldsymbol{r})$ preserves all the charge moments such that the electrostatic potential outside the r_{in} is unchanged. The charge density $\varrho_{\alpha\beta}(\boldsymbol{r})$ is modified and re-written in terms of functions of total angular momentum L, which are then smoothed using the L-dependent inner radii. Thus [*96*],

$$\varrho_{\alpha\beta}(\boldsymbol{r}) = \sum_{LM} c_{LM}^{\alpha\beta}\, Y_{LM}(\hat{r}) q_{\alpha\beta}^{rad}(r) \quad , \tag{2.74}$$

where $c_{LM}^{\alpha\beta}$ are Clebsch-Gordan coefficients, $Y_{LM}(\hat{r})$ are spherical harmonics, and $q_{\alpha\beta}^{rad}(r)$ gives the all-electron radial dependence of $\varrho_{\alpha\beta}(\boldsymbol{r})$ and is independent of L and M by construction. However, $q_{\alpha\beta}^{rad}(r)$ in Eqn. (2.74) may be written such that it is L-dependent. This is because the number of possible L channels is finite, since a nonlocal PP is required only for the lowest L. Thus

$$\varrho_{\alpha\beta}(\boldsymbol{r}) = \sum_{LM} c_{LM}^{\alpha\beta}\, Y_{LM}(\hat{r}) q_{\alpha\beta}^{L}(r)\,. \tag{2.75}$$

For each L-component, however, the Lth moments of charge distribution must be conserved. Introducing r_{in}^{L}, the L-dependent inner cut-off radius, this conservation requirement can be stated as

$$\int_0^{r_{in}^L} r^2 dr\, r^L q_{\alpha\beta}^{L}(r) = \int_0^{r_{in}^L} r^2 dr\, r^L q_{\alpha\beta}^{rad}(r)\,. \tag{2.76}$$

The decomposition of $\varrho_{\alpha\beta}(\boldsymbol{r})$ in terms of functions of L-dependent allows an accurate smoothening of the $\varrho_{\alpha\beta}(\boldsymbol{r})$, and reduces the need for higher Fourier components which are mainly due to the high L-components. In addition, for a given E_c^{ep}, it is convenient to use a smaller r_{in}^{L} for low L-components, since a relatively better description of the lowest moments of the electron density is maintained. This procedure is particularly important for *d*-electron elements, such as, Cu and Ti, since in these cases, the charges are highly localized and the low L-component of the augmentation charges is the dominant contribution to the electron density.

2.4 Smearing techniques in Brillouin zone (BZ) integration

In many-solid state calculations, it is a common routine to calculate integrals of periodic functions over the Brillouin zone, especially when evaluating important spectral properties of solids [*97*], such

as the density of states or charge densities. For non-metallic systems such as insulators and semiconductors, the function to be integrated has the property that it is continuously differentiable, due to the energy gap between the occupied and the empty bands. The convergence of the integral to be evaluated is proportional to the exponential of the spacing, Δ, in the uniform mesh of the BZ of the primitive reciprocal lattice. In the study of metals, however, we wish to evaluate a function *I* of the form [*98*]

$$I = \frac{\Omega}{(2\pi)^3}\int \theta(E(\boldsymbol{k}) - \epsilon_F) f(\boldsymbol{k}) d\boldsymbol{k} \quad , \tag{2.77}$$

where the integration is over the BZ; ϵ_F is the Fermi energy, $E(\boldsymbol{k})$ represents the energy band as a function of the wavevector, and $\theta(x)$ is the Fermi cut-off or step function. The integrand function is discontinuous and non-differentiable in reciprocal space due to the partial filling of the energy bands. Therefore, its Fourier transform does not decay rapidly in real space, leading to slow convergence when sampling over a uniform mesh in the BZ with the linear tetrahedron method [*99*].

Several methods of BZ integration in metals [*100*] aim at improving *k* convergence consists in using smooth continuous functions such as the Gaussian, Lorentzian, or similar functions, $\bar{\theta}(\sigma, x)$, parameterized by linewidth, σ, to broadening or 'smear' contributions from all *k* points. In the limit of $\sigma \rightarrow 0, \bar{\theta}(\sigma, x)$ becomes the step function, and one recovers the ''absolutely converged result'' [*98*]. The convergence of the result can be checked by varying the value of σ. For example, if σ is large, the BZ integration converges with a small number of *k* points to an inaccurate result. Decreasing the value of σ tends to bring the convergence to the right answer but at the expense of using large number of *k* points mesh. A popular form of smearing $\bar{\theta}(\sigma, x)$, is the Gaussian-method represented as [*101*]

$$\bar{\theta}(\sigma, x) = \frac{2}{\sqrt{\pi}}\int_{-\infty}^{x/\sigma} exp(-y^2) dy \quad . \tag{2.78}$$

To determine the Fermi energy, the constraint of conservation on the total number of electrons, n_{el}, with the same width σ is imposed as follows

$$\frac{\Omega}{(2\pi)^3}\int d\boldsymbol{k}\bar{\theta}(\sigma,\epsilon_F-\epsilon(\boldsymbol{k}))=n_{el} \quad , \tag{2.79}$$

and the Fermi energy is then determined from the Gaussian-smoothed density of states. This approximation creates smooth integrand functions different from the true function by an error which depends on σ. It is however possible to estimate this error, and hence to add a σ dependent correction to the total energy functional [*102*].

An improvement of the broadening function introduced by Methfessel and Paxton [*98*] (henceforth to be referred to as M-P) allows independent control of the *k*-points convergence and the absolute convergence. This implies that the broadening can be chosen such that *k* convergence is reached for a relatively coarse mesh, and the corresponding limit is close to the correct value. In the M-P approach, the integral in the Eqn. 2.77 is transformed into the energy integral as follows

$$I=\frac{\Omega}{(2\pi)^3}\int\theta(E(\boldsymbol{k})-\epsilon_F)f(\boldsymbol{k})d\boldsymbol{k}=\int_{-\infty}^{+\infty}\theta(\epsilon-\epsilon_F)F(\epsilon)d\epsilon\,, \tag{2.80}$$

where

$$F(\epsilon)=\frac{\Omega}{(2\pi)^3}\int f(\boldsymbol{k})\,\delta\big(\epsilon-E(\boldsymbol{k})\big)d\boldsymbol{k}\,. \tag{2.81}$$

If $F(\epsilon)=g(\epsilon)$, the density of states, then *I* becomes the total charge within the Fermi surface, or $F(\epsilon)=g(\epsilon)\epsilon$, if *I* is to be the band energy. Then, by expressing $\delta(x)$ as a complete set of functions,

$$\delta(x)=\sum_{i=0}^{\infty}A_iH_{2i}\,(x)e^{-x^2}\ , \tag{2.82}$$

where H_i is the Hermite polynomial of degree i, and by using the orthogonality of the Hermite polynomials with respect to Gaussian weights [*103*] to obtain the coefficient A_i, a finite sum $S_n(x)$ which serves as an approximation to the $\delta(x)$ may be obtained. Thus

$$S_n(x) = \sum_{i=0}^{n} A_i H_{2i}(x) e^{-x^2}. \tag{2.83}$$

To obtain successive approximations to the step function $\theta_n(x)$, the function $S_n(x)$ is integrated as follows

$$\theta_n(x) = 1 - \int_{-\infty}^{x} S_n(t)dt \quad . \tag{2.84}$$

The zero order approximation, that is when $n = 0$, corresponds to simple Fermi-Dirac-like smearing, and higher-order terms (i.e. $n \geq 1$) are corrections to the error in using such procedure. Defining $x = (\epsilon - E_F)/\sigma$ as the dimensionless energy variable, and if $F(\epsilon)$ is sufficiently smooth within the energy range determined by the choice of broadening σ, the errors δI_n (at k convergence) due to the use of zero and first order approximation to the step function in Eqn. 2.80 are

$$\delta I_n = \int_{-\infty}^{+\infty} [\theta_n((\epsilon - E_F)/\sigma) - \theta(\epsilon - E_F)F(\epsilon)d\epsilon]$$

$$= \begin{cases} \frac{1}{4}F'(E_F)\sigma^2 & for\ N = 0 \\ 0 \quad for \quad N > 0 \end{cases} \quad . \tag{2.85}$$

Thus, the zero-order approximation converges to the correct value as $\sigma \to 0$, but slowly as σ^2. On the other hand, all higher-order approximations, that is, $N > 0$ give the correct results.

2.5 Finding minimum energy path: The nudged elastic band (NEB) method

The nudged elastic band method [*104,105*] is an efficient method for finding the minimum energy path (MEP) between a pair of known stable states of a transition. This pair of states has the property

that each is a local minimum on the potential energy surface, and a path connecting the states that has the greatest statistical weight is the minimum energy path. The minimum energy path has the property that any point on it is at the energy minimum in all directions that are perpendicular to the path [*106*]. At any point along the path, the force acting on the atoms is only pointing along the path, and the energy is at minimum for the any perpendicular degree of freedom. The maxima on the MEP are saddle points on the potential energy surface, and the energy of the saddle point relative to that of the initial state is the *migration energy barrier*. The migration barrier energy can then be used to estimate the rate constant for a given transition process. The relative distance between the final and the initial states is the reaction coordinate. At the saddle point, the direction of the reaction coordinate is given by the normal mode eigenvector corresponding to negative curvature [*105*].

The NEB method has been well integrated into the electronic structure calculations [*107,108*], especially the plane-wave based density functional calculations and those using the empirical potentials. In addition, studies involving very large systems, such as those involving millions of atoms, have been carried out using the NEB. The MEP is found by constructing replicas of the system, often called *images*, between the initial and the final states of the transition process. The number of intermediate images is in the order of 5-20, and they are connected by a spring-like system through which adjacent images interact such that continuity of the path is ensured. The system of images and spring system thus constitutes an *elastic band*. The MEP is obtained by optimizing the band, which basically involves minimization of the force acting on the images. To further illustrate the concepts of NEB, imagine an elastic band consisting of $n+1$ images which are denoted as $[\boldsymbol{R_0}, \boldsymbol{R_1}, \boldsymbol{R_2}, \dots, \boldsymbol{R_n}]$, where the endpoints $\boldsymbol{R_0}$ and $\boldsymbol{R_{n+1}}$ constitutes the known fixed initial and final states, and $\boldsymbol{R_i}$ is a vector containing the coordinates of image i. The $n-1$ intermediate images need to be minimized by appropriate optimization algorithm. The total force (shown in Fig.

2.1) acting on an image *i* in the band, $\boldsymbol{F_i^{NEB}}$, is the sum of two independent components: the spring force parallel to the local tangent, $\boldsymbol{F_{si}^{\parallel}}$, and the force component

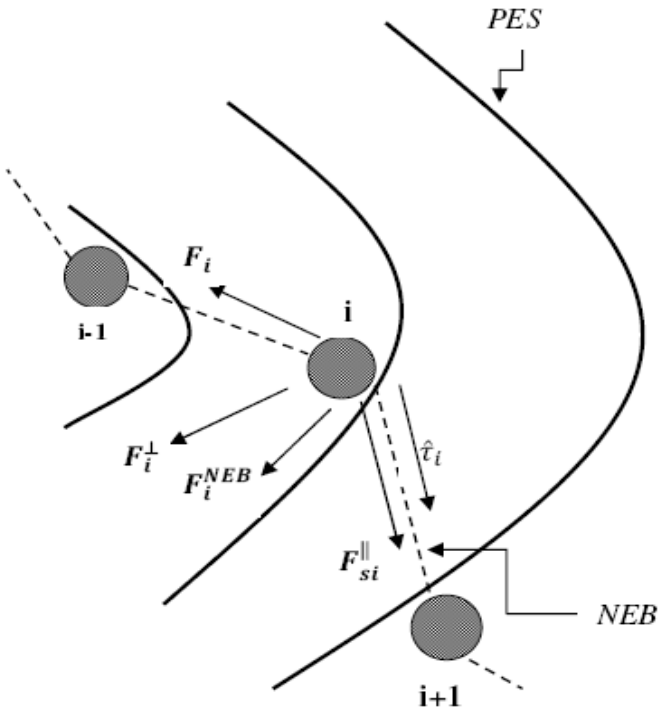

Fig. 2.1. Schematic of the resolution of the components making up the nudged elastic band (NEB) force on the potential energy surface (PES): the spring force $\boldsymbol{F_{si}^{\parallel}}$ acting long the tangent $\boldsymbol{\hat{\tau}_i}$, the perpendicular force due to the potential $\boldsymbol{F_i^{\perp}}$, and $\boldsymbol{F_i}$ is the unprojected force due to the potential.

perpendicular to the local tangent, $\boldsymbol{F_i^{\perp}}$. Thus [*105*]

$$\boldsymbol{F_i^{NEB} = F_{si}^{\parallel} + F_i^{\perp}} . \tag{2.86}$$

Defining the true force $\boldsymbol{F_i^{\perp} = -\nabla E(R_i)|^{\perp}}$, and

$$\boldsymbol{\nabla E(R_i)|^{\perp} = \nabla E(R_i) - \nabla E(R_i).\hat{\tau}_i} , \tag{2.87}$$

where $\boldsymbol{E(R_i)}$ is the energy of the system as a function of all the atomic coordinates, and $\hat{\tau}_i$ is the normalized local tangent at image *i* which may be simply defined as

$$\hat{\boldsymbol{\tau}}_{\boldsymbol{i}} = \frac{\boldsymbol{R_{i+1} - R_{i-1}}}{|\boldsymbol{R_{i+1} - R_{i-1}}|} \quad , \tag{2.88}$$

or

$$\hat{\boldsymbol{\tau}} = \frac{\boldsymbol{\tau}}{|\boldsymbol{\tau}|} \quad , \tag{2.89}$$

where

$$\boldsymbol{\tau} = \frac{\boldsymbol{R_i - R_{i-1}}}{|\boldsymbol{R_i - R_{i-1}}|} + \frac{\boldsymbol{R_{i+1} - R_i}}{|\boldsymbol{R_{i+1} - R_i}|} . \tag{2.90}$$

The latter definition of the tangent vector ensures the images are equispaced even in regions of high curvature as long as the spring constant is the same. The spring force $\boldsymbol{F_{si}^{\parallel}}$ in Eqn. 2.86 follows simply the application of Hooke's law. Thus

$$\boldsymbol{F_{si}^{\parallel}} = k_{spr}[|\boldsymbol{R_{i+1} - R_i}| - |(\boldsymbol{R_i - R_{i-1}}|]\hat{\boldsymbol{\tau}}_{\boldsymbol{i}} \quad , \tag{2.91}$$

where k_{spr} is the spring constant. The force projection as stated in Eqns. (2.86-2.91), which enables only the parallel component of the spring force and the perpendicular component of the true force to be included in the calculation of the force on each image is referred to as *nudging*. The spring force then controls only the separation of the images along the elastic band. This force projection is essentially what distinguishes the NEB method from similar elastic bands methods [*106-108*]. Optimization routines are used for moving the images along the MEP, with the various force-based routines commonly employed including the steepest descent [*109*], the conjugate gradient [*110*] and the Broyden-Fletcher-Goldfarb-Shanno (BFGS) [*111-113*].

An efficient technique of finding the saddle point introduces a small modification to the regular NEB as explained above. The technique is called the climbing-image NEB (CI-NEB) [*104*]. In the CI-

NEB, the shape of the MEP is retained, but the highest energy image i_{max} feels no spring forces and climbs to the saddle, via an inversion in the force acting along the tangent, that is,

$$\boldsymbol{F}_{i_{max}}^{CI} = \boldsymbol{F}_{i_{max}} - 2\boldsymbol{F}_{i_{max}}.\hat{\boldsymbol{\tau}}_{i_{max}}\hat{\boldsymbol{\tau}}_{i_{max}} , \tag{2.92}$$

or

$$\boldsymbol{F}_{i_{max}}^{CI} = -\boldsymbol{\nabla E}\left(\boldsymbol{R}_{i_{max}}\right) + 2\boldsymbol{\nabla E}\left(\boldsymbol{R}_{i_{max}}\right).\hat{\boldsymbol{\tau}}_{i_{max}}\hat{\boldsymbol{\tau}}_{i_{max}} \tag{2.93}$$

The climbing image (CI) moves up the potential energy surface (PES) along the elastic band and down the potential surface perpendicular to the band. Other images in the nudged band define the only degree of freedom for which the energy maximization is carried out.

It is important to have the best resolution in the MEP near the saddle point, rather than at any other point in the MEP, so as to obtain an accurate saddle-point. This is accomplished by using different spring constants between different pairs of images. Because of nudging, there is no interference between the spring forces that distribute the images along the path, and the true force that brings the elastic band to the MEP. The NEB is such that the spring constant depends linearly on the energy of the images, so that images with low energy get connected by a weaker spring constant. A stronger spring is therefore required near the saddle point to obtain a better resolved the saddle-point. Images with the highest energy are connected by a spring constant k_{max}, while lower energy images are connected by a weaker spring constants [*104*]

$$k_s^{'} = \begin{cases} k_{max} - \Delta k \delta E & if\ E_i > E_0 \\ k_{max} - \Delta k & if\ E_i < E_0 \end{cases} , \tag{2.94}$$

where

$$\delta E = \frac{E_{max} - E_i}{E_{max} - E_0} .$$

and $E_i = max\{E_i, E_{i-1}\}$ is the higher of two images connected by the spring s, E_{max} is the maximum values of E_i for the whole elastic band, while E_0 is the energy chosen as the minimum value of the spring constant. To ensure that the number of images is roughly equal near the two end points, E_0 is usually chosen to be equal to the higher energy end point of the MEP. The spring constant is, therefore linearly scaled from k_{max} to a lowest value $k_{max} - \Delta k$ for images with energy of E_0 or lower. By choosing E_i to be the higher energy of the two images connected by the spring, there is a tendency for the two images adjacent to the climbing image to be symmetric about the saddle point. Finally, it should be mentioned that in addition to the NEB, there are several other techniques of finding the minimum energy pathways for a transition process. These include the doubly-nudged elastic bands method (DNEB) [*114,115*], the evolving string method (ES) [*116*], and the growing string method (GS) [*117*].

2.6 The QUANTUM-ESPRESSO (QE) package

QUANTUM ESPRESSO (QE) [*118*] is an integrated module of computer codes for electronic-structure calculations and material modelling based on the frame work of the density-functional theory, plane-wave basis sets and pseudopotentials to represent the electron-ion interactions. It is free, open-source software distributed under the terms of the GNU General Public License (GPL). The main components of the QE are the following:

PWscf

This implements the iterative approach to self-consistency using different matrix diagonalization techniques in the framework of the plane-wave pseudo-potential (PP) method. With regards to the PP, both norm conserving (NC-PP) and the ultrasoft (US-PP) are implemented. Recently, the projector augmented-wave method has also been added. *PWscf* can use the LDA or the GGA exchange-correlation functionals, including spin-polarization. Other advanced functionals that have

been implemented include the TPSS meta-GGA [*119*], B3LYP [*120*], PBE0 [*121*], and functionals with finite size corrections [*122*]. Self-consistency is achieved via the Broyden method [*65*], and the sampling of the Brillouin Zone (BZ) can be achieved using the special ***k***-points method of Chadi and Cohen [*123*] or that of Monkhorst and Pack [*124*]. BZ integration in metallic systems can be performed by smearing/broadening techniques, such as the Fermi-Dirac, Gaussian, Methfessel-Paxton (m-p) [*98*], and Marzari-Vanderbilt (m-v) [*125*] cold smearing. The tetrahedron method [*126*] is also implemented. Structural optimization in the form of internal, microscopic degrees of freedom or macroscopic ones involving the shape and size of the unit cell can be performed. NEB method is also implemented. Self-consistent calculations, structural relaxations and the NEB related calculations are performed by invoking the executable file called the *pw.x.* Among the most important parameters in the input files of *Quantum Espresso*, we have:

-*ibrav:* specifies the type of Bravais lattice we are simulating, ibrav=1 is for sc, ibrav=2 is for FCC, etc.

-*celldm (i) i=1, 2, 3*: specifies the lattice parameters of the crystal and are usually given in atomic units (au), while *i=4, 5, 6*, are the cosines of the angles between each pair of lattice vectors.

-*ecutwfc*: is the energy cutoff, which limits the amount of plane waves that the program will use during the minimization procedure. The unit, as implement in QE, is in Ry.

-*nat:* specifies the number of atoms in a unit cell. For example, for HCP Ti, *nat = 2.*

-*ntyp:* is number of atomic species i.e. how many different kinds of atoms are involved in the simulations

-*ATOMIC SPECIES:* a section where one specify the symbols of the atoms, their corresponding masses (as written on the periodic table) and the name of the files containing the pseudo-potentials.

-*ATOMIC POSITIONS:* here the atomic coordinates of the atoms are specified. The allowed degrees of freedom of the atoms can also be specified.

-*k points:* is the number of points in the reciprocal space that the program is supposed to sample, i.e. the points in which the actual self consistent minimization of the energy will be performed.

PostProc

The *PostProc* module contains a number of codes for post-processing and analysis of data files produced by *PWscf*. It contains utilities such as the following:

-*dos.x:* calculates the electronic density of states (DOS).

-*plotrho.x*: produces the 2-dimensional charge density contour plot.

-*bands.x*: extracts and reorders eigenvalues from files produced by the pw.x for band structure plotting.

plotband.x: reads the output of bands.x, and then produces the band structure plots.

projwfc.x: calculates the projections of wavefunction over atomic orbitals, performs Löwdin population analysis, and calculates projected density of states (PDOS).

Other modules [*127*] in QE includes the *PHonon* for phonon related calculations using the density functional perturbation theory (DFPT) [*128*], CP for performing Car-Parrinello Molecular Dynamics [*129*], Wannier 90 [*130*] that calculates maximally-localized Wannier functions in metals or insulators.

CHAPTER 3

Modelling the bulk properties of α(h. c. p)-Titanium

As a preliminary step towards the study of intrinsic and foreign defects in hexagonal closed-packed (h.c.p) titanium [*131*], we have studied the ground-state structural and electronic properties of its perfect crystalline structure, and compared these with experimental results. This is necessary to assess the reliability of the pseudopotential (PP), although it must be stressed that arguably the true figure of merit of a PP is not how well it reproduces the experiment, but how well it matches the results of all-electron calculations when using otherwise similar methods [*56*]. Nevertheless, an important criterion for a PP to be used in complex calculations is that it reproduces the ground state experimental values within acceptable errors. With regards to metals, structural properties that are usually calculated include the lattice parameters, equilibrium volume, bulk modulus, Poisson's ratio and the elastic constants. In this chapter, we calculate all of these quantities, and results are also given for electronic properties, such as the band structure and the density of states (DOS). We then compared our results with previous theoretical calculations and experimental data.

3.1 Computational methodology

All the DFT calculations have been performed using the QUANTUM-ESPRESSO [*127*] package. The PP used for titanium in that of Vanderbilt's USPP, taken from the library of the QE package. The atomic configuration for the PP construction consists of twelve electrons in the valence shells: $3s^2\ 3p^6\ 4s^2\ 3d^2$. The cut-off radii for the *s, p, d*, orbital components were taken to be r_{cs} =1.8, r_{cp} =1.8, and r_{cd} = 2.0 in atomic units (a.u), respectively. The inner cut-off radii of

the L-components (L = 0, 1...4) for the conservation augmentation charges are $r_{in}^{L} = 1.2\ a.u$ (Eqn. 2.76). Exchange and correlation effects were treated within the GGA using the Perdew and Wang [PW91] interpolation formulas [*72*]. Non-linear core correction [*94*] to the charge density was included in the calculation of exchange-correlation functional. The above choice of parameters allows one to achieve a very good energy convergence of within ~ 0.01 eV, using an energy cut-off of 435 eV for the pseudo-wavefunctions, and 3400 eV for the augmentation functions $\varrho_{\alpha\beta}(\boldsymbol{r})$ (Eqn. 2.68c). Calculations were performed using plane-waves having up to a 612 eV kinetic energy, but convergence with respect to the total energy, within 0.002 eV/atom, was achieved for 476 eV. Hence this value has been used throughout the work presented in this thesis. In addition, convergence of the total energy (within 0.002 eV/atom) with respect to the discrete Brillouin Zone (BZ) sampling was achieved for 8 × 8× 8 Monkhorst-Pack grid [*97*]. This corresponds to 80 irreducible *k*-points. The BZ integration has been performed with the smearing technique of Methfessel-Paxton [*98*] and a smearing width $\sigma = 0.272$ eV. Our checks have shown that this width results in a satisfactory convergence of all the calculated quantities.

Titanium is a transition metal that crystallizes in the hexagonal closed-packed (h.c.p) structure [*132*]. The h.c.p structure is often referred to as the α-titanium. Although, other phases of titanium exist, such as, β (bcc) [*133*], γ (distorted bcc) [*134*], δ [*135*] and the ω (hexagonal) [*136,137*], although the transition from the α-phase to other phases usually occurs at high temperature or pressure. The primitive hexagonal unit cell has axes $\boldsymbol{a_1} = \boldsymbol{a_2} \neq \boldsymbol{c}$ and the corresponding angles $\alpha = \beta = 90^0$, $\gamma = 120^0$. The shortest distances between atom centres along the $\boldsymbol{a_1}$ and $\boldsymbol{a_2}$ is usually taken as *a*, and along the $\boldsymbol{c}$-axis as *c*. The axial ratio c/a is $\sqrt{8/3} = 1.633$ [*138*] for an ideal hexagonal closed-packed metal. The equilibrium lattice

parameter a and the bulk modulus for the h.c.p titanium were obtained from the calculation of the total energy as a function of volume, which are then fitted to the Murnaghan's equation of state [*139*] of the form

$$E(\Omega) = \frac{B_0}{B_0^{'}}\left[\frac{(\Omega_0/\Omega)^{B_0^{'}}}{B_0^{'}-1}+1\right] + const \quad , \tag{3.1}$$

where B_0 and $B_0^{'}$ are the bulk modulus and its pressure derivative at the equilibrium atomic volume $\Omega_0 = \sqrt{3}a^2c/4$. For an h.c.p structure, there is an additional parameter to be optimized at any given volume, that is, the c/a ratio. The approach used is as follows: energy was first calculated as a function of a at a fixed c/a ratio close to the experimental, from where the lattice parameter a corresponding to the minimum energy was obtained. By varying the ratio c/a about the experimental value, and keeping the equilibrium volume Ω_0 of the unit cell constant, the equilibrium c/a ratio corresponding to the minimum energy was obtained by fitting the energy and c/a values to the polynomial of the form

$$E(c/a) = \alpha_1(c/a)^3 + \alpha_2(c/a)^2 + \alpha_3(c/a) + ß \quad , \tag{3.2}$$

where $\alpha_i (i = 1, 2, 3)$ and ß are arbitrary fitting parameters. The c/a ratio corresponding to the minimum energy is the equilibrium ratio for titanium at the equilibrium volume.

There are five independent elastic constants in an h.c.p material: $C_{11}, C_{12}, C_{13}, C_{33}$, and C_{55}. These have been calculated with the strain matrices proposed by Fast et al. [*140*]. Five different strains types are needed to determine these constants. If the h.c.p crystal structure that is spanned by three Bravais lattice vectors is written in a matrix form [*140*]

$$\boldsymbol{R} = \begin{pmatrix} 1 & 0 & 0 \\ -1/2 & -\sqrt{3}/2 & 0 \\ 0 & 0 & c/a \end{pmatrix} \quad , \tag{3.3}$$

where each row of the matrix is a vector representing the dimension of the primitive hexagonal unit cell. The distortion of the lattice is written as follows

$$\boldsymbol{d} = \boldsymbol{R}\boldsymbol{\epsilon} \quad , \tag{3.4}$$

where $\boldsymbol{R}$ is as defined above and $\boldsymbol{\epsilon}$ is the distortion matrix. The first distortion matrix changes the dimension of the basal plane while keeping the ***c***-axis constant. They symmetry of the strained structure therefore remains hexagonal. Thus

$$\boldsymbol{\epsilon} = \begin{pmatrix} 1+\delta & 0 & 0 \\ 0 & 1+\delta & 0 \\ 0 & 0 & 1 \end{pmatrix} \quad , \tag{3.5}$$

where δ is the distortion. The energy associated with the distortion is

$$E(V, \delta) = E(V_0, 0) + [(\tau_1 + \tau_2)\delta + (C_{11} + C_{12})\delta^2]V_0 \tag{3.6}$$

The second distortion increases the $\mathbf{a_1}$-axis and decreases the $\mathbf{a_2}$ -axis in equal amounts**,** while the **c**- axis is kept constant. Thus

$$\boldsymbol{\epsilon} = \begin{pmatrix} 1+\delta & 0 & 0 \\ 0 & 1-\delta & 0 \\ 0 & 0 & 1 \end{pmatrix} \quad . \tag{3.7}$$

The symmetry of the strained lattice is therefore monoclinic, and the energy is expressed as

$$E(V, \delta) = E(V_0, 0) + [(\tau_1 - \tau_2)\delta + (C_{11} - C_{12})\delta^2]V_0 \quad . \tag{3.8}$$

By extracting $C_{11}+C_{12}$ and $C_{11}-C_{12}$ from Eqns. 3.6 and 3.8, C_{11} and C_{12} can be calculated. The third strain involves stretching the ***c***-axis, while the other axes remain unchanged. The hexagonal symmetry of the strained object is thus maintained. The distortion is written as

$$\boldsymbol{\epsilon} = \begin{pmatrix} 1 & 0 & 0 \\ 0 & 1 & 0 \\ 0 & 0 & 1+\delta \end{pmatrix} \quad , \tag{3.9}$$

giving C_{33} from the relation

$$E(V,\delta) = E(V_0,0) + (\tau_3\delta + \frac{C_{33}}{2}\delta^2)V_0 \quad . \tag{3.10}$$

The fourth elastic constant, C_{55} is obtained by deforming the lattice such that the resulting strained object is of very low symmetry, as in a monoclinic structure. The deformation is written as

$$\boldsymbol{\epsilon} = \begin{pmatrix} 1 & 0 & \delta \\ 0 & 1 & 0 \\ \delta & 0 & 1 \end{pmatrix} \quad . \tag{3.11}$$

The energy can be written as

$$E(V,\delta) = E(V_0,0) + (\tau_5\delta + 2C_{55}\delta^2)V_0 \ , \tag{3.12}$$

and this gives directly the C_{55}. The last constant C_{13} may be obtained by deforming the lattice according to the matrix

$$\boldsymbol{\epsilon} = \begin{pmatrix} 1+\delta & 0 & 0 \\ 0 & 1+\delta & 0 \\ 0 & 0 & 1+\delta \end{pmatrix} \ , \tag{3.13}$$

and the expression for energy is

$$E(V,\delta) = E(V_0,0) + ((\tau_1+\tau_2+\tau_3)\delta + \ (C_{11}+C_{12}+2C_{13}+C_{33}/2)\,\delta^2)V_0 \ . \tag{3.14}$$

If the bulk modulus *B* is defined as

$$B = \frac{1}{9V_0}\frac{d^2E}{d\delta^2} \ , \tag{3.15}$$

and applying this definition to Eqn. 3.14, the relationship between the elastic constants and the bulk modulus can be obtained thus

$$B = \frac{2}{9}(C_{11} + C_{12} + 2C_{13} + C_{33}/2) \tag{3.16}$$

The total energy $E(V, \delta)$ is obtained self-consistently while allowing internal relaxations for each of the deformed cell.

Poisson's ratio [*141*] σ is the negative ratio of the transverse strain to the corresponding axial strain in a body subjected to a uniaxial stress. In a hexagonal system, it is usually calculated by keeping the value of *c* fixed, and determining the total energies as the *a* values are varied. The results of energy versus *a* are then fitted to a parabola, and the minimum value of *a*, that is, a_{min} is obtained. The procedure is repeated for different values of fixed *c* and varying *a*. Poisson ratio is then obtained from the slope of *c* versus *a* (a_{min}), [*142*]

$$\sigma = -(\Delta a/\Delta c)(c/a) \tag{3.17}$$

where $\Delta a/\Delta c$ is the slope of the fit, and c/a ratio is the calculated equilibrium ratio.

With regard to the electronic structure of titanium, Fig.3.1 shows the Brillouin Zone (BZ) in the hexagonal closed-packed structure [*143,144*]. The energy bands are usually calculated along symmetry directions define by high symmetry points as shown in the figure. The coordinates of the points in the units of $2\pi/a$ are: $\Gamma\ (0,0,0)$; $A\ (0,0,a/2c)$; $M\ (1/\sqrt{3},0,0)$; $K\ (2/2\sqrt{3},1/2\sqrt{3},0)$; $H\ (1/2\sqrt{3},1/2\sqrt{3},1/\sqrt{3})$; $L\ (1/\sqrt{3},\ 0,1/2\sqrt{3})$. The coordinates along

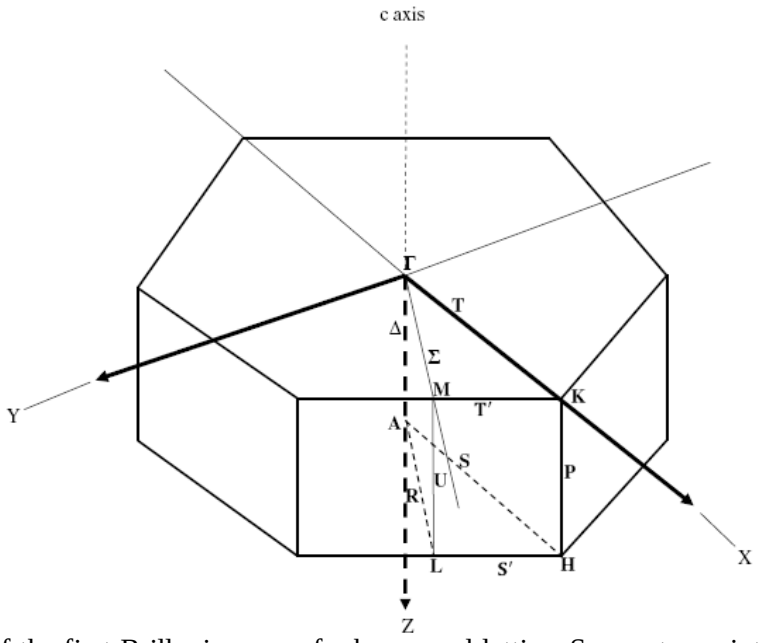

Fig. 3.1 Schematic of the first Brillouin zone of a hexagonal lattice. Symmetry point and symmetry lines are shown

the symmetry lines are: Σ [ξ, 0, 0] with $0 < \xi < 1/2$; T [ξ, ξ, 0] with $0 < \xi < 1/3$; T → T^1 with $0 < \xi < 1/2$; Δ [0, 0, ξ]; U [1/2, 0, ξ], P [1/3, 1/3, ξ], and R [ξ, 0, 1/2] with $0 < \xi < 1/2$; S [ξ, ξ, 1/2] with $0 < \xi < 1/3$, and finally, S' [ξ, ξ, 1/2], T' [ξ, ξ, 0] with $1/3 < \xi < 1/2$. The density of states (DOS) per unit energy *E*, is given as

$$\rho(E) = \frac{1}{n_k} \sum_{i,k} \delta(\varepsilon_{i,k} - E) \ , \tag{3.18}$$

and in an extended object, $\rho(E)$ is defined per unit volume Ω. Thus [*70*]

$$\rho(E) = (\Omega_{BZ})^{-1} \int d\boldsymbol{k}\, \delta\left(\varepsilon_{i,k} - E\right) \ , \tag{3.19}$$

where Ω_{BZ} is the volume of the Brillouin zone and the integration is over the zone, n_k is the number of $\boldsymbol{k}$ points in the BZ, and $\varepsilon_{i,k}$ denotes the energy of an electron. The density of states $\rho(E)$ may be defined as the number of independent-particle states per unit energy.

3.2 Results and Discussion

3.2.1 Physical Properties: Equilibrium Structure and Elastic Properties

The curves of $E(a)$ at $c/a = 1.587$ and $E(c/a)$ at $a = 2.950$ Å, from which lattice parameters are deduced are shown in Fig 3.2a and 3.2b, respectively. The parameters obtained are given in Table 3.1 along with the relative phase stabilities of three different phases of titanium [145]. Fig. 3.3 shows the linear fit of variation of a_{min} with *c*. For given four different values of *c* (0.88, 0.91, 0.95, 1.03, in units relative to the *c* experimental value). A straight line was fitted through the energy calculated at five *a* points (0.91, 0.96, 1.02, 1.07, 1.12, in the units of *a* experimental value). The slope of the graph is used with Eqn. 3.17 with $c/a = 1.585$, and the Poisson ratio is thus obtained. Agreements with experiments [146,147] are generally good (within an error of ~2%) for the calculated physical parameters. Compared with previous theoretical calculations, our results are also in good agreement with the *ab inito* calculations performed using the linearised augmented plane wave (LAPW) [147] and the GGA-full potential-linear-muffin-tin (FP-LMTO) methods [148,149]. With regards to relative phase stability however, our GGA calculation predicts a stable ω phase under zero pressure in contrast to experimental results. The energy difference between the α and ω phases are however very small, i.e. ~0.01 eV/atom. From the available experimental data [150] however, the ω phase is higher in energy than the α -phase by ~0.02 eV/atom. The error we make in our calculation therefore is ~0.03 eV/atom, which is still within the accuracy of DFT calculations. In addition, similar *ab inito* calculations of Trinkle et al. [151] show the ω phase to be slightly lower in energy at zero applied external pressure. It should be mentioned also that GGA corrections usually overestimate the equilibrium volume (Ω_0) and underestimate the bulk modulus (*B*). Across the transition metal (TM) series,

however, and in agreement with our results, the tendency to underestimate Ω_0 in the beginning of the series (such as in Ti and V), and to overestimate Ω_0 at the end of the series (such as in Os, Ir and Pt), is a well established trend [151].

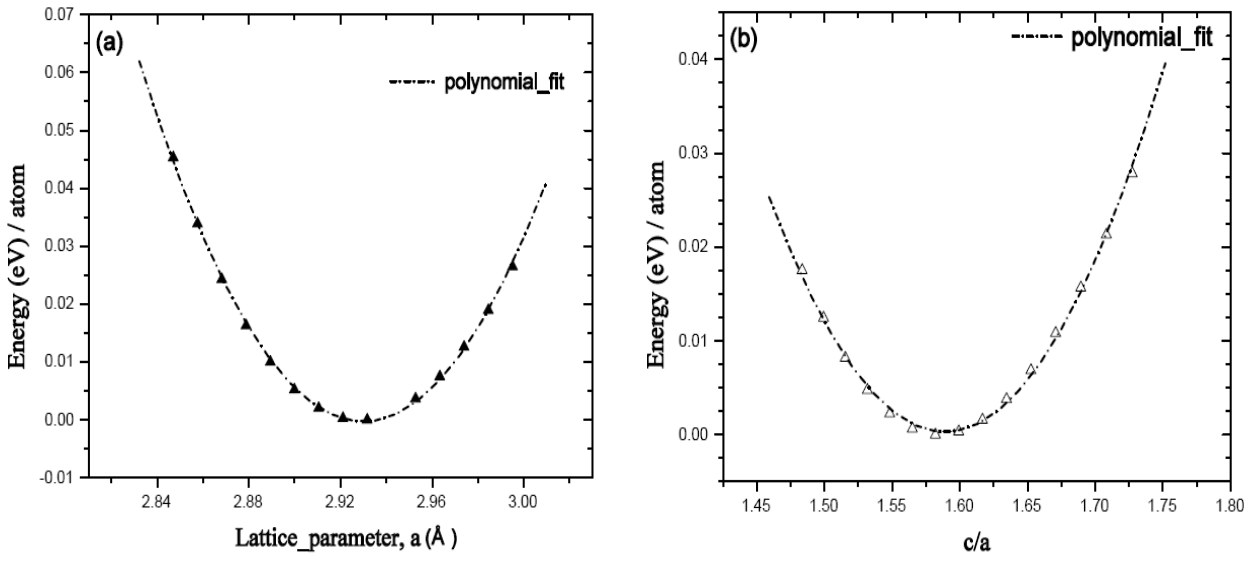

Fig 3.2: Energy variation with (a) lattice parameter, a (b) c/a ratio for α-Titanium

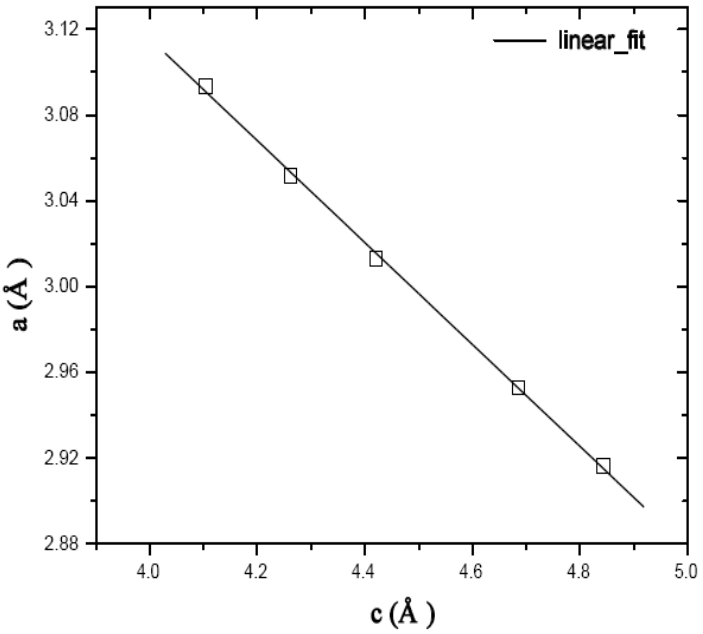

Fig 3.3 Linear relationship between c and $a_{min,}$ the slope of which gives the Poisson's ratio at $c/a = 1.585$.

Table 3.1 Results for the equilibrium lattice constant a_0, equilibrium volume Ω_0, bulk modulus B_0, and the c/a ratio of α (h.c.p)-titanium structure, in comparison with experimental data. Results for the ω and bcc relative phase stabilities (in eV/atom) test are also included. The two values under published theory in reference [147] are due to two different exchange-correlation potentials. $E_{h.c.p}$, E_{ω}, and E_{bcc} are the energies of the h.c.p, ω and the α (bcc) phases of titanium.

	a_0 (Å)	B_0(GPa)	σ	Ω_0 (Å^3)	c/a	E_{ω} - $E_{h.c.p}$	E_{bcc} - $E_{h.c.p}$
Present work	2.930	112	0.38	17.26	1.585	-0.01	0.11
Published Theory						-	-
LAPW	2.866[b], 2.925[b]	127[b], 108[b]	0.34[b], 0.29[b]	16.18[b], 17.29[b]	1.586[b], 1.595[b]		
FP-LMTO		108[c], 125[d]			1.585[c], 1.589[d]		
Experiment	2.9506[a]	110[a]	0.36[a]	17.64[a]	1.586[a]	-	-

[a]Reference 146.
[b]Reference 147.
[c]Reference 148.
[d]Reference 149.

In Fig.3.4, the total energy of distorted titanium primitive unit cell as a function of the distortion parameter are shown. The points in each of the figures have been fitted to a polynomial from which the second order coefficients are extracted, and the elastic constants calculated according to Eqns. 3.6, 3.8, 3.10, 3.12 and 3.14. The total energy has been calculated for five different distortions, δ = -0.02, -0.01, 0.00, 0.01, and 0.02 for everyone of the five different deformations of the lattice. Since the α-titanium is not centro-symmetric, internal relaxations were allowed for each deformation of the cell. We also performed convergence test of the number of *k*-points using the deformation for the C_{33} elastic constants. It was confirmed that the total energy is converged for an 8 × 8 × 8 mesh. This mesh size was then used to calculate the total energy for every distortion. In Table 3.2, we summarize the calculated elastic constants and compare with experimental results.

Overall, the agreement with experiment [152] is good in light of the expected density functional error for elastic constants of metals. The agreement is satisfactory for the bulk modulus *B*, and the elastic moduli C_{11} and C_{33}. Also, using the theoretical data of Table 3.1 and Eqn. 3.16, the calculated bulk modulus B_0, is in good agreement with the 112 GPa, obtained from the Murnaghan fit. However, the shear moduli C_{12} and C_{44} are underestimated, while C_{13} is overestimated. The main problem with C_{12} and C_{13} may be due to unfavourable error propagation in the evaluation of

Table 3.2. Elastic constants (in GPa) and the bulk modulus B_0 of h.c.p Ti, as calculated in the present work, and compared with the experimental values [152] at 4^0K.

	C_{11}	C_{12}	C_{13}	C_{33}	C_{55}	B_0(GPa)
Present work (GGA)	194	69	80	175	41	114
Experiment	176	87	68	191	51	110

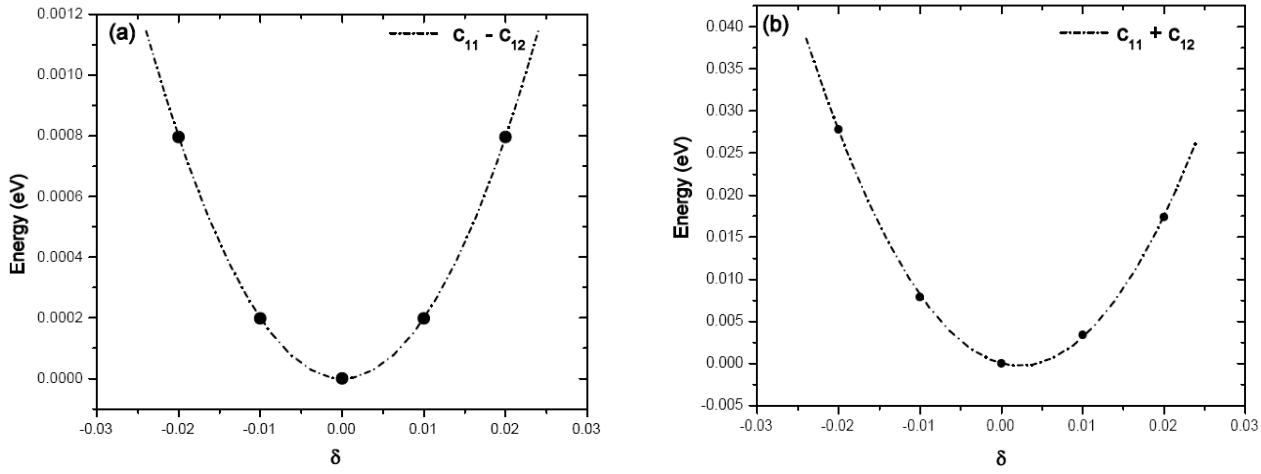

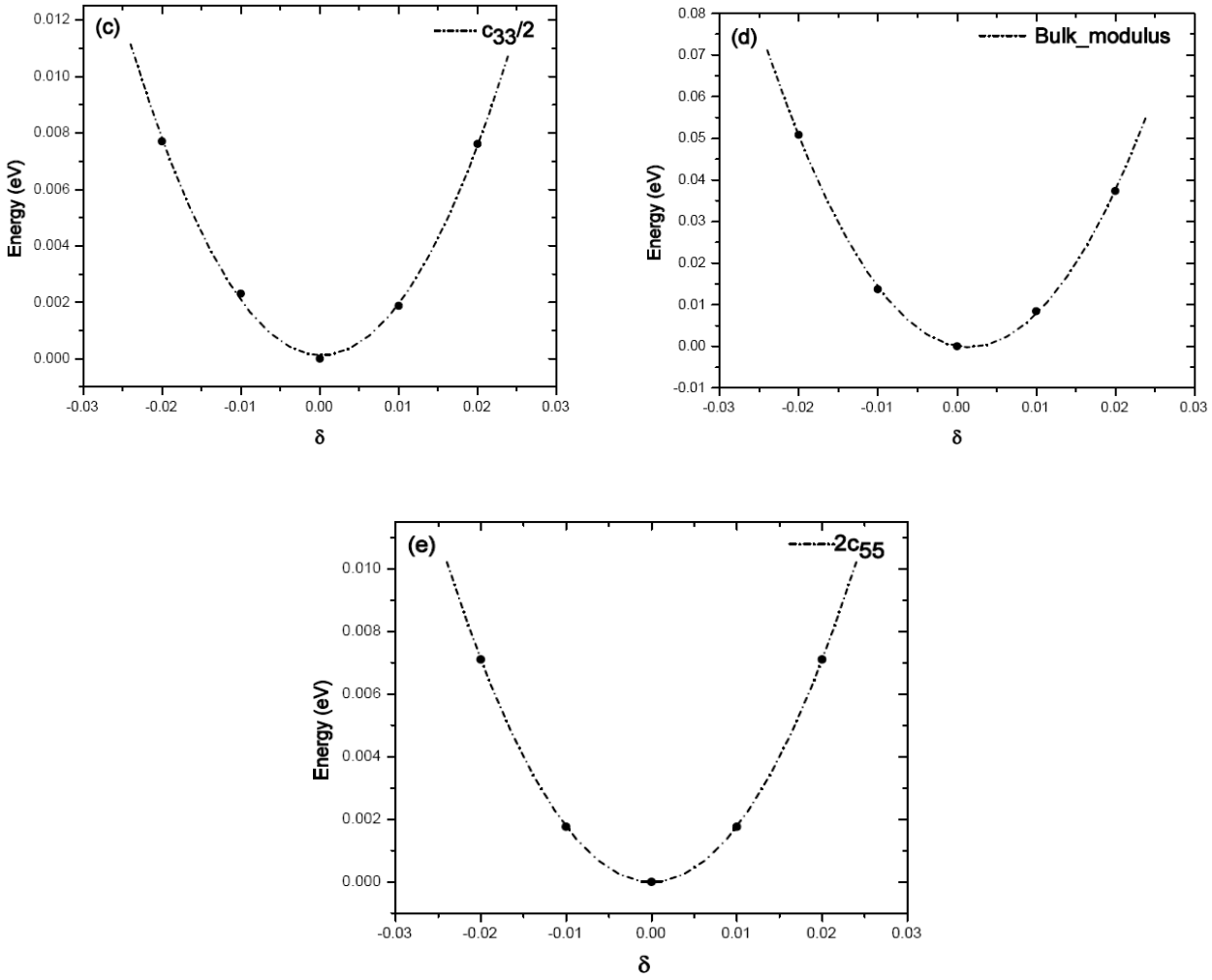

Fig. 3.4 Total energy of titanium as a function of lattice distortion parameter δ for the five different lattice deformations described in the text. Panels (a-e) correspond to distortions given by Eqns. 3.6, 3.8, 3.10, 3.12 and 3.14, respectively.

these elastic constants. The deformations [140] used to extract C_{12} and C_{13} involve a linear combination of elastic constants which are twice as large as C_{12} and C_{13}. Consequently, the relative error associated with the deformations is increased for each. Furthermore, the error in C_{12} may not be only attributed to calculation, but also due to experiment as C_{12} is known to be particularly sensitive to experimental error [153]. As regards to C_{55}, the same error margin (~ 20%) has been reported in previous [142,31] GGA calculations in h.c.p Zr and none of the

authors gave reasons for such relatively large error. However, deviations between theory using DFT and experiment for elastic constants are in the region of ±30% [140].

3.2.2 Electronic properties: bands and density of states (DOS)

The band structure and the density of states of h.c.p titanium have been previously calculated by several authors, using a variety of techniques. These include calculation by Jepsen [154] which employ the linear muffin-tin-orbital (LMTO) method with Slater type approximation for the exchange and correlation; numerical calculations using linear combination of localized Gaussian orbitals by Feibelman et al. [155], augmented-plane-wave (APW) calculations by Hygh et al. [156], Welch et al. [157], and the self-consistent full potential linear APW calculations by Blaha et al. [158] and Lu et al. [147]. All of these calculations used either $3d^2 4s^2$ or $3d^2 4s^1$ atomic configurations in contrast to $3s^2\ 3p^6\ 3d^2\ 4s^2$ that have used in the calculations reported here. In addition, details of the potentials and approximations or corrections used are different from ours. Moreover, we have not included spin polarization effect in our calculations, as has been done in Refs. [147,154,158]. Therefore, our results may differ in some details when compared with these earlier studies. The band structure calculation reported here has been performed at the calculated lattice parameters shown in Table 3.1. We show in Fig. 3.5 shows the calculated band structure of h.c.p titanium along the high symmetry lines as earlier mentioned in section 3.1. The occupied valence bandwidth is about 5.9 eV which compares well

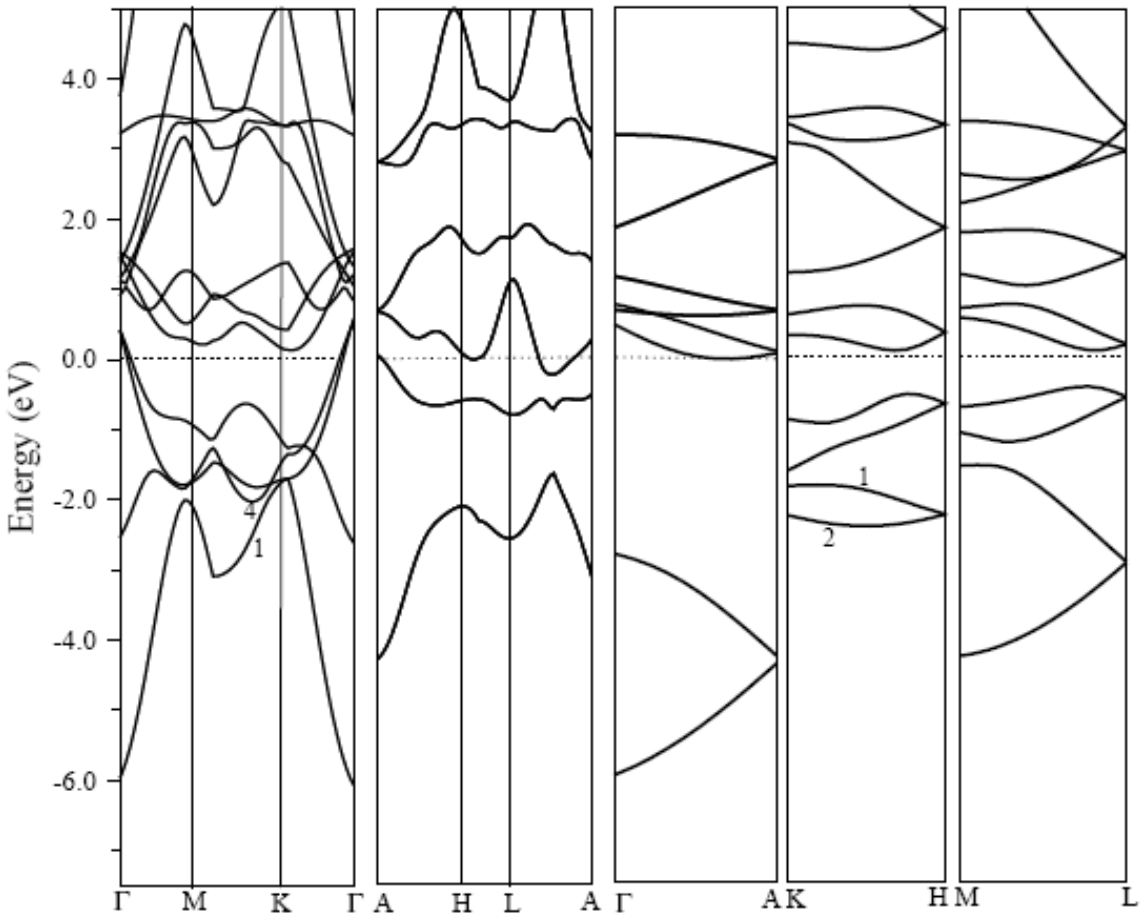

Fig. 3.5. Band structure for α −Titanium using the GGA-plane-wave pseudopotential method.

with 6.1 eV of Blaha et al. [158]. The occupied bandwidth is the difference between the Fermi energy and the energy at the lowest state at Γ. Compare to studies by Lu et al. [147] and Jepsen [154], we too find the double intersection of the $\Gamma - A$ band with the Fermi energy, consistent with the experimental de Haas-van Alphen results [159]. However, along the line K – H, they reported a band crossing and dipping slightly below the Fermi level, whereas our calculation does not show that. In addition, Jepsen [154] reported two almost degenerate bands along the K – H and K – M directions. These bands, labelled 1, 2, and 1, 4 in Fig. 6, are split in our calculations

and are also nondegenerate in the self-consistent nonrelativistic bulk band structure calculations of Feibelman et al. [155].

Our calculated density of states (DOS) is shown in Fig. 3.6. The calculation was carried out using the tetrahedron method [126] with discrete mesh corresponding to 800 *k*-points in the primitive Brillouin Zone. The DOS curve reported here exhibits three characteristics energy gaps

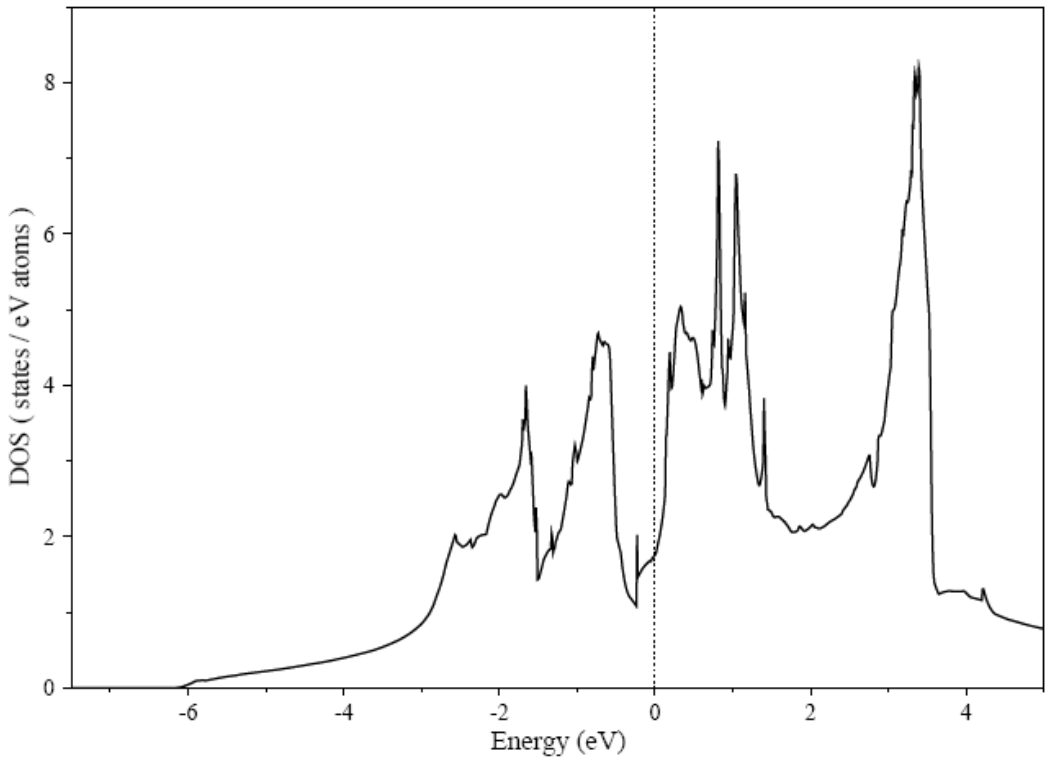

Fig.3.6. Density of states (DOS) of α −Titanium calculated using the GGA plane-wave pseudopotential method. The Fermi energy is indicated by the dashed line.

which are typical of h.c.p metals. The DOS is primarily *d*-like, showing two narrow peaks around the Fermi energy, which falls on the high-energy side of a relatively sharp minimum. The small peak just below the Fermi energy is due mostly to contribution from *p*-electron.

The DOS at the Fermi level is ~1.9 states/eVatoms. This value is in excellent agreement with the calculations of Jepsen [154], Hygh et. al [156], and Vohra [160] who reported 1.8 states/eV atoms, 2.1 states/eV atoms, and 2.2 states/eV atoms, respectively. The low numbers of electrons at the Fermi level, as well as the location of the Fermi level are consistent with observations from experimental studies on transition metal series by Eastman [161].

CHAPTER 4

Intrinsic defects in α(h. c. p)-Titanium: formation and migration

Vacancies are the simplest lattice defects, and many properties of solids, such as, optical, electrical and mechanical properties depend directly on their concentration [*162*]. Vacancies also play an important role in determining the surface morphology of metals [*163*]. Vacancies generally have lower formation energy than self- interstitial atom, and hence in thermal equilibrium the monovacancy mechanism is widely accepted as the dominant mechanism for atomic diffusion [*164*]. However, for a metal subjected to irradiation or ion implantation [*9*], the situation may be different due to the high concentration of vacancies and self interstitial atoms (SIA) that may be produced [*11*]. In this case, it has been suggested that the SIA mechanism may be dominant [*165*]. The macroscopic behaviour of cubic metals due to damage production and accumulation may be explained in term of reaction kinetics governed by the isotropic migration of vacancies and interstitials [*166*]. However, because of crystallographic anisotropy, diffusion of lattice defects in hexagonal-closed-packed metals can be expected to be anisotropic [*167*]. A clear understanding of the behaviour of h.c.p metals during and after radiation therefore requires information on the intrinsic defects generated, and the anisotropy of migration of both vacancies and interstitials in particular. In this chapter, we report on the energetics of formation of a monovacancy and divacancy, as well the anisotropic migration of a monovacancy and self interstitial atom (SIA) in α-Titanium, using the supercell approach [*56*]. We also studied the electronic structure around a single vacancy.

4.1 Computational methodology

4.1.1 Supercell and other methods

A popular way to calculate defect energetics from first-principles, that is from the electronic degrees of freedom, is based on the supercell approach [*56*]. In this method, the atoms defining the region of interest are confined into an otherwise arbitrary box, which is then repeated infinitely in one or more spatial directions. The supercell then becomes the unit cell of the system, and periodic boundary conditions are applied at one or more of its boundaries. The supercell method is the main technique for defect calculations, aside from the Green-functions embedding techniques [*168*] and the finite-cluster methods [*169*]. The second is often considered to be the best way to study isolated defects and the implementation is done in such a way that the perturbed defect region is matched to the known DFT Green's function of the unperturbed host material. The Green's function method is mathematically elegant, but the numerical effort involved is challenging for an accurate description of interatomic forces and long-range atomic relaxations, as it requires a well localized defect potential and usually short-range basis functions. In the finite-cluster methods, the defect of interest is simply incorporated into a finite atomic cluster. The method is well suited for local defect properties, such as vibrational modes and defect-related hyperfine fields, provided that the atomic cluster size is sufficiently large to minimize any surface effects. Nevertheless, the supercell method [*56*] has gained enormous popularity in studying defect related calculations. The great advantage of this approach is that the periodic boundary conditions allow the utilization of the many efficient techniques derived for the quantum physics of periodic systems. For example, the standard band structure methods of periodic solids can be applied to a supercell by taking advantage of the fact that the wave-vectors

of the Brillouin zone in the reciprocal space of the supercell are good quantum numbers. Fast and efficient computation methods [*110*] can be performed by using Fourier analysis as they naturally adapt to periodic boundary conditions. In addition, the supercell method also allows full relaxation of the structure and volume in order to minimize the total energy [*170*]. However, in spite of the advantages of the supercell method, there are drawbacks, especially when applied in defect calculations. The periodicity of supercell is artificial and can lead to spurious interactions between the defects. They have a finite density, which may not necessarily be the true physical representation, usually characterized by an aperiodic, low density defect distribution. Also, point defects induce elastic stress in the host-lattice, which is relieved by lattice relaxation through ionic displacement [*171*]. The long range ionic relaxations, however, may not be correctly described, especially when defects such as self or foreign interstitial atoms, larger than the host lattice atoms are involved. This is because the lattice relaxation pattern is restrained by the supercell geometry, or the supercell symmetry itself may fix the positions of the ions at the borders [*172*]. When the supercell method is applied in defect studies therefore, an examination of the finite-size and periodicity effects should always be carried out [*173*].

As regards charged defects [*174,175*], divergence in electrostatic energies may occur. A popular solution is to introduce a fictitious neutralizing background charge, often in the form of a uniform jellium distribution to the supercell array. This, however, introduces an artificial long-range electrostatic interaction between the periodic charge distribution in the supercell, and the jellium background. In principle, this should be negligible in the limit of infinitely large supercells. However, this is not always guaranteed, and therefore corrections due to the influence of the artificial neutralizing charge are made to the total energy calculations. This is usually

referred to as the Madelung or electrostatic correction [*176*]. Parameters that may be obtained from supercell calculations include the probabilities of certain types of defects to form in materials, nature of defect electronic states, migration barriers, and vibration modes, among other properties.

4.1.2 Energy of formation and relaxation volumes of defects

If we define *N* as the total number of atoms in a perfect defect-free supercell, the formation enthalpy of such a system containing *n* number of vacancy can be calculated using the expression [*177*]

$$H_{ni}^{f} = E(N-n, n, V_v) - \frac{N-n}{N} E(N, 0, N\Omega_0) + p(V_v - (N-n)\Omega_0)\,, \qquad (4.1)$$

where $E(N-n, n, V_v)$ denotes the total energy of a relaxed supercell, obtained by removing *n* atoms from an ideal supercell containing *N* atoms; volume V_v corresponds to the relaxed volume of the supercell at pressure *p*; Ω_0 is the equilibrium volume of one atom at pressure *p* in the perfect lattice. Thus *n* = 1, 2 corresponds to a mono- and divacancy respectively. However, in this study, all the calculations have been performed at zero external pressure, and thus $H_{nv}^{f} = E_{nv}^{f}$ for *n* = 1, 2, is the vacancy and divacancy formation energy respectively. Obviously, the calculation of E_{nv}^{f} requires two supercell calculations with periodic boundary conditions. In order to ensure error cancellations, the bulk energies $E(N, 0, N\Omega_0)$ were calculated using the same $\boldsymbol{k}$ points mesh as $E(N-n, n, V_v)$. Also, the value N in Eqn 4.1 must be sufficiently large to minimize the interaction between vacancies in different supercells. The volume relaxation due to effect of the formation of *n* vacancies can be obtained by minimizing the energy of the supercell with *n* vacancy with respect to homogenous volume changes. The formation volume

V_{nv}^{F} is thus obtained as the difference between the volume gained by rigidly removing n atom from the bulk, $(N-n)\Omega_0$, and the volume lost $V^{'}$, when the n vacancy is fully relaxed in the supercell. Thus [*178,179*]

$$V_{nv}^{F} = V^{'} - (N-n)\Omega_0 \quad . \tag{4.2}$$

The relaxation volume V_{nv}^{r} due to defect formation is therefore expressed as $V_0 - V_{nv}^{F}$, for single vacancy defect where V_0 is the volume of a perfect unrelaxed supercell. Attraction or repulsion between defects can be quantified through the calculations of the defects binding energy. In the case of a divacancy, the binding energy, E_{2v}^{b}, of the two vacancies making up the divacancy is defined as follows [*177*]

$$E_{2v}^{b} = 2E_{1v}^{f} - E_{2v}^{f} \quad , \tag{4.3}$$

where E_{1v}^{f} and E_{2v}^{f} are the mono- and divacancy formation energies, respectively. According to this definition, a positive or negative binding energy implies a stable or metastable divacancy configuration with respect to two isolated monovacancies. The formation enthalpy of an interstititial configuration is defined as

$$H_{ni}^{f} = E(N+n, n, V_i) - \frac{N+n}{N}E(N, 0, N\Omega_0) + p(V_i - (N+n)\Omega_0) \quad . \tag{4.4}$$

Here $E(N+n, n, V_i)$ denotes the total energy of a relaxed supercell containing n additional atoms at volume V_i. As in the case of Eqn. 4.1, at zero applied external pressure, $H_{ni}^{f} = E_{ni}^{f}$, the formation energy of the interstitial atom. The formation volume of an interstitial defect is defined as [*180, 181*]

$$V_{ni}^{F} = V_i - (N + n)\Omega_0 \tag{4.5}$$

where n is the number of extra atoms inserted into the supercell, and V_i is as defined in Eqn 4.5. The relaxation volume V_{ni}^{r} of the interstitial is then defined as $V_0 + V_{ni}^{F}$.

Three different divacancy configurations and eight different interstitial configurations, shown in Figs. 4.1 and 4.2 respectively, have been studied in this work. The three divacancy configurations are termed the *in-plane*, the *off-plane*, and the *basal-basal* configurations. They are termed D_{v1}, D_{v2} and D_{v3} respectively. In the in-plane configuration,D_{v1}, the two nearest adjacent atoms of the same plane are missing; the off-plane configuration, D_{v2}, has one of the atoms missing in the basal plane, and the other missing at the closest position off basal plane. In the basal-basal, D_{v3} divacancy configuration, there are two missing atoms at the centre of two basal planes separated by the distance *c*, the lattice parameter along *c*-axis of the hexagonal-closed-packed titanium. Thus, D_{v1}, D_{v2}, and D_{v3} corresponds to divacancy at the first, second, and fourth nearest neighbours, respectively.

In naming the eight self-interstitials configurations, shown in Fig. 4.2, we have adopted the notation of Johnson and Beeler [*182*]. The site marked *O* has an octahedral coordination, the interstitial site *S* denotes a <001> split dumb-bell, and has two atoms jointly sharing the same site in the *c*-direction; configuration *C* is often termed the pseudocrowdion, and is the site midway between the two nearest neighbour atoms separated by two atomic planes, along the *c*-direction. Configuration *T* has tetrahedral coordination. *BT*, *BC*, and *BO* are basal projections of tetrahedral, pseudocrowdion, and the octahedral configurations, respectively. Supercells consisting of up to *N* = 96 atomic sites have been used to study the monovacancy properties and

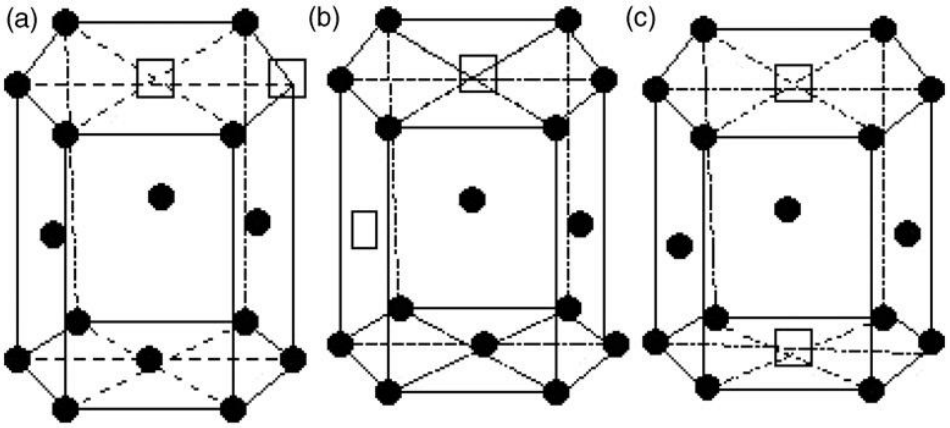

Figure 4.1. Divacancy configurations (a) D_{v1}, (b) D_{v2} and (c) D_{v3} in the hexagonal closed -packed structure, as studied in this work. Filled black circles (●) are regular atomic sites, while open squares (□) are vacancy positions.

convergence with respect to cell size, while supercell of size N = 64 atoms have been used in studying D_{v1} and D_{v2} divacancy configurations. For the D_{v3} configuration, N = 72 atoms have been used, while for the interstitials, cell of sizes N = 36, 64, and 96 were used. Supercell of size N = 36 has dimension $3a \times 3a \times 2c$, while that of 48 atoms measures $3a \times 2a\sqrt{3} \times 2c$. For N = 64, 72, the dimensions are $4a \times 2a\sqrt{3} \times 2c$ and $3a \times 2a\sqrt{3} \times 3c$, respectively. The biggest supercell, N = 96 has dimension $3a \times 2a\sqrt{3} \times 4c$. The number of k points needed to converge the result is of course dependent upon the actual cell size. For a larger supercell, a smaller number can be used because of the smaller volume of the Brillouin zone. The k-points mesh for the supercell generally scales with the k-points mesh used to converge the primitive unite cell with respect to energy, smearing width, and so on. Thus, equivalent k-points meshes to the primitive unit cell have been used for the supercells. We have calculated the formation energies for a monovacancy and three divacancy configurations that are shown in Fig. 4.1. The formation energy predicts the thermodynamically preferred defect structure in a material [*183*], while the

binding energy gives an indication of the stability of a particular defect configuration with respect to its constituents [*184*]. The binding energies of the three divacancy configurations have

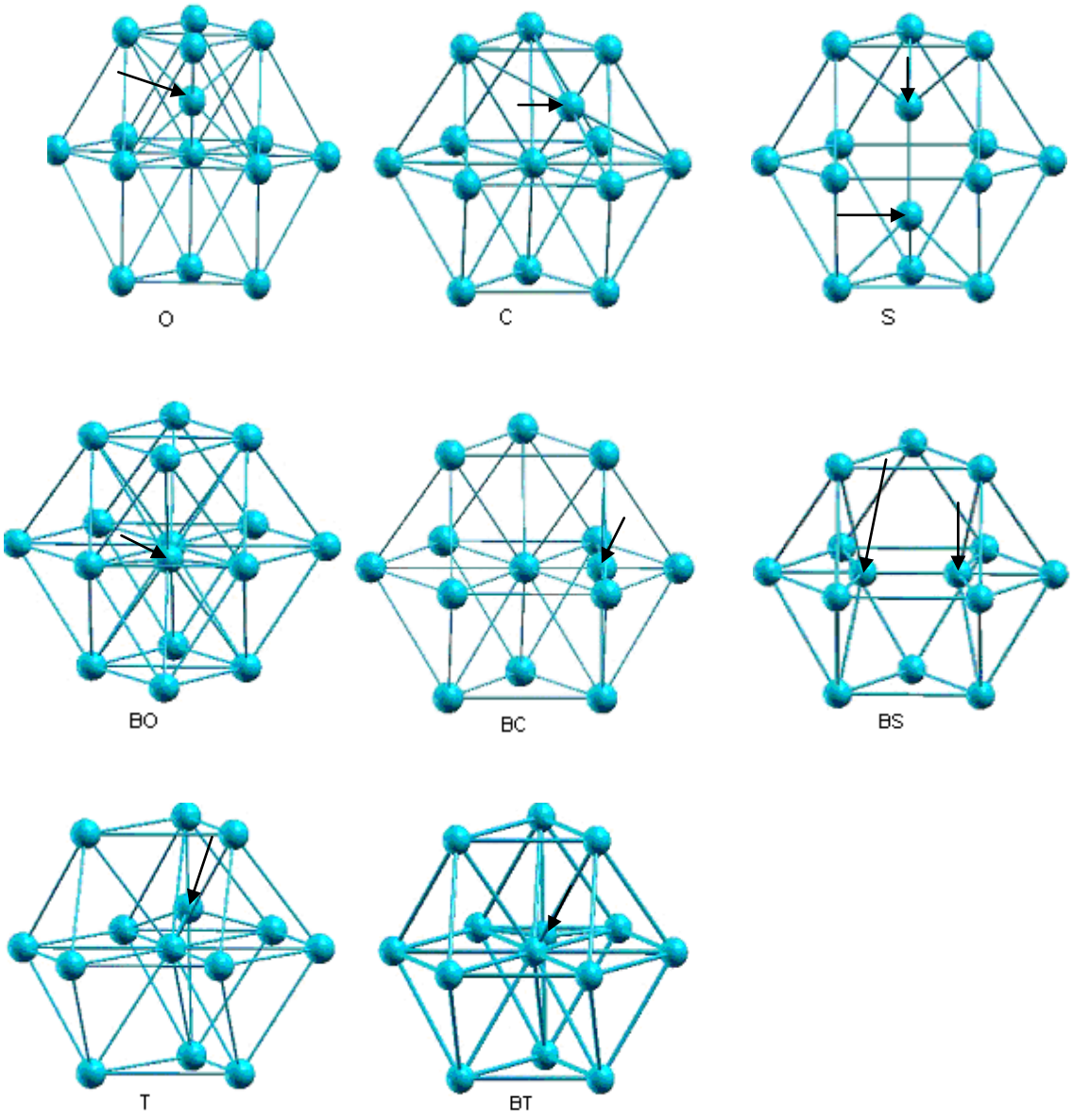

Figure 4.2. Schematics of the initial eight interstitial configurations in the h.c.p structure investigated in this study. Black arrows indicate the position of interstitial atoms.

been determined, while the formation energies and the relaxation volumes of eight different interstitial configurations (Fig. 4.2) were also calculated.

There are two types of monovacancy migration in hexagonal closed-packed crystal due to the crystal symmetry [*185*]: the *in-plane* and the *out-of-plane*. These are shown in Fig. 4.3(a) and have been denoted as B_v and A_v respectively in this work. We have studied the migration of these, along with that of divacancy, using the nudged elastic band (NEB) method described earlier in Section 2.4. For the divacancy migration [*186*], a total of four migration paths have been considered. These are D_{ab}, D_{aa}, D_{ba}, and D_{bb} shown in Fig. 4.3 (b-c). Divacancy migration is such that one of the vacancies rotates with respect to the other. On completion of the rotation, the divacancies either preserve their initial configurations or transform into one another. The migration path denoted as D_{bb} is such that the two vacancies remain in the same plane after the rotation. On the other hand, in the case of D_{ab} migration, after completing the migration along its path, the divacancy transforms to the D_{bb} configuration. The vacancies are now in the same plane, and diffusion may therefore proceed via in-plane vacancy migration. The D_{aa} migration on completing its path retains its configuration, while the D_{ba} transforms into the D_{ba}. The monovacancy and divacancy minimum energy path (MEP) have been determined using the $N = 48$ and $N = 64$ atomic sites supercell respectively. For a single vacancy migration, a total of five images have been used as images in the NEB calculations, while seven images were used for determining the MEP and the activation energy barrier for the divacancy diffusion.

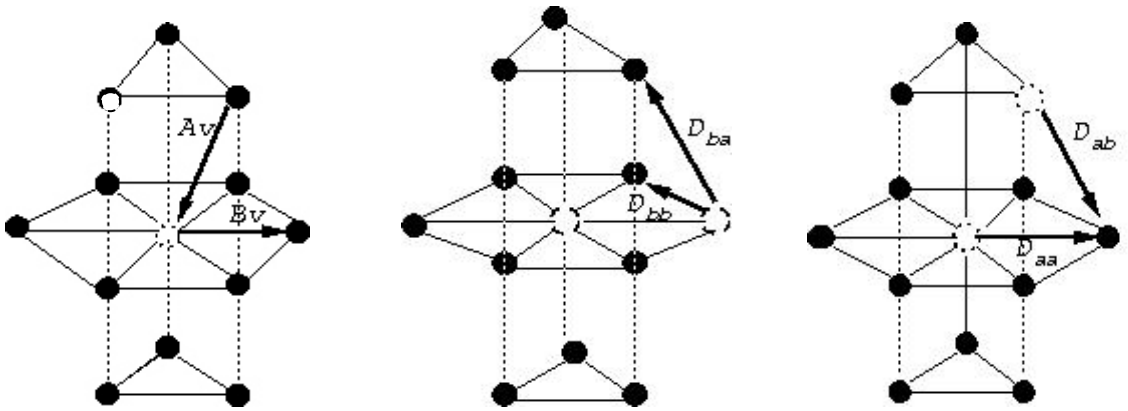

(a) (b) (c)

Fig. 4.3: Schematics of monovacancy and divacancy migration in α (hcp) lattice. (a) *in-plane* (B_v) and off-plane (A_v) migration (b) possible rotations of basal (*in-plane*) divacancy (c) possible rotations of off-plane divacancy. Black filled (●) spheres represent titanium atoms, while open dotted sphere (◌) stand for a vacancy.

4.2. Results and discussion

4.2.1 Formation of vacancy and divacancy

The calculated monovacancy formation energies, E_{1v}^{f} using supercells of sizes, *N = 36, 48, 64, 72, 96* are shown in Table 4.1. The energies have been calculated using the Eqn. 4.1 in section 4.2.2. The fully relaxed results are obtained by performing structural and volume relaxations such that the forces on the atoms are less than 0.03 eV/Å and the pressure in the supercell were less than 0.5 Kbar. The Methfessel-Paxton broadening [*98*] scheme of smearing width ~ 0.27 eV have been used. The value E_{1v}^{f} = 1.92 eV obtained for *N = 48, 64* atom supercell only differs from the value obtained for the largest supercell *N = 96* by only 0.05 eV. In addition, the difference between the E_{1v}^{f} value for the *N =72* and *N = 96* supercells is only ~ 0.01 eV. Convergence with respect to supercell size can thus be said to have been fully achieved with *N = 72*. Thus, our calculated value for the monovacancy formation energy in h.c.p titanium is thus

1.98 eV. This value is not a good agreement with the experimental value reported by Shestopal [*187*] which is 1.55 eV, or the later positron annihilation measurement [*188*] which gives 1.27 eV. With regards to similar theoretical studies, we note that for *3d* metals such as Ti, V, and

Table 4.1. Monovacancy formation energy E_{1v}^{f} and formation volume Ω_{1v}^{f} for different supercell sizes. available experimental results are also shown for comparison. There is no reliable experimental result for monovacancy formation volume. The formation energy is in eV, while the formation volume is in the unit of atomic volume Ω_0

Supercell sizes, N	48	64	72	96	Published theory	Experiment
E_{1v}^{f}	1.920	1.920	1.980	1.970	2.13[a] 2.14[b] 2.03[c]	1.27[d] 1.55[e]
Ω_{1v}^{f} (Ω_0)	0.64	0.64	0.64	0.64	0.60[b]	

[a]Reference *190*.
[b]Reference *189*.
[c]Reference *191*.
[d]Reference *188*.
[e] Reference *187*.

Cr, both the LDA and the GGA calculations do overestimate E_{1v}^{f} [*170*]. We have also have compared our results with other *ab initio* data obtained using the full-potential linearised muffin-tin orbital (FP-LMTO) method [*189*], the full-potential Green's functions method [*190*] , and the GGA calculation of Trinkle et al. [*191*]. They reported 2.14, 2.13, and 2.03 eV, respectively. However, our calculated value of the formation energy in α-Titanium is consistent with the well known correlation stated for metals [*192*], that is, $E_{1v}^{f} = 10^{-3}\ T_m$, where T_m is the melting temperature (in K). With T_m = 1948 K for titanium [*193*], E_{1v}^{f} = ~1.95 eV. Carling et al. [*194*] have shown that surface energy corrections to the GGA E_{1v}^{f} value in aluminium reduces the discrepancy with experiments by increasing the theoretical value. Thus applying such corrections to our calculated monovacancy formation energy may not lead to better agreement with

experiment, suggesting that the calculations need to be further improved, especially approximations for the exchange-correlation potential for regions of diminishing electron density, such as in a vacancy. Nevertheless, a more extensive work by Mattsson et al. [*194*] on Pt, Pd, and Mo, shows that surface-correction to vacancy formation energies for both LDA and GGA generally lowers the discrepancy between theory and experimental values.

The formation volume Ω_{1v}^{f} calculated using Eqn. 4.2 is also shown in Table 4.1, and is found to be quite independent of the system size. Care should be taken when comparing theoretical results for the formation energy and the formation volumes with the experimentally determined values. This is because calculations pertain to an ordered array of vacancies at a higher density than the real life experimental situations. Nevertheless, for the formation volume, there is a good agreement with the value calculated in Reference 189. Furthermore, our result is consistent with available data in literature [178-180, 195] which shows that the theoretical relaxation volume values for metals are in the range of ~ 0.50-0.60Ω_0. There is no available experimental relaxation volume data for α-Titanium. With regards to structural relaxation around a monovacancy, Fig. 4.4 shows the amplitude u of the displacement of the neighbouring atoms as a function of the distance R (in the unit of lattice parameter, a_0) to the vacancy, obtained using the $N = 48$ supercell at fixed supercell size. The amplitude of the atomic relaxation is small, which is the usual observation in h.c.p titanium [*189,196*]. The first neighbour atoms are only inwardly relaxed by less than 2%, while the second nearest neighbour atoms are inwardly relaxed by just about 0.5 %. The third neighbouring atoms are however outwardly relaxed. Atoms at ~1.6a_0 are located at the boundary, and thus their displacement has to be zero due to symmetry restrictions. Furthermore, in h.c.p metals with a *c/a* ratio that is less than the ideal value of 1.633, such as in

titanium, the atoms below and above the basal plane (first neighbour atoms) are at slightly closer distances than those in the same plane (second neighbour atoms) [197] to the vacant site. The calculated displacement pattern of the atoms is therefore expected.

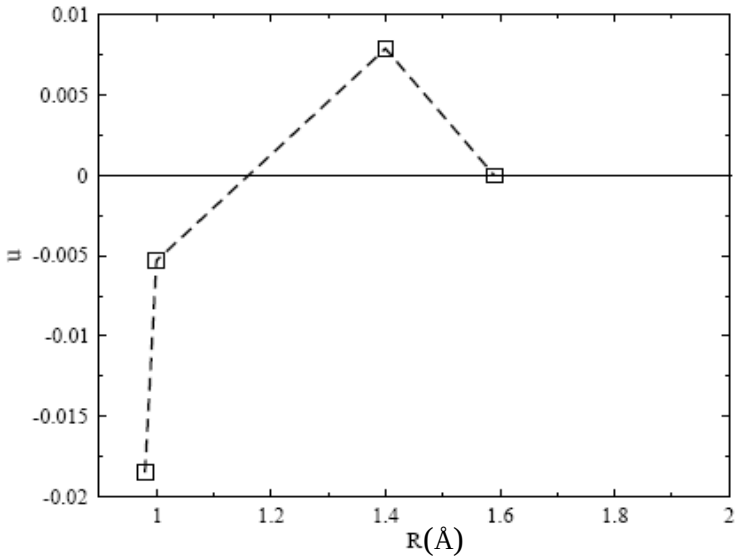

Fig. 4.4 Amplitudes of the atomic relaxations u as a function of the distance R (in the unit of lattice parameter a_0) around the vacancy. Figure corresponds to results obtained using the $N = 48$ atomic sites at fixed supercell size

Divacancy formation and binding energies for the three configurations in Fig 4.1 have been calculated using Eqns. 4.1 (with $n = 2$) and 4.3, respectively. The results are shown in Table 4.2, along with the formation volumes calculated using the Eqn 4.2. Cells containing 62 atomic sites have been used to study the D_{v1} and D_{v2} configurations, while D_{v3} has been studied with a supercell containing 72 lattice sites. The cells are all fully relaxed. From the table, we note that the binding energies for the D_{v1} and D_{v2} are both positive, i.e. E_{2v}^{B} = 0.10 eV and 0.12 eV respectively. This suggests that each of the two divacancy configurations is stable compared to

the two isolated single vacancies. In contrast, the D_{v3} divacancy configuration has a strong negative binding energy of -0.32 eV, implying strong repulsion between the vacancies, and is

Table 4.2 Divacancy formation energy E_{2v}^{f} and formation volume Ω_{2v}^{f}. D_{v1} and D_{v2} calculations have been done with N = 64 atomic sites. Asterisk (*) indicated that the D_{v3} was done with supercell containing 72 atomic sites.

Divacancy	E_{2v}^{f} (eV)	E_{2v}^{B} (eV)	Ω_{2v}^{f}
In-plane (D_{v1})	3.74	0.10	$1.385\Omega_0$
Out of plane (D_{v2})	3.72	0.12	$1.385\Omega_0$
Basal to basal (D_{v3})*	4.28	-0.44	$1.346\Omega_0$

thus likely to be a metastable configuration. The observation by Fernández et al. [*198*], that first and second neighbour divacancy are stable, and have practically the same binding energies, whereas the fourth neighbour divacancy, i.e. D_{v3}, is unstable, is consistent with our findings.

4.2.2 Electronic Properties of a Single Vacancy Defect

We now examine the effect of vacancy formation on the electronic properties of α-Titanium. First, there is a reduction of the electron density from the bulk value, from ~0.15/Å^3 to ~0.05/Å^3 at the vacancy centre. This decrease of the electron density is very similar to the behaviour at a surface, suggesting that vacancy may be regarded as an internal surface [*194*]. The excess charge in the empty space left by the vacancy may be due to charge redistribution such that charges from the nearest-neighbour are spread into the vacancy centre. Fig 4.5 (a) and (b) shows the plots of charge density difference with and without a vacancy, in a supercell containing a vacancy (N = *47*) and an ideal supercell (N = *48*). There appears to be a charge accumulation in between the

nearest-neighbour atoms. Also, the difference in electron density is more or less negligible for the regions beyond the nearest-neighbour atoms. The vacancy is thus efficiently screened similar to what has been previously observed in aluminium [*199*], h.c.p and b.c.c zirconium [*189*], and in f.c.c. transition metals [*162*]. The small perturbation of the charge density around the second-neighbour atoms is not totally unexpected in view of small atomic relaxation around the atoms as shown in Fig. 4.4.

We have investigated the distribution of electrons on the site of a vacancy and around its nearest-neighbours by calculating the density of states (DOS) of the supercell with N = *47* atoms (one vacancy), and then comparing with the bulk DOS. The DOS have been calculated using the tetrahedron method [*200*], and 10 × 10 × 8 *k*-points grid has been used for the Brillouin zone integrations.

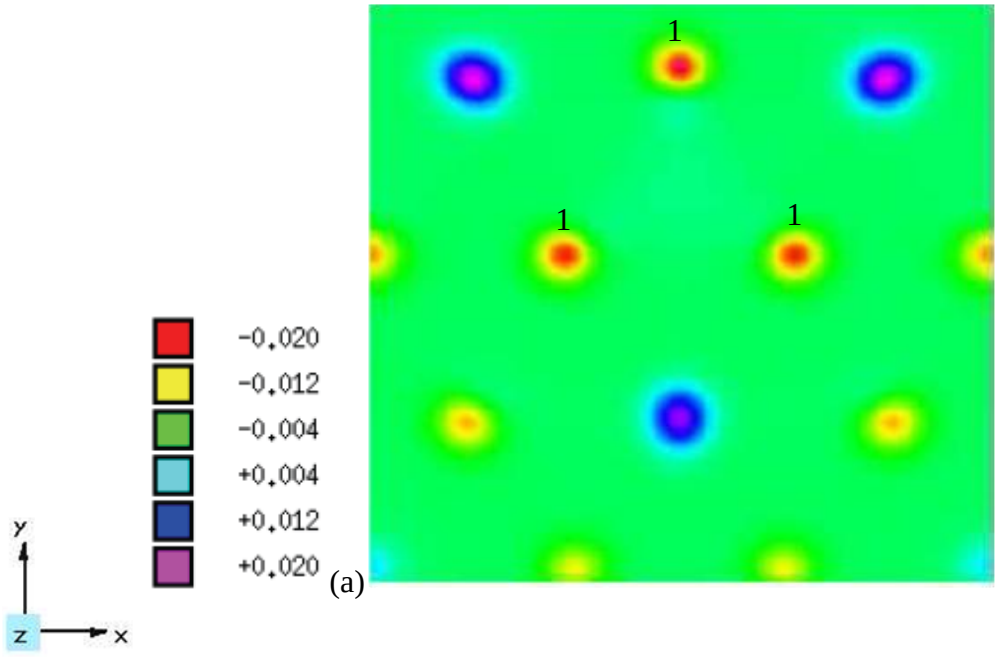

(a)

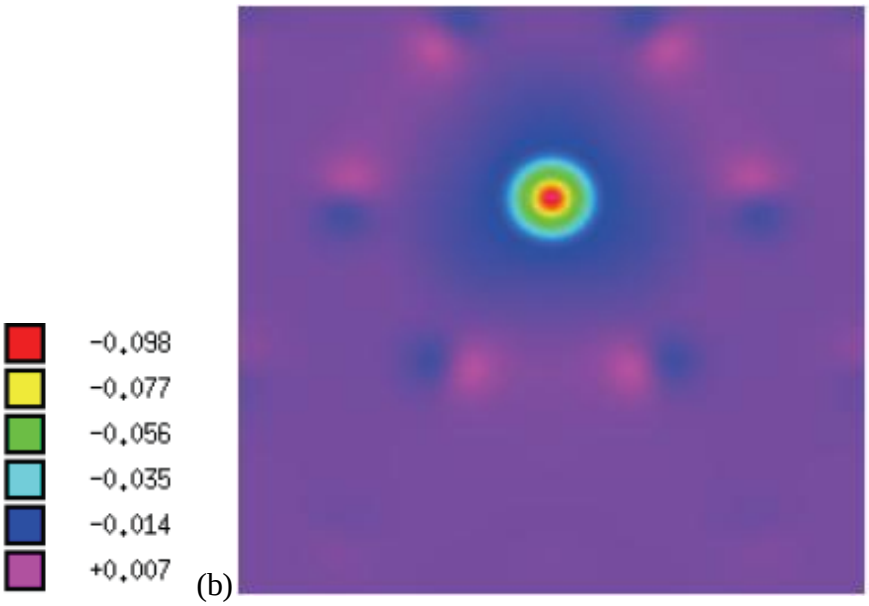

Fig. 4.5. (a) Charge density distribution around the nearest neighbour atoms (NNA) to a vacancy; label '1' indicates the positions of the NNA atoms (b) bottom panel: charge distribution around the second nearest neighbour to a vacancy. The size of the supercell is *N = 48*, and the plane of the figure is parallel to the basal plane. A positive sign on the legend indicates an excess of valence electrons, while a negative sign indicates depletion.

Fig 4.6 shows the DOS for a pure bulk titanium and titanium with a vacancy defect. The DOS consists in broad band around the Fermi level, characteristics of metals with an essentially *d* character. However, there are new features in the defect cell DOS: around the Fermi energy ($E = E_f$ = 0 eV), there appears some pronounced peaks which may correspond to states that are localized at the vacancy site and its nearest neighbours. In addition, there appears to be appearance of other resonance states in the vacancy supercell, such as, a low-lying state at about 1.25 eV below the E_f = 0 eV, and at ~1.70 eV and 2.40 eV above the $E_f = 0$, respectively. Simillar features have been observed in the combined experimental and theoretical studies of W (100) and Mo (100) surfaces by Weng et al. [*201*] and Posternak et al. [*202*]. Furthermore, we also observe the exact

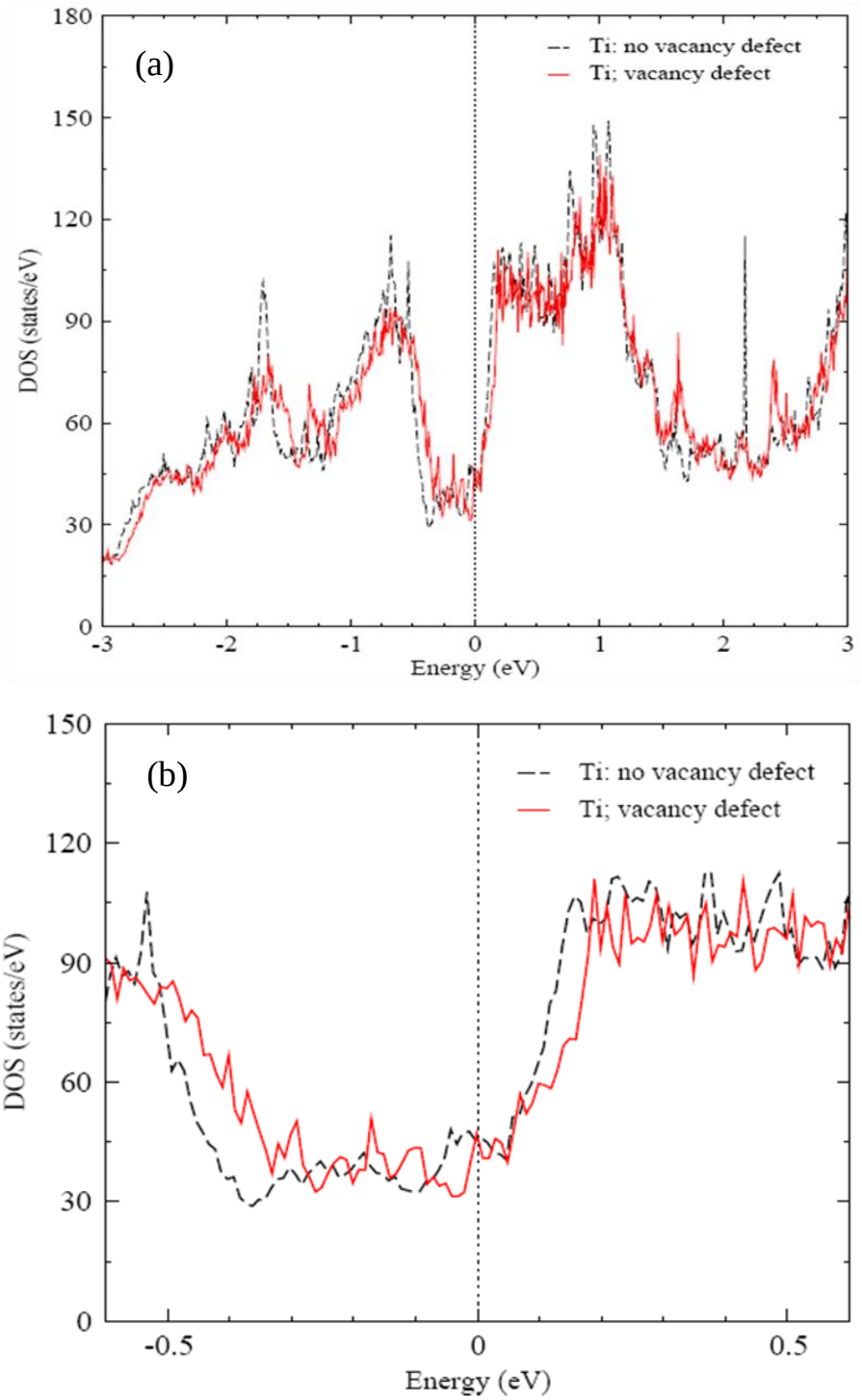

Fig 4.6 (a) Calculated total bulk density of states (dashed line) for a perfect supercell , *N = 48*, and for a supercell containg one vacancy, *N = 47* (full line) (b) Same plot, but with region around the Fermi energy (*E = 0*) enlarged. The tetrahedron method has been used to calculate the DOS.

coincidence of the Fermi energy with a peak as seen in the enlarged region around $E = 0$ in Fig. 4.6(b). This has a strong similarity with the observed strong surface resonance in the studies of Ti (0001) surface by Feibelman [*203*]. To explain the origin of this peak, we note that Friedel [*204*] associated the appearance of excess density of *d* states in resonance condition, which are introduced by an impurity to the existence of virtual bound states. By comparison, therefore, the peak presently observed, reflects the environment of the surface atoms, and may be associated to such resonance-like states. A similar explanation has been offered to explain the appearance of a strong central peak in tungsten with one vacancy [*195*]. Finally, it should be mentioned that despite the fact that we have shown the similarity between vacancies and surfaces, there is a fundamental deviation that is best explained in terms of two common density parameters: the reduced density gradient defined as $s = |\nabla n|/2(3\pi^2 n)^{1/3} n$, and the electronic Wigner-Seitz radius given by $r_s = (3/4\pi n)^{1/3}$ (*n* being the electron density) [*138*]. In closed-packed metals, such as titanium, when going from the bulk toward the centre of the vacancy, r_s increases monotonously whereas *s* first increases, reaches the maximum and then drops to zero around the vacancy centre [*205*]. Thus for vacancies, the maximum of r_s , that is, the minimum of the density corresponds to vanishing reduced density gradient [*206*]. On the other hand, for metallic surfaces, both r_s and *s* increases monotonously towards the vacuum.

4.2.3 Monovacancy and divacancy migration

Figure 4.7 (a) and (b) show the minimum energy paths for the *in-plane* and *out-of-plane* vacancy migration. Unlike the out-of-plane migration, vacancy migration in the basal plane (in-plane) does not follow a straight line connecting the initial and final positions. Both paths are shown in

Fig 4.8 (a) and (b) respectively. The migration energy barriers are E_{mi}^{v} = 0.47 eV and E_{mo}^{v} = 0.61eV for the *in-plane* and *out-of-plane* migration, respectively. Thus, there is anisotropy in the

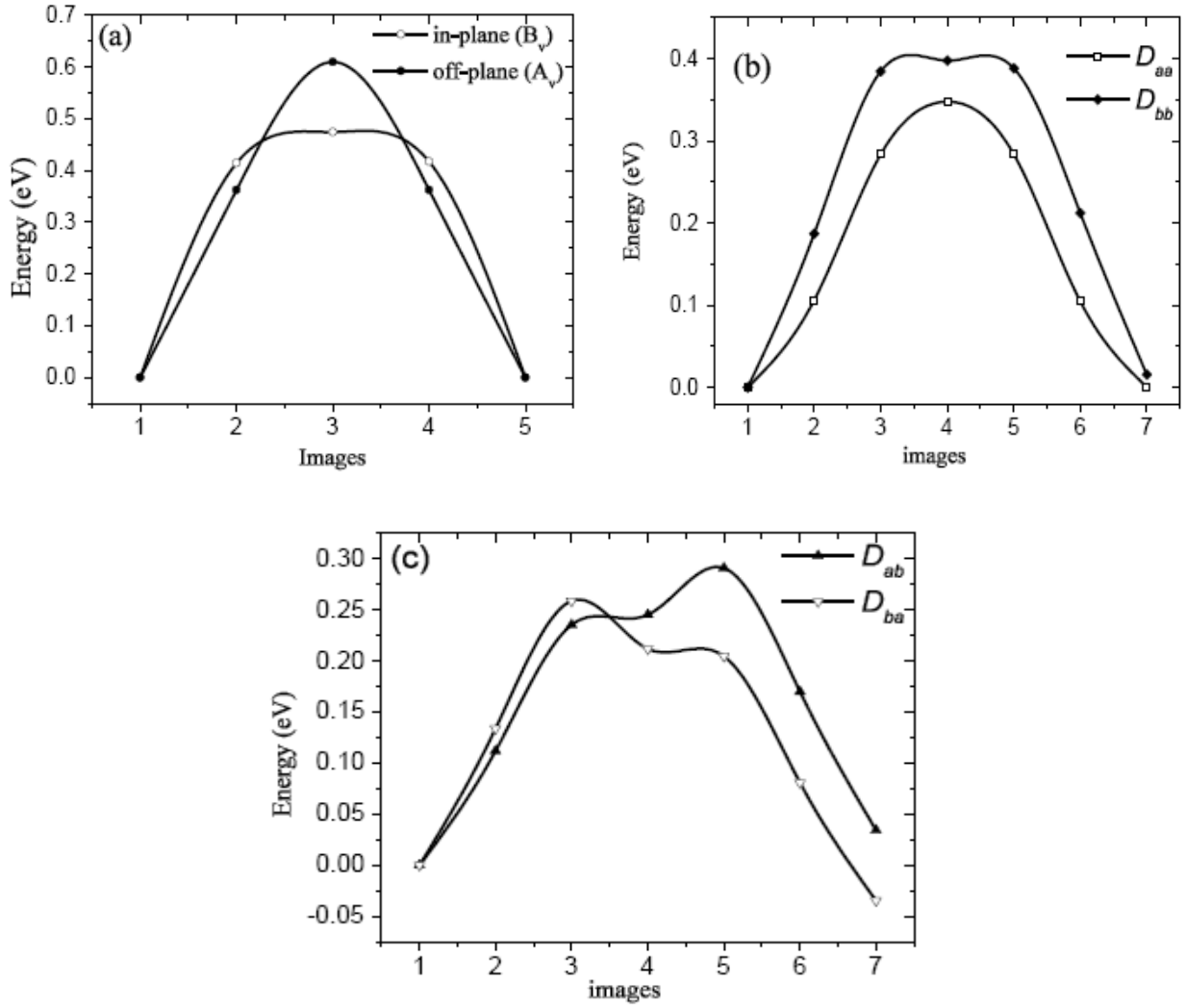

Fig. 4.7. Energy profiles for vacancy and divacancy migration. (a) Vacancy migration (b-c) divacancy migration.

single vacancy migration. The lower migration energy for the in-plane vacancy migration suggests that it is preferred, compared to the out-of-plane migration. This is consistent with the experimental results of Hood et al. [*207*], where it was suggested that vacancies might diffuse

faster in the basal plane than along the *c*-direction in h.c.p zirconium. Results from theoretical calculations of self-diffusion properties in h.c.p metals are very sensitive to the type of interatomic potential employed. Embedded atom method studies by Zope [*208*] slightly favoured *in-plane* basal migration in *α*-Titanium, whereas, Fernández [*209*] also using different EAM type interatomic potentials reported 0.51 (0.48) eV and 0.65 (0.65) eV respectively for the *in-plane* (*out-of-plane*) vacancy migration energy barrier in hcp titanium, thus slightly favouring out-of-plane migration. EAM many-body potential studies of Hu et al. [*210*] also predicted 0.61 (0.56) eV for the *in-plane* (*out-of-plane*) single vacancy migration. It should be noted however that, EAM potentials are usually fitted such that they reproduce equilibrium physical parameters of materials such as elastic constants, the lattice spacing or the *c/a* ratio, in the case of hcp metals. However, single

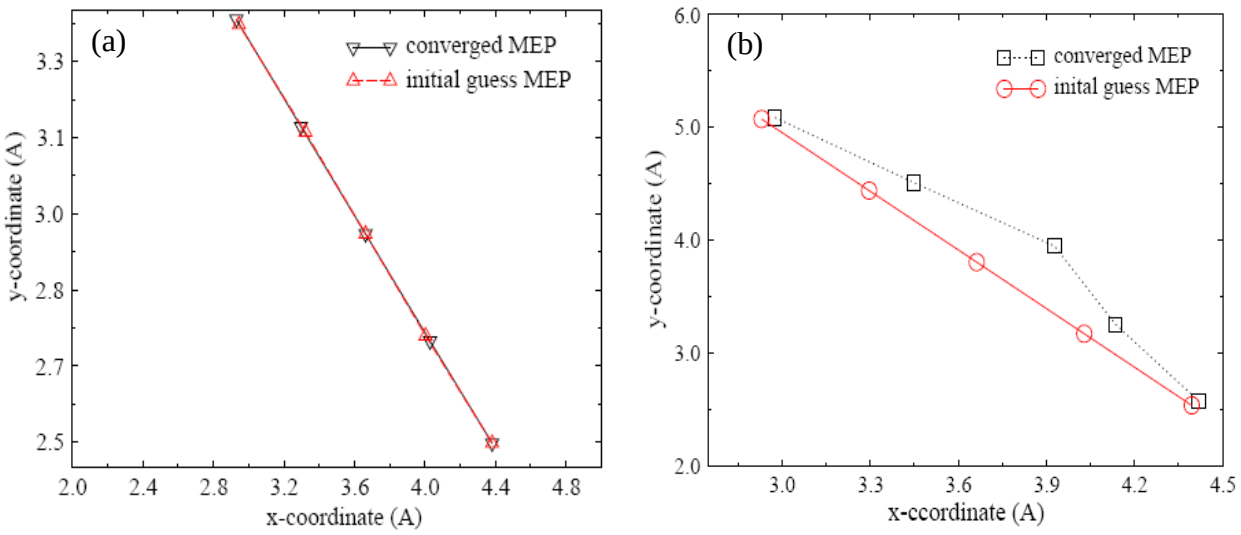

Fig. 4.8 Initial guess and converged minimum energy path for (a) off-plane vacancy migration (b) in-plane vacancy migration.

vacancy migration involves a self-atom that is much more close to other atoms than the equilibrium distance during the diffusion process. Therefore, EAM potentials offer simplified descriptions of the real situation occurring in diffusion processes, and migration properties predicted by such potentials may therefore be less accurate. *Ab initio* calculations are in principle

Table 2: Initial and final defect orientation in vacancy and divacancy migration. Also shown are the positions of interstitial (saddle) point locations. Migration barrier energies (in eV) are also shown. For each of the divacancy migration jump, the asterisk (*) indicates the coordinates of the migrating atom, while the other coordinate is for fixed vacancy. Double asterisk (**) are the estimates of the migration energy barriers for the divacancy diffusion, obtained by considering two saddle points for each of the path, as explained in the text.

defect	migrating jump	interstitial location	migration barrier (eV)
vacancy	B_v (0, 0, 0)→(a, 0, 0) A_v (0, 0, 0)→($a/2, -a/2\sqrt{3}, c/2$)	0.34a, 0.05a, 0 $a/2, -a/4\sqrt{3}, c/4$	0.47 0.61
Divacancy	D_{aa}: (0, 0, 0) → (a, 0, 0)* ($a/2,-a/2\sqrt{3}, c/2$)→($a/2,-a/2\sqrt{3}, c/2$)	0.5a, 0.67a, 0.01c	0.35
	D_{ab} : (0, 0, 0) →(0,0,0) ($a/2,-a/2\sqrt{3}, c/2$)→(0, 0, a)*		0.24**, 0.29**
	D_{bb} : (0, 0, 0)→(a, 0, 0)* ($a/2,-a\sqrt{3}/2$,0)→ ($a/2,-a\sqrt{3}/2$, 0)	0.69a, -0.01a, 0	0.40
	D_{ba}: (0, 0, 0) → (0, 0, 0) (0, 0, a) → (0,$-a/2\sqrt{3}$, c/2)*		0.22**, 0.25**

more accurate, since they are parameter free and they provide a better description of interactions between atoms at equilibrium and non-equilibrium lattice spacing. Using 1.92 eV as the vacancy formation energy, as obtained for *N = 48* supercell, the activation energy for self diffusion, i. e. $h_v^{sd} = E_m^v + E_f^v$, are h_{vi}^{sd} = 2.39 eV (*in-plane*) and h_{vo}^{sd} = 2.53 eV (*out-of-plane*) respectively.

Our calculated results for the activation energy are not in good agreement with those reported in the experiments. Libanti et al. [*211*] and Köppers et al. [*212*] both reported h_{vo}^{sd} = 1.27 eV and h_{vi}^{sd} = 3.14 eV respectively. As regards to previous theoretical studies, h_{vi}^{sd} = 2.31 eV [*213*], h_{vi}^{sd} = 2.77 eV [*182*], and h_{vo}^{sd} = 2.16 [*213*], h_{vi}^{sd} = 2.77 eV [*182*] have been reported. In Ref. *182*, an h.c.p lattice with an ideal *c/a* ratio is assumed, and the interatomic potential used in the calculations is fitted to lattice and elastic constants similar to those of titanium. Ref. *213* employed embedded atom potential fitted with parameters that are similar to that of Ref. *182*. In view of the aforementioned inherent limitation of fitted potentials, the discrepancy between these earlier studies and the present calculations is not totally unexpected.

Divacancy migration seems to be more complex. For the D_{aa} and D_{bb} migration, the saddle point is obvious and the migration energy barriers are E_{aa}^{d} = 0.35 eV and E_{bb}^{d} = 0.40 eV. In figure 4.7 (b), the migration paths are shown. The positions of the interstitials and the saddle point are also displayed in Table 4.3, along with that of a monovacancy. For the D_{ab} and D_{ba}, the saddle point is less obvious. We show the minimum energy path in Fig. 4.7(c). Image 4 for both divacancy migrations corresponds to the diffusing atom located at the centre of the triangle formed by three nearest neighbour vacancies. This atomic configuration has been described as the saddle point of the migration by Johnson [*182*]. Images 5 and 3 for the D_{ab} and D_{ba} respectively correspond to the migrating atom at the centre of an equilateral triangle formed by three nearest neighbour atoms. If image 4 is taken as the saddle point, the migration energy barrier energy for the D_{ab} and D_{ba} configurations are respectively E_{ab}^{d} = 0.24 eV and E_{ba}^{d} = 0.22 eV. However, if images 5 and 3 are taken as the saddle point, E_{ab}^{d} = 0.29 eV and E_{ba}^{d} = 0.25 eV. The choice of the appropriate saddle points is best resolved by carrying out vibrational analyses [*214*] of configurations

corresponding to the images. Nevertheless, with the present results, we may already conclude that divacancy migration is much faster than single vacancy migration, and the divacancy migration is such that the two vacancies move between two nearest planes in the *c* direction. *Ab initio* studies of vacancies and their migration in transition metals are rare, and where they exist, they are more focused on those of b.c.c structures [*215*]. The present study therefore is an important step towards a better description of vacancy diffusion mechanisms in a typical hexagonal close-packed metal.

4.2.4 Formation of self interstitial atoms

The interstitial formation energies for both constant volume and fully relaxed configurations are reported in Table 4.4. Only stable interstitial configurations, as well as the relaxation volumes for the fully relaxed configurations are shown. The effect of full relaxation is not very significant. As expected, the formation energies of fully relaxed configurations are less than that of constant volume calculations. However, the maximum energy difference between the configurations is only ~ 0.3 and 0.15 eV for $N = 37$ and $N = 65$, respectively. Also, relaxation does not affect the relative stability of the configurations in the two supercell sizes. In addition, in all the interstitial configurations, the relaxation volumes are only slightly greater than one atomic volume, in agreement with similar empirical studies in h.c.p metals [*213*], and specifically, in h.c.p zirconium [*165*]. Comparison between $N = 37$ and $N = 65$ atom supercell results for the fully relaxed supercell results for the fully relaxed configurations shows that the interstitial formation energies do not change significantly between these two supercell sizes for all the studied configurations, except BS. The differences are 0.03 eV for *S* and *C* configurations, and less than 0.1 eV for the *O* configuration. In the case of the *BS* configuration, it was observed that the

difference in the calculated formation energy between the two supercell sizes is 0.23 eV. Hence, we have used a supercell of size $N = 96$ to ascertain the convergence of the formation energy to 2.45 eV. With the exception of the BS configuration, therefore, the formation energies for all the interstitial configurations can be said to have converged for a supercell of 64 atoms. The *O* and *BO* configurations have the lowest formation energies consistent with results obtained in GGA calculations in similar hcp Zr [*165*], while the *C* configuration has the largest formation energy. The overall spread in energies is not large, ranging between 2.13 and 2.53 eV for the fully relaxed 64-atom supercell. In addition, compared to similar studies on body-centered cubic (b.c.c)

Table 4.4. Formation energies and relaxation volumes for various interstitial configurations in hcp titanium. The asterisk (*) in the table indicates that a supercell of size $\boldsymbol{N}$ = 97 was required to reach acceptable convergence for the BS interstitial configuration. The *T* configuration decay to *S*, while *BT* and *BC* decay to the *BO* configuration.

Configurations	*O*	*C*	*S*	*BO*	*BS*
*Formation energy (*eV*)*					
$\boldsymbol{N}$ **= 37**	2.22	2.50	2.51	2.32	2.62
Relaxed	2.26	2.50	2.76	2.36	2.92
Unrelaxed					
$\boldsymbol{N}$ **= 65**	2.13	2.53	2.48	2.25	2.39 (2.45*)
Relaxed	2.28	2.68	2.62	2.39	2.57
Unrelaxed					
Relaxation volume (Ω)					
$\boldsymbol{N}$ **= 37**	1.17	1.30	1.22	1.15	1.19
$\boldsymbol{N}$ **= 65**	1.35	1.26	1.30	1.13	1.25

transition metals (TM) [*216*], the interstitial formation energies are low. However, a close look at those calculated for transition metal groups 5B and 6B in Ref. 63 shows a substantial decrease in

formation energy across the period, and an increase, down the group. For example, from Cr to V, Mo to Nb, and W to Ta, the formation energies are substantially reduced for all the interstitial configurations reported. A similar trend is observed for W → Mo → Cr and Ta → Nb →V. If the energy values reported in [*31*] for octahedral (2.84 eV), crowdion (3.08 eV) and dumbbell (3.01 eV) interstitial configurations in zirconium are taken into consideration, there is indeed a substantial decrease in formation energy from Nb to Zr. We may, therefore, expect a similar pattern of results, from V to Ti, or even from Zr to Ti. Based on the calculated formation energies, two configurations (*O* and *BO*) are probably the most stable configurations in hexagonal phase titanium. The energy differences between them are quite small, i.e. 0.12 eV. The small energy differences are also suggestive of possible co-existence of these configurations. Configurations *S*, *C* and *BS* appear to be less stable. Making a firm prediction of interstitial stability is generally tricky, especially when relatively small supercell sizes, as used in this work, are considered, since interstitials induce long-range stress fields. To make more quantitative predictions, therefore, larger supercell may be needed to study the effect of the elastic interaction of an interstitial with its periodically repeated images. Nevertheless, a comparison of our results with similar ab initio studies conducted using larger supercell sizes, in hexagonal closed packed Zr, shows good agreement in term of the relative stability of the interstitial configurations. Willaime [*31*] concluded that, in hcp Zr, the most stable interstitial configurations are likely to be *O*, *S*, *BC* and *BO*, while the *C* configuration appears to be less stable, in good agreement with our observation for h.c.p titanium. Domain et al. [*165*] observed that five configurations, i.e. *O*, *BO*, *BC*, *S* and *C*, are more stable than the *BT* configuration in h.c.p Zr. The energy differences between these five configurations are, however, small, suggesting their possible co-existence under irradiation. In addition, their relative concentration may also depend on differences in

vibrational entropy [*209*] or in electronic formation entropy [*217*], resulting from temperature change. The symmetry of the hcp lattice is such that the defects and the surrounding atoms can undergo large relaxation from the initial configuration. The three atoms forming the equilateral triangle around the *BO* are pushed equally outward by about 0.6 Å. The two interstitial atoms forming the *BS* configuration also appear to be pushed apart, and are slightly displaced from the line passing through their sites. The atoms forming the cage around the *O* interstitial are equally displaced outward: the strain field is symmetric. The *O* atom itself indeed appears to have maintained its initial input symmetry. Furthermore, both *BT* and *BC* configurations decay to *BO*, and the *T* configuration decays to *S*.

Extensive reviews of theoretical models of intrinsic point defects in hexagonal closed packed metals can be found in the article by Bacon [*218*]. In this review, it was observed that all pair potentials that model an equilibrium hcp crystal result in *c/a* value equal, or very close to the ideal value of 1.633. All the defect properties modelled by these potentials are, therefore, not fully reliable, but rather serve as a possible guide to what may actually occur. Many-body potentials have been developed rapidly in the last decade, though their applications in defect studies of hcp metals are not as extensive as for the cubic systems. These potentials normally contain many-body terms, which depend on the distance between the atoms, and many-body terms, which depend on the local atomic density when an atom is embedded in the medium created by its neighbours. In addition, the potentials are usually fitted to several physical parameters, such as the *c/a* ratio and the elastic constants of the materials, but not to any data arising from interatomic interactions at distances less than the normal equilibrium lattice spacing, such as those encountered for interstitials. This leads to formation energies which are too large.

In addition, the many-body terms are isotropic and neglect directionality in the bonding, which may be important for transition metals. Therefore, these potentials offer only a simplified description of the real situation [*219*]. Ackland [*196*], using such potentials in titanium, has predicted that only SIAs within the basal plane, that is *BS*, *BC* and *BO*, are stable. Fernandez et al. [*209*], using embedded atom potentials, also predicted *BS* and *BC* to be the most stable. Mikhin et al. [*220*] suggest *BO* as the most stable configuration, while Bacon [*218*] concluded that both basal and non-basal SIAs are likely to be stable in metals with *c/a* =1.633. In most hcp metals studied by Igarashi et al. [*221*], using many-body potentials, the energetically most favourable interstitial configuration is the crowdion associated with the site *C*. However, the interstitial at the octahedral site *O* possesses, in these cases, only a marginally higher energy. Therefore, both *O* and *C* may likely co-exist as common interstitial configuration. Oh and Jonson [*222*], employing EAM potentials for Mg, Ti and Zr, showed the site *C* to be energetically most favourable and the site *O* having a slightly higher energy. They also showed that sites *S*, *T*, *BO* and *BC* show higher energies or are unstable. Pasianot et al. [*223*] also predicted *BC* and *BO* to be the most stable configurations for Zr and Ti. Willaime et al. [*224*], using many body interatomic potentials for their calculations, predicted that, in h.c.p Zr, both *S* and *T* configurations are unstable, and that both decay to *C*. In addition, their calculations also suggest that *BC* and *BT* are also unstable and decay to *BO*, in agreement with our results. From the experimental side, Huang's X-ray diffuse scattering measurement on electron irradiated single crystal hcp zirconium, at liquid helium temperature, suggests *O*, *S* and *T* as the most stable configurations [*165*]. Also, internal friction measurements [*225,226*] on neutron-irradiated Ti and Zr polycrystalline wires at 77K show peaks that have been attributed to the *C* configuration [*223*]. This study concludes, from an *ab initio* energetics point of view, that the *O* and *BO*

interstitial configurations are more likely stable interstitial configurations in hexagonal closed packed titanium. The small energy differences between these configurations make their possible co-existence an equally likely possibility. In addition, we conclude that the *T*, *BC* and *BT* are metastable: *T* decays to *S*, while both *BC* and *BT* decay to the *BO* configuration.

4.2.5 Migration of self interstitial atoms

The minimum energy path (MEP), calculated using the nudged elastic method, for the migration of a self-interstitial titanium atom from an octahedral position to the nearest octahedral position, along the *c* direction, is shown in Fig. 4.8 [*145*]. Once the NEB has shown that the MEP is such that the self-interstitial atom, starting at the *O* site, passes through the *BO* configuration at halfway, we used three intermediate images between these two configurations to locate the saddle point and to determine the migration energy barrier. The other half of the MEP path, that is, from *BO* to *O* (i.e. image 6–9), has been obtained by symmetry considerations. The *BO* configuration appears to be a local minimum. The local structures of the initial state (image 1), the transition state (image 2) and the local minimum (image 5) are also shown. The local minimum is about 0.11 eV higher in energy than the initial state (image 1). The three nearest neighbour atoms forming an equilateral triangle around the interstitial atom in image 5 are radially equally displaced. Images 6, 7, 8 and 9 are mirrors of images 4, 3, 2, 1, respectively. In addition, one can also see that the mirrors of images 4, 3, 2, 1, respectively. In addition, one can also see that the self-interstitial atom moves from *O* to the *BO* position via a configuration that lies in between them. This configuration corresponds to image 2 in Figure 4, and it appears to represent the first saddle point for the interstitial atom migration. As earlier explained, the second saddle point corresponding to image 2 should be image 8. The NEB calculated migration energy

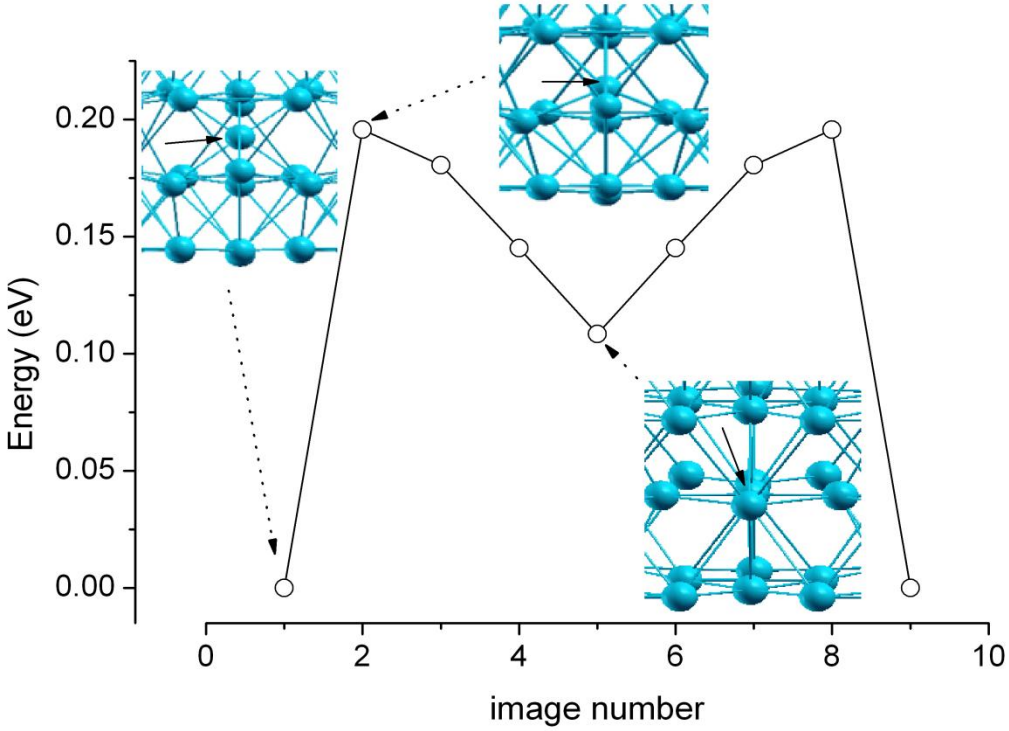

Figure 4.8 Minimum-energy path (MEP) for self-interstititial *O–BO–B* migration in a 64 atom titanium supercell. Shown on top of the MEP are the relaxed local structures of initial, transition, and intermediate states. The structure of the final state coincides with the initial one and is therefore not shown. Thick black arrows on the structures point to the positions of self-interstitial atoms

barrier for diffusion is low, i.e. approximately 0.20 eV. Finally, it should be emphasized that a better description of titanium self-interstitial atom migration may be obtained by increasing the number of images used in the NEB calculations. However, increasing the number of images is not likely to significantly change the quantitative result on the migration energy barrier, within the accuracy of calculations.

CHAPTER 5

Krypton and vacancies interactions in α-Titanium

Impurity-defect energetics are of great importance, since they can be incorporated in multiscale models [*227*] that can be used to make quantitative predictions of the macroscopic properties of solids containing the impurity atoms. Thus, in this chapter, krypton impurity sites in α-Titanium, possible migration paths, and the stability of small interstitial krypton–vacancy complexes, Kr_mV_n, for n, m = 0 to 4 are investigated. Multiple defect interactions in clusters containing several combinations of vacancy and substitutional krypton atoms have been studied, and possible diffusion mechanisms for krypton incorporated into titanium are proposed.

5.1 Computational Methodology

The pseudopotential (PP) for titanium has been described in Section 3.1 of Chapter 3. The krypton PP is also a Vanderbilt USPP [*93*] which was developed by one of the principal scientist of the Abdus Salam ICTP, since it was not available in the Quantum-Espresso [*127*] online library of pseudopotentials [*228*]. The atomic configuration for the PP construction consists of eight electrons in the valence: $4s^2\ 4p^6$. The cut-off radii for the *s* and *p* orbital components were taken to be r_{cs} =1.7 and r_{cp} =1.7 (in atomic units (a.u)), respectively. The inner cut-off radii of the *L*-components (L = 0, 1...4) for the conservation augmentation charges are r_{in}^{L} = 1.0 a.u (Eqn. 2.72 of Chap. 2). To study krypton in titanium using the planewave pseudopotential method, both elements must have the same exchange and correlation functional. Thus, for the krypton PP, exchange and correlation interactions were described by the Perdew and co-workers (PW91) [*72*] in the framework of GGA, adding non-linear

core correction [*94*] to the charge density. With the above mentioned parameters for the krypton PP, a good energy convergence of ~ 0.01 eV was achieved using an energy cut-off of ~ 300 eV for the pseudo-wavefunctions, and 3400 eV for the augmentation functions $\varrho_{\alpha\beta}(\boldsymbol{r})$ (Eqn. 2.66b).

The relative stabilities of the various krypton insertion sites in titanium are determined by calculating the formation energies of substitutional and interstititial sites, using the supercell models of the defect structures in which the krypton atoms are placed at the appropriate positions within the cell. Comparing the formation energies gives an indication of the occurrence of a particular defect configuration in preference to others in similar thermodynamic conditions [*229-231*]. For a supercell consisting of *N* titanium atoms and one krypton atom with energy $E(N\mathrm{Ti},\mathrm{Kr})$, the formation energy is calculated as [*232*]

$$E_{\mathrm{int}}^{f} = E(N\mathrm{Ti},\mathrm{Kr}) - NE(Ti) - E(\mathrm{Kr}) \tag{5.1}$$

if the krypton atom is in the interstitial position, and [*41*]

$$E_{subs}^{f} = E((N-1)\mathrm{Ti},\mathrm{Kr}) - ((N-1)/N)E(N\mathrm{Ti}) - E(\mathrm{Kr}) \tag{5.2}$$

if the krypton atom is substitutional. $E((N-1)\mathrm{Ti},\mathrm{Kr})$ represents the energy of a supercell containing *N*-1 titanium atoms with a single krypton in a substitutional site; $E(N\mathrm{Ti})$ is the energy of a supercell containing *N* titanium atoms, while $E(\mathrm{Kr})$ represents the energy of a single isolated krypton atom in an empty supercell. The first two terms in the Eqns. 5.1-5.2 are usually calculated using the same set of *k*-point grids, energy cut-off, and other computational settings so as to minimize the effect of systematic errors [*233*]. The third term i.e. $E(\mathrm{Kr})$ is calculated by inserting a single krypton atom in a box of sufficiently large size and carrying out a Γ-point calculation.

The simplest krypton defects involve substitutional and interstitial positions. There are two possible interstitial positions shown in Fig. 5.1: the octahedral and the tetrahedral. However, in the h.c.p structure, all substitutional positions are equivalent. Thus, it is sufficient to consider a single krypton atom occupying a vacant titanium site as the substitutional configuration. The relative stability of the krypton insertion sites are determined by calculating the formation energy of the corresponding configurations, using supercell models and Eqn. 5.1 in the case of interstitial atoms, and Eqn. 5.2 for the substitutional atom. The atomic coordinates and volume were relaxed to minimize the forces and pressure. The energy of the krypton atom is obtained by considering a cubic unit cell with a significantly large lattice parameter of 10 Å, and Γ-point in the irreducible Brillouin zone. To examine the impact of the supercell sell size on the relative stabilities of the three defect configurations, we carried out simulations involving two supercell sizes, namely, 64 and 120. The dimensions of these cells are $4a \times 2a\sqrt{3} \times 2c$ and $4a \times 5a\sqrt{3/2} \times 3c$, respectively. Brillouin-zone sampling was performed using the Monkhorst-Pack scheme [*97*]. For the 120-atom supercell, 2 × 2 × 2 *k*-point mesh was used. We could not use denser *k*-point grid due to the substantial increase in the computational time. Nevertheless, it is envisage that this mesh size should be sufficient to converge the total energy within the acceptable value, given that for the conventional primitive unit cell size, the energy converged to within 2 meV/atom for the 8 × 8 × 8 *k*-point mesh. Equivalent *k*-point densities to that of the conventional unit cell were chosen for the 64-atom supercell structure. The energy cut-off used for all the supercell calculations was 476 eV.

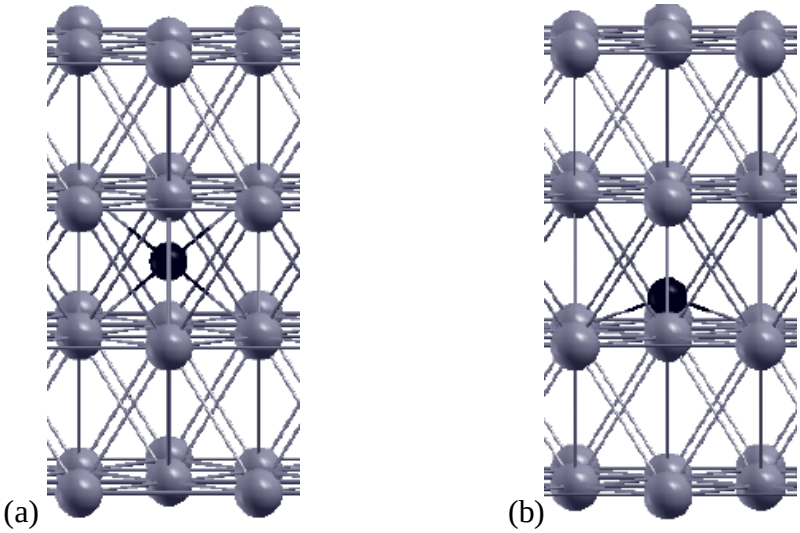

(a) (b)

Fig 5.1 (a) octahedral and (b) tetrahedral interstititial positions in h.c.p structure. The grey spheres represent the positions of titanium lattice sites, while the black sphere shows the position of the interstitial. A substitutional site is a foreign atom occupying a regular lattice site in the host structure, and is therefore not shown in the figure.

The electronic structure of the Ti-Kr system can be investigated using the concepts of density of states (DOS), as well as the electronic density redistribution due to the incorporation of the krypton impurity atom. The DOS has been described in section 3.1. However, the total density of states can be projected onto a local set of states or atomic sites in what is known as the projected density of states (PDOS). The PDOS thus corresponds to a decomposition of the Kohn-Sham (K-S) states in term of local atomic orbitals. The K-S wavefunctions $\left|\varphi_{n,k}\right\rangle$ are projected on a set of orthogonalized atomic wavefunctions $\left|ilm\right\rangle$, where *n* is the band index, *k* is the electron wavevector, *i* indicates the corresponding atomic sites, and *lm* are the usual angular momentum quantum numbers. Then, the local contribution to the total density of states from site *i* is [*234*]

$$\rho_{ilm}(E) = \sum_{n,\vec{k}}^{occ} \delta(\varepsilon_{n,\vec{k}} - E)\left|\left\langle ilm \middle| \varphi_{n,\vec{k}} \right\rangle\right|^2 \tag{5.3}$$

where the factor $\left|\left\langle ilm\left|\varphi_{n,\vec{k}}\right\rangle\right|^2$ may be interpreted as the probability of finding an electron in the eigenstates $\varphi_{n,\vec{k}}$ at site *i*. The total charge associated with the local site is [*235,236*]

$$\rho_i = 2\int_{-\infty}^{E_F} \rho_{ilm}(E)dE \tag{5.4}$$

where E_F is the energy of the highest occupied state and the factor of 2 is for spin degeneracy.

For a supercell containing *N* titanium atoms and a krypton atom, that is, NTi-Kr, the electronic density redistribution map due to the presence of a krypton atom is obtained by subtracting from the electronic density of a system *N*Ti-Kr, both the electronic density of NKr and the electronic density contribution of an isolated Kr atom. Thus [*237*]

$$\Delta n = n(\mathrm{Ti}+\mathrm{Kr}) - n(\mathrm{Ti}) - n(\mathrm{Kr}) \tag{5.5}$$

where n(Ti+Kr*)*, n(Ti), and n(Kr) are the charge density contributions from supercells containing one krypton atom and *N* titanium atoms, krypton-fee supercell and isolated krypton atom, respectively. With this representation, the isosurfaces of the charge difference map gives a direct real-space visualization of the local electronic deformation due to the presence of the krypton atom. The formation energy of a $\mathrm{Kr}_M\mathrm{V}_L$ cluster containing *M* krypton atoms and *L* vacancies is defined as [*238*]

$$E_f(\mathrm{Kr}_m V_m) = E(\mathrm{Kr}_m \mathrm{V}_n) - mE(\mathrm{Kr}) - (N-n)E(\mathrm{Ti}) \tag{5.6}$$

where the $E(\mathrm{Kr}_m\mathrm{V}_n)$ is the calculated total energy of a supercell containing *m* krypton atoms and *n* vacancies; *N* is the number of titanium atoms; E(Ti) is the energy per titanium atom in a perfect lattice; and E(Kr) is the energy of isolated krypton atom. The stability or binding of a krypton-

vacancy cluster, Kr_mV_n, can be described by the binding energy of a vacancy E_b(V), or a krypton E_b(Kr) atom to the cluster. In the case of the vacancy, the binding energy is calculated as [*239*]

$$E_b(\mathrm{V}) = E_f(\mathrm{Kr}_m\mathrm{V}_n) - E_f(\mathrm{V}) - E_f(Kr_m\mathrm{V}_{n-1}) \tag{5.7a}$$

and

$$E_b(\mathrm{Kr}) = E_f(\mathrm{Kr}_m\mathrm{V}_n) - E_f(\mathrm{Kr}) - E_f(Kr_{m-1}\mathrm{V}_n) \tag{5.7b}$$

in the case of krypton atom. With such a scheme, a negative binding energy means attraction between the entities, while a positive binding energy implies repulsion. Also, the more negative the binding energy, the greater the stability. These definitions will be used to explore different combinations of vacancies and krypton atoms in cluster configurations. The interaction energy between a vacancy and krypton clusters in a supercell containing *N* titanium atoms in substitutional sites and *n* vacancies can be defined as [*227*]

$$\delta E_{\mathrm{int}}(\mathrm{V}_n, \mathrm{Kr}_p) = E_f(\mathrm{V}_n, \mathrm{Kr}_p) + E(N\mathrm{Ti}) - E(\mathrm{V}_n) - E(\mathrm{Kr}_p) \tag{5.8}$$

Here, the first term on the right is the total energy of an atomic system consisting of *n* vacant sites (denoted by V_n) and *p* near-neighbour sites of the vacancies occupied by krypton atoms, all remaining sites being occupied by titanium atoms. The second term, E(*N* Ti), is the energy of a perfect h.c.p lattice containing *N* lattice sites, while $E(\mathrm{V_n})$ is the energy of a titanium lattice containing *n* vacancies. The last term, $E(\mathrm{Kr}_p)$, is the energy of the supercell containing *p* krypton atoms in substitutional sites. As for the binding energy, negative interaction energy indicates an attraction, while a positive energy indicates repulsion, between the krypton atoms making up the configuration.

It is well known that DFT is not capable of describing physical properties of van der Waals (vdW) atoms, such as krypton, due to its incorrect treatment of forces binding the solid phase of such atoms. Nevertheless, our use of DFT-GGA is justified, since we are considering krypton atoms inside a metal where the electronic densities are much higher than in solid krypton, and the resulting interactions are much stronger. Moreover, interatomic distances in metals are small, and vdW forces should play little role in krypton-titanium atom interactions. It should be mentioned, however, that different schemes that describe vdW interactions in the framework of standard density functional theory now exists [*240*]. Finally, the following definitions have been used concerning relaxations. The relaxation energy of a crystal is determined as a difference between the total energy of a crystal before and after relaxation. The relaxation volume is determined in a similar way.

5.2 Results and Discussion

5.2.1 Single krypton impurity occupancy in α-Titanium

In Table 5.1, the formation energies of interstitial and substitutional sites are presented. They have been calculated using Eqns. 5.1 and 5.2 respectively for both relaxed and unrelaxed supercells consisting of 120 atoms. First we note that ordering of the formation energies is $E^f_{subs} < E^f_{octa} < E^f_{tetra}$, suggesting that the octahedral interstitial configuration is energetically more favourable than the tetrahedral. The energy difference between the interstitial configurations is 0.46 eV for relaxation at constant volume, decreasing slightly to 0.45 eV after volume relaxation. More importantly, relaxation does not change the ordering of the stability of the defect configurations. Changing the supercell size from 64 to 120 atoms cell also preserves this ordering. The relative stability of the octahedral site to that of the interstitial may be understood from the following simple arguments [*241*]: using the

calculated lattice parameters of h.c.p titanium, the 'radii' of the tetrahedral and the octahedral sites are 1.78 Å and 2.05 Å respectively, and the covalent radius of krypton atom is 1.1 Å [*242*]. Therefore, the free volume available for the octahedral defect is larger than that of the tetrahedral. Krypton has a closed shell electronic structure and bonding interactions are not expected, it is thus reasonable to expect krypton atom to occupy larger octahedral sites.

Table 5.1. Formation energies E_j^f (j = subs, octa, tetra) and relaxation energy E_{rel} (in eV) of substitutional and interstitial defect in h.c.p titanium. Relaxation volume $\Delta\Omega$ (in Ω_0) is also given.

property	unrelaxed	relaxed
E_{subs}^f	5.78	5.73
E_{octa}^f	6.96	6.79
E_{tetra}^f	7.42	7.24
$\Delta(E_{tetra}^f - E_{octa}^f)$	0.46	0.45
$\Delta\Omega$		1.82 (octa) 1.86 (tetra) 0.84 (subs)
E_{rel}		0.01 (octa) 0.02 (tetra) ~0.00 (subs)

As may be expected, placement of krypton into the vacancy causes lattice expansion relative to the pure solid. However, the volume expansion associated with interstitial krypton is more than double that of the substitutional krypton, although the relaxation volume for the two interstitial only differs only slightly. The volume resulting from the krypton substitution is higher than the vacancy formation, i.e. ~ $0.80\Omega_0$ compared to ~$0.60\ \Omega_0$. The relaxation energy appears to be insignificant for the three configurations. Nevertheless, the value for the tetrahedral configuration is higher than that of the tetrahedral. The relaxation of the surrounding titanium lattice due to the presence of the krypton

impurity atom is remarkably different in the three defect configurations. For the relaxed octahedral configuration, shown in Fig 5.2(a), the relaxed krypton atom almost maintains its initial input configuration. However, the first neighbour toms are equally displaced by about 0.40 Å: *the strain field is symmetric*. As for the tetrahedral configuration (Fig 5.2(b)), the greatest displacement of the krypton atom is along the *c*-axis. However, in this case, the relaxed position of the krypton atom is such that it is exactly mid-point between the three atoms at the

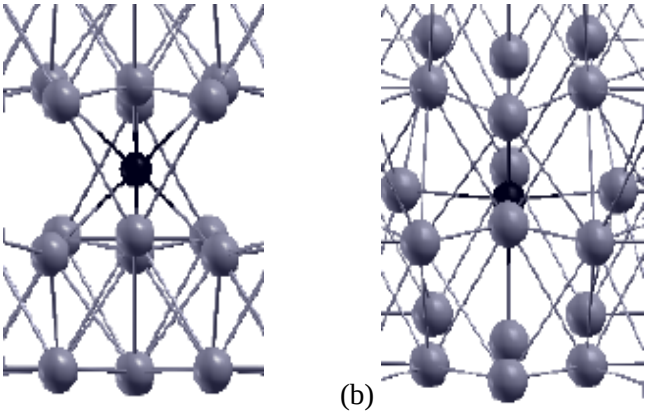

(a) (b)

Fig 5.2 Local lattice relaxations around krypton atom in (a) octahedral (b) tetrahedral, positions. Grey spheres are titanium atoms, while black spheres represent krypton impurity atom.

base of the tetrahedron, thereby pushing the atoms outwardly by ~ 0.64 Å from their initial input configuration. In addition, the displacements of the second nearest neighbour titanium atoms to the krypton atoms are greater for the tetrahedral, than for the octahedral configuration. Relaxation of the neighbouring atoms and the substitutional krypton is quite negligible, as the first neighbour atoms are pushed outwardly by only ~ 0.1 Å, and the relaxed krypton atom almost maintain its substitutional position. The krypton atom is displaced only by ~ 0.03 Å (~1% of the lattice parameter) along the *a*-axis, towards another atom in the same plane, and is displaced by the same amount along the *c*-axis. If the relaxation of the surrounding lattice around the krypton atom is an indication of the relative

stability of the three configurations, then we find the same order of site preference for the krypton defect. We may summarize the relative stability of krypton atom in titanium as follows: for the krypton in interstitial sites, the octahedral position is energetically more favourable than the tetrahedral. However, for the three defect configurations, the substitutional site is the most energetically preferred.

5.2.2 Electronic properties of interstitial krypton atom

Krypton induced electronic rearrangement may not be directly related to observable metallurgical properties of the host titanium matrix. Nevertheless, analyzing the electronic structure of the krypton defects will shed light on what underlies the krypton site preference in titanium. In addition, it gives a realistic picture of a closed-shell noble gas atom inside a typical *3d* h.c.p. transition metal. The latter is particularly important in view of the fact that earlier studies on krypton atom insertion into h.c.p titanium focused either on experimental studies of damage profile [*243*], or the changes in the pre-existing stress profile resulting from the implantation [*12*]. None of these earlier studies focused on underlying electronic structures in order to have a more complete picture of the krypton atom in titanium, as has been recently done for xenon nanoparticles in aluminium [*48*] using the electron energy loss spectroscopy studies [*45*]. In addition, recent studies on noble gas atoms in metals focus mainly on helium in cubic metals [*32,42,45*], and krypton and xenon in aluminium [*244,48*].

The electronic density of states (DOS) corresponding to the krypton insertion sites were evaluated for the octahedral and the tetrahedral occupancies. Fig. 5.3 shows the DOS corresponding to krypton in the octahedral site which is similar to that of the tetrahedral site. The DOS for the substitutional and the tetrahedral sites are similar. The result was obtained for a 64-atom supercell with $8 \times 8 \times 8$ *k*-grid for the Brillouin zone integrations, using the tetrahedron method [*100*]. Characteristically of metals

with an essentially *d* character, the total DOS consists of a broad band around the Fermi level. In addition, a strong peak that can unambiguously be attributed to krypton atom can be seen at about -10.1 eV below the Fermi level. From the

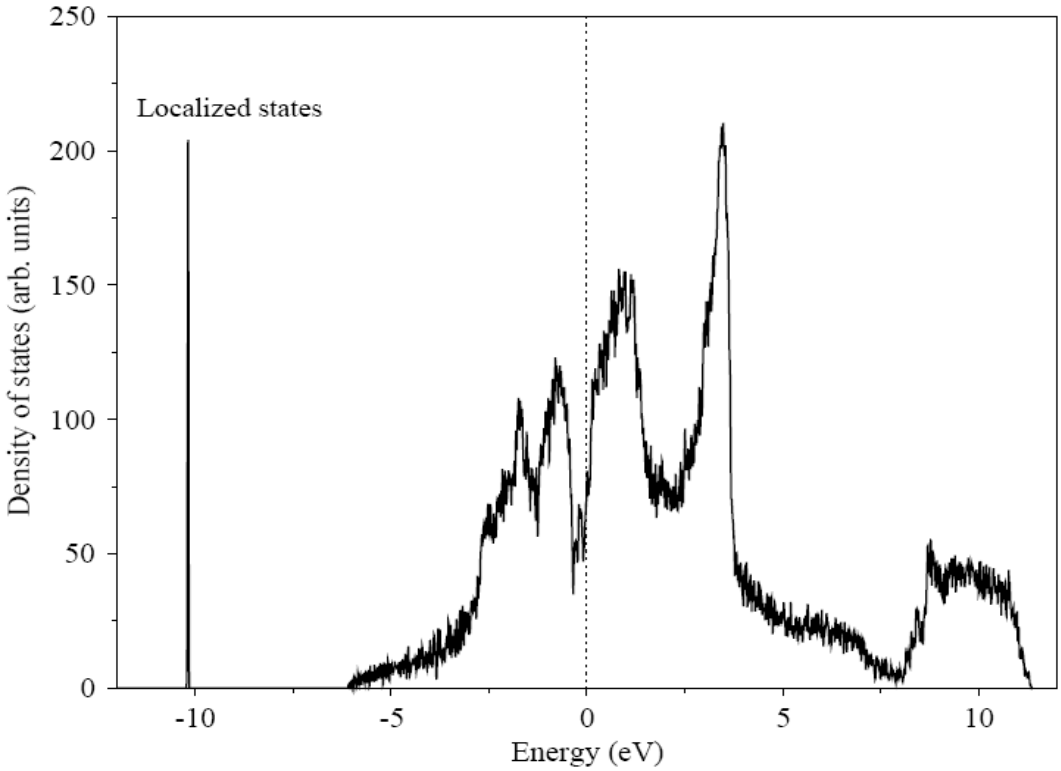

Fig 5.3. Total density of states of the Ti-Kr system, calculated with a supercell containing 64-titanium atomic sites and one krypton impurity atom in the octahedral site. Zero of energy (E =0) is set at the Fermi level.

information contained in the total density of states spanning the whole supercell, local site information in the form of the local density of states (LDOS) may be deduced. Thus, Fig. 5.4 illustrates the LDOS for krypton atom in a relaxed octahedral site and its first nearest neighbour (1nn) titanium atoms. It is evident that the states contained in the 10.1 eV peak corresponds to localization of electrons around the krypton atom and its first nearest neighbour titanium atoms. This is similar to our observation for the krypton atom at a tetrahedral site and its first nearest

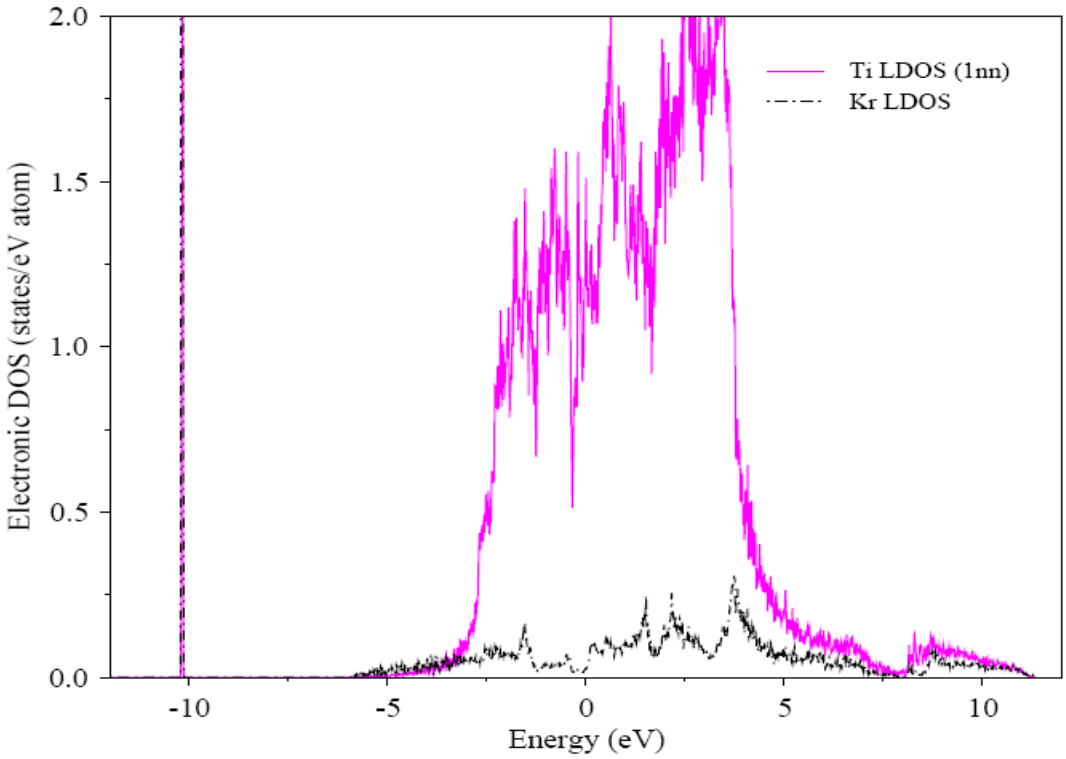

Fig. 5.4. Local density of states (LDOS) for relaxed octahedral krypton atom and its 1nn titanium atoms. The zero of the energy axis is at the Fermi level.

neighbour. In Fig 5.5(a), we present the *d*-projected electronic density of states of nearest neighbour titanium to the krypton impurity atom in octahedral and tetrahedral positions, after atomic relaxation. The *d*-projected density of state for pure titanium is also presented for comparison. Also, in Fig 5.5(b), the *p*-projected DOS of krypton atom at interstitial site is presented to demonstrate the electronic states of krypton defects in titanium. The overall dissimilarity in the shapes of titanium *d*-states and krypton *p*-states suggests that there is no hybridization between these states. Furthermore, as evidenced from Fig 5.5(a), for both interstitial sites, there is a strong modification of pure titanium *d*-states at the Fermi energy, such that as the interstitial configuration changes from the tetrahedral to the octahedral, the DOS increases relative to the DOS of pure titanium. Since krypton is a closed-shell atom, meaning

that bonding with titanium atom is highly unlikely, the distortion of the DOS of the neighbouring metal atoms, when the krypton atom is present in either the octahedral or tetrahedral sites, may serve to indicate its preferred

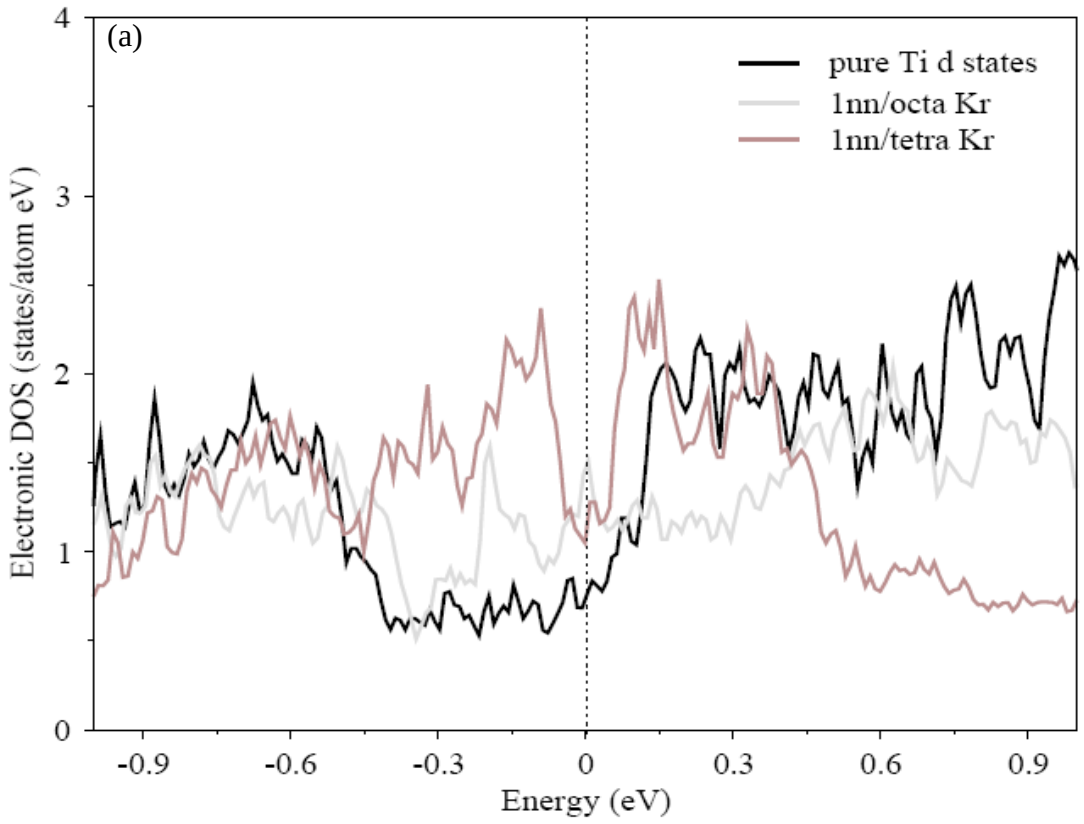

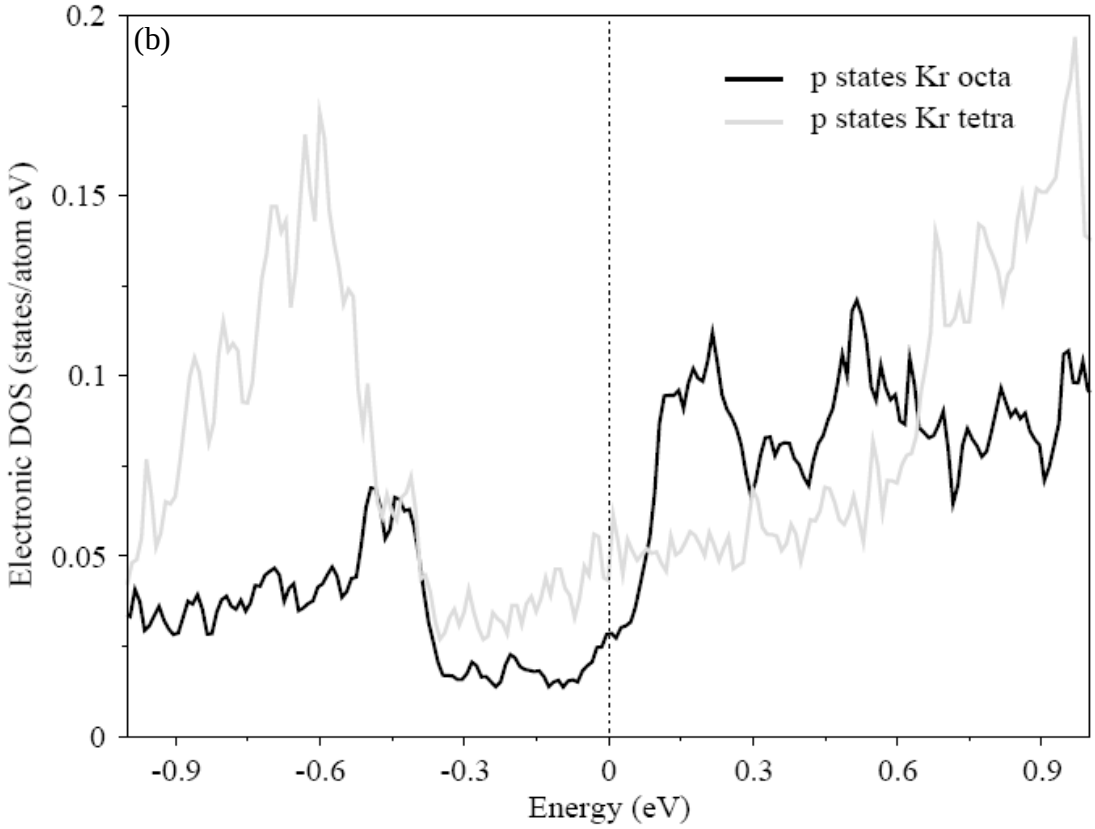

Fig 5.5 (a) Local DOS of titanium atoms. The black line shows the DOS of defect-free titanium. The grey and the dark-grey represent the DOS of metal sites with krypton at the tetrahedral and octahedral positions, respectively. (b) *p*-projected DOS of krypton defect at the tetrahedral site (grey line) and the octahedral site (black line). The zero of the energy axis is at the Fermi level.

sites. The DOS of the nearest neighbour titanium atoms to the octahedral krypton appears to be less distorted (relative to the pure titanium, especially near the Fermi level) compared to the nearest neighbour to the tetrahedral krypton, within the energy range shown in Fig 5.5a. The larger distortion of the DOS at the metals site may correspond to the higher formation energy of the krypton defect, and thus indicates which defect site it preferred when incorporated into titanium structure. In Fig. 5.5(b), it can be seen that the DOS of the tetrahedral krypton is higher than the DOS of the octahedral defect, at the Fermi energy. This effect may have contributed to the overall destabilization of the tetrahedral position. Figs. 5.6 (a) and 5.6 (b) represents maps of

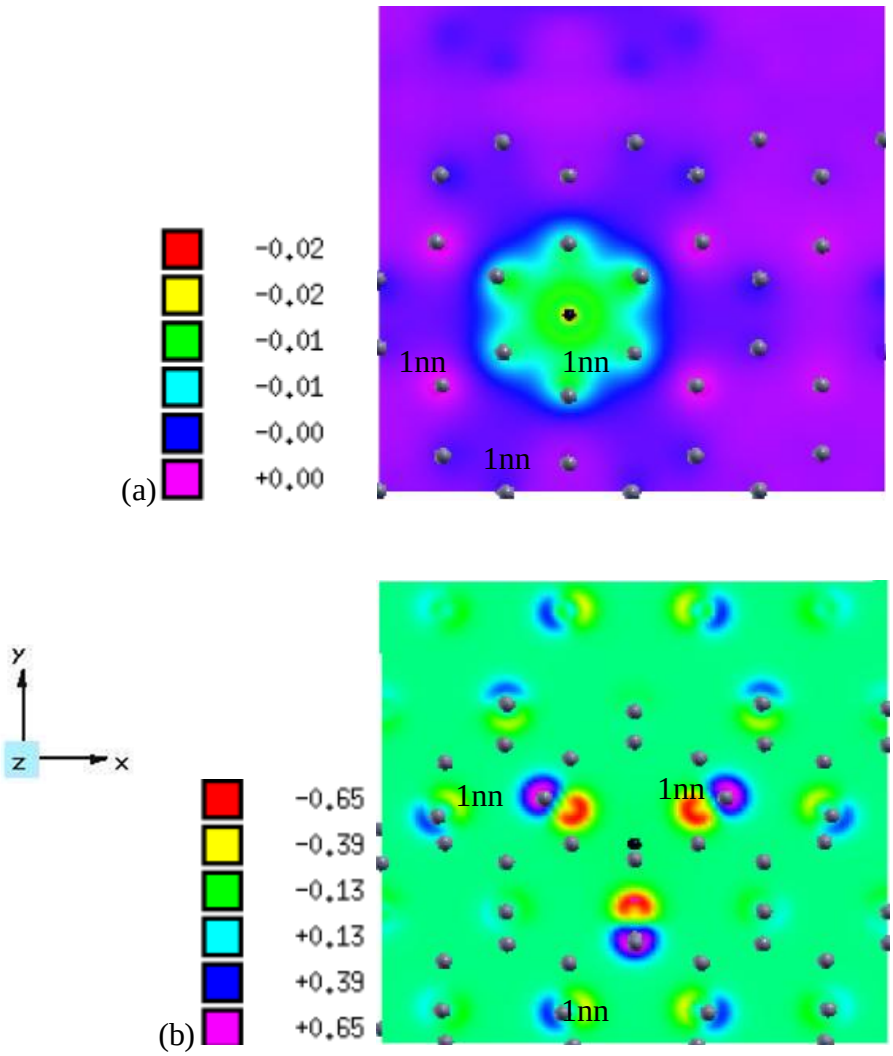

Fig 5.6: The change in the charge density (in electrons/Å^3) of krypton atom (a) insertion into the octahedral site (b) insertion in the tetrahedral site. The grey spheres are the titanium atoms, while the black sphere is the krypton defect.

the electronic density deformation maps (Eqn. 5.5) produced by krypton octahedral and the tetrahedral defects after atomic relaxations. Clearly, titanium atoms become more strongly polarized when the krypton atom is present at the tetrahedral site, in comparison to the octahedral site. In fact, the polarization is negligibly small for the octahedral defect. This strong polarization of the near neighbour titanium atoms in the case of tetrahedral krypton may be responsible for its higher

formation energy, thus making it less energetically favourable than the octahedral krypton. Similar observations have been made for the relative stability of helium defects in iron [42].

5.2.3 Interstitial krypton-vacancy clusters

Fig.5.6 (a) shows the binding energies of a krypton interstitial to small Kr_MV_L clusters, obtained using 64-atom supercell, and a 2 × 2 × 2 *k*-point grid. The energy values have been calculated using Eqns. 5.6 and 5.7(b), and the calculations were performed at constant pressure. The first observation from the graph is that the binding energies of clusters containing only krypton atoms without vacancies), and those containing krypton-vacancy combinations, are all negative i.e., all the interactions are attractive. The krypton binding energies are negative for $m = 2–4$, $n = 0$, suggesting that krypton clusters containing up to four atoms are stable, even without the presence of vacancies. This further implies that, at low temperatures, implanted krypton impurity atoms (at a concentration of 1–6 at. %) are able to form bubbles in an initially vacancy-free matrix. That possible clustering of krypton in titanium may result in bubble formation, and is this is not entirely unexpected. Results from earlier experimental studies [*245,246*] on Cu containing 3.3 at. % krypton atoms, suggest that the injected krypton atoms either exists as submicroscopic bubbles, or in small vacancy-krypton complexes. Another observation from Fig. 5.8(a) is that for a given number of vacancies *n*, when the number of krypton atoms $m \leq n$, the krypton binding energy decreases with increasing krypton content, possibly indicating an increase in cluster pressure as the atoms agglomerate. This is further evidenced in the case of $m \geq 2$, $n = 2$ and $m \geq 2$, $n = 1$.Fig 5.8 (b) shows the binding energies of a vacancy to small krypton–vacancy clusters. The energies have been calculated using Eqns. 5.6 and 5.7(a). First, we note that di-, tri- and tetra-vacancy clusters are stable. The vacancy to cluster binding appears to increase

with increasing krypton content, and the binding is always larger with krypton than without. We may conclude that krypton atoms serve to enhance the stability of vacancy type clusters, possibly by

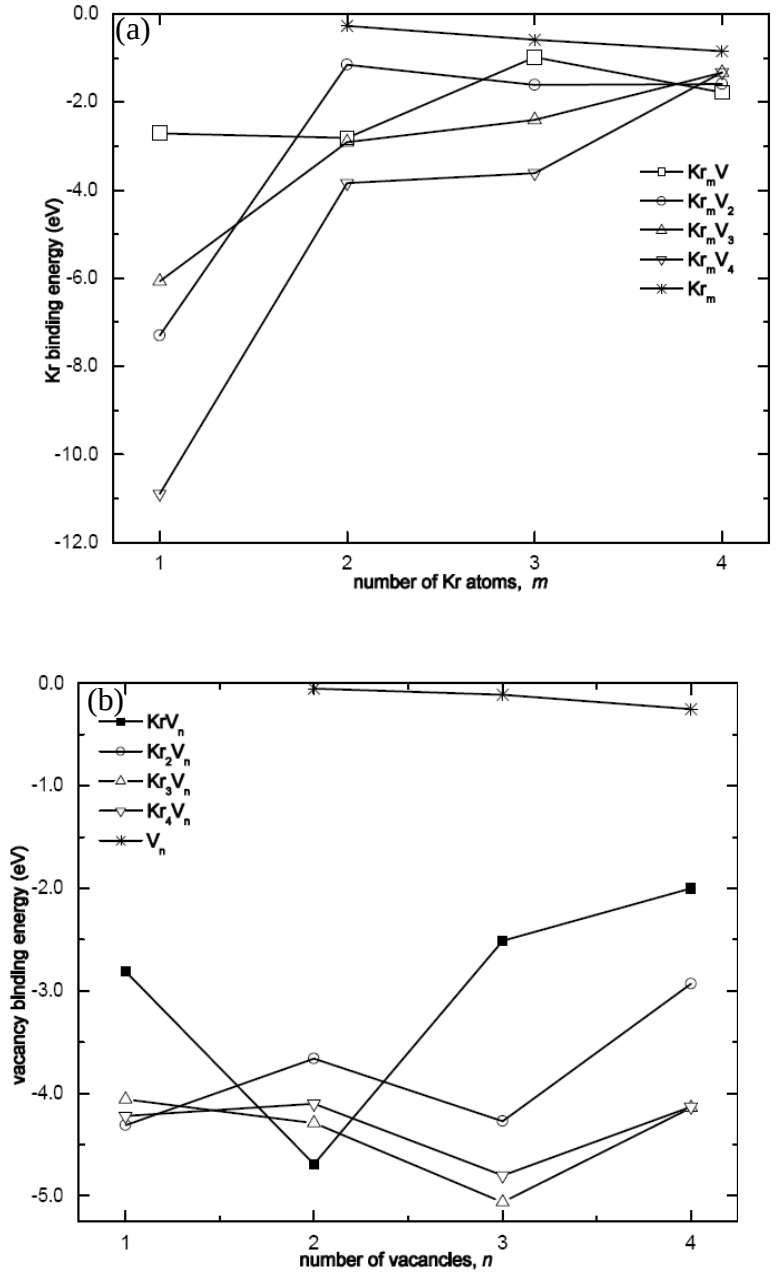

Fig. 5.8. Binding energies of (a) krypton interstitial atom, and (b) a vacancy to $Kr_{m-1}V_n$ and Kr_mV_{n-1} cluster respectively. The legends indicate the composition of the resulting clusters.

reducing vacancy exchange with host lattice atoms. Also, the vacancy binding appears to increase significantly when the relationship between n and m in a Kr_mV_n cluster is such that it may be approximated $-1 \leq n\text{-}m \leq 1$. Then it decreases rapidly when $1 \leq n\text{-}m \leq 3$. The former may corresponds to increasing cluster pressure which favours vacancy to cluster binding, while the latter may indicate decreasing cluster pressure which does not favour vacancy binding.

5.2.4 Substitutional krypton-vacancy clusters

Eighteen different substitutional krypton-vacancy combinations in a titanium lattice have been studied in the present investigation. They are shown in Fig. 5.8(a-i). Simulation cells containing 120 atomic sites, and of size $4a \times 5a \times 3c$ have been used, with $2 \times 2 \times 2$ k-point grid and energy cut-off of 476 eV. The k-point grid is found to be sufficient to converge the total energy. Calculations were carried out at constant volume, that is all the atomic coordinates were relaxed at fixed supercell shape and volume. Defect configurations 1, 3, and 5 (Fig. 5.8a), 8 and 9 (Fig. 5.8b), as well as 10 and 11 (Fig. 5.8c), may be described as *planar* defects, since in each of these cluster configurations, the krypton atoms and vacancies making up the clusters are in the same plane. All of the other defects can be described as *non-planar,* since the defects making up such clusters extend to the planes above and below the (0001) plane. Such are the cases for defects 12 to 18. In the case of configurations 2, 4, 6 and 7, the clusters extend to the plane above the (0001) plane. Defects 15 through 18 are the largest configurations studied. Defect 15 is made up of eleven krypton atoms in substitutional sites arranged in the closest possible way, and it has no vacancy. Defect 16 is similar to 15 except that the central krypton atom in the latter is now replaced with a vacancy in the former. Defects 17 and 18 contain seven and nine vacancies, respectively. In Table 5.2, we summarize the results for the interaction energies (obtained using Eqn. 5.8) for the defects shown in the Fig. 5.8 (a-i). The second and the third

columns list, respectively, the number of vacancy (n_v) and the number of krypton (n_{kr}) atoms making up each of the clusters, while the fourth column gives the interaction energy per krypton atom for each of the defects. The first conclusion to be drawn from the table is that multiple substitutional krypton clusters, without vacancies, are not stable. In addition, the stability of multiple krypton atoms decreases with increasing number of krypton atoms, if there are no neighbouring vacancies.

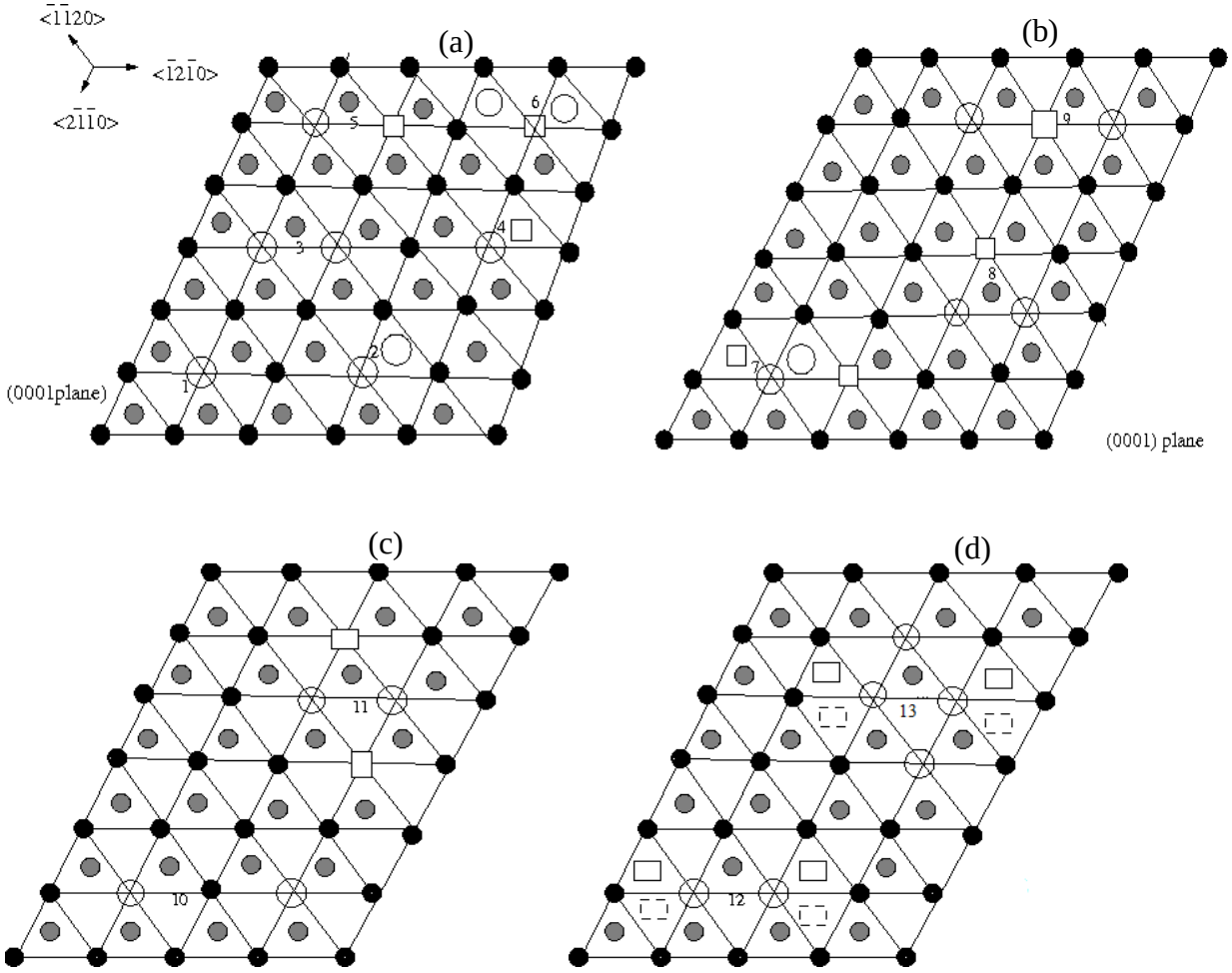

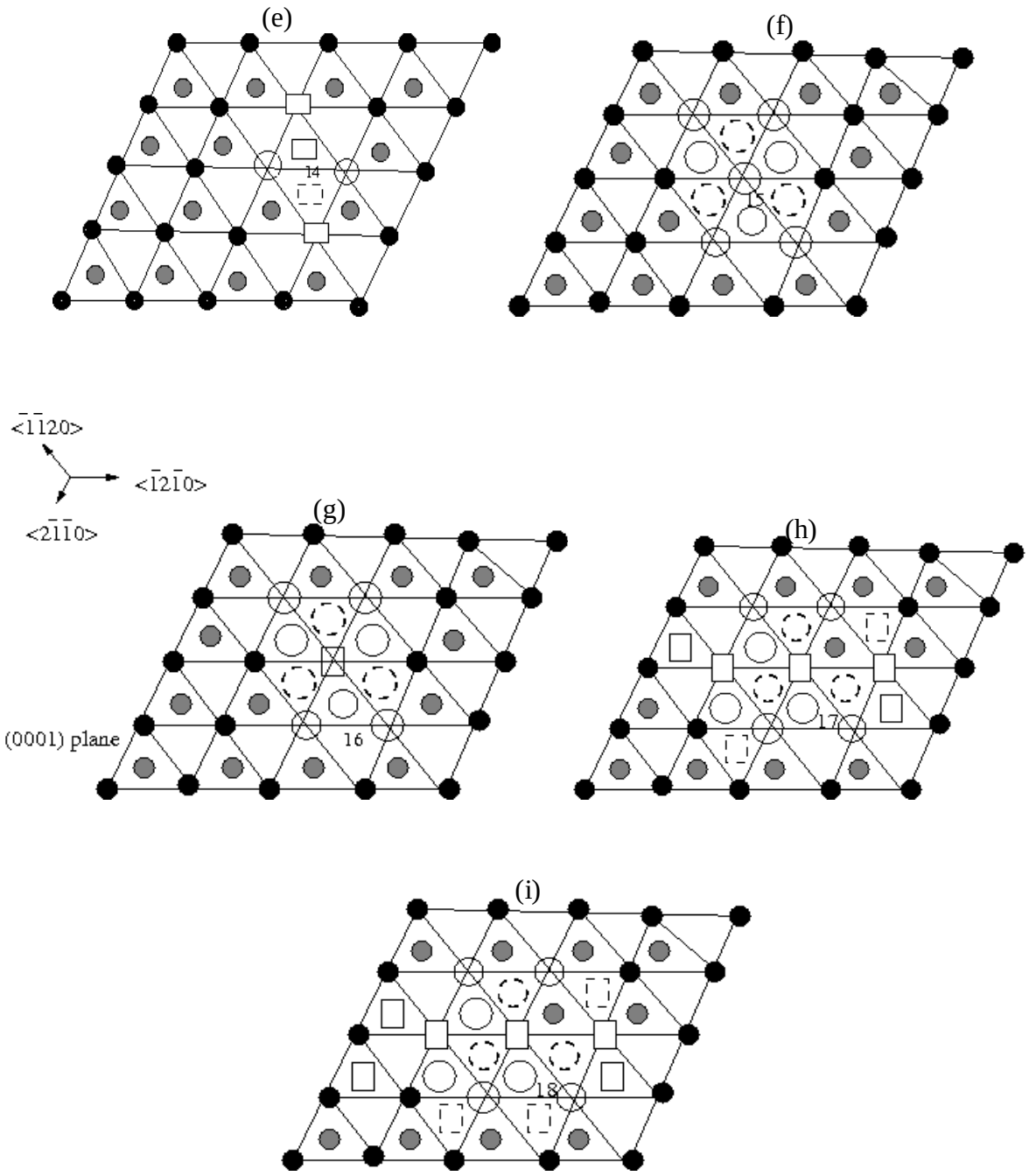

Fig. 5.8. Different combinations of substitutional krypton-vacancy complexes in titanium matrix. Black sphere (●) represents titanium atoms in the (0001) plane, grey sphere (●) represents titanium atoms above the plane, and open spheres (○) represent Kr atoms in substitutional sites. Open broken spheres (◌) represents krypton atoms above the plane. Open (□) and broken (⬚) rectangles, respectively, represent vacancies above and below the plane. The dimensions of the (0001) planes shown are not the one used in the calculations.

This is evident from defect configuration 2, 3, 10, and 15, where the calculated binding energies are all positive. These results are not surprising if one takes into consideration the larger size of krypton

atoms compared to that of titanium [*193*]. The larger krypton atoms introduce strain in the lattice when they substitute for titanium atoms. Increasing number of krypton atoms implies increasing strain and instability, and hence the positive binding energy. Secondly, the presence

Table 5.2. Interaction energy characteristics of vacancy-krypton defect configurations in *alpha*-titanium. n_v, n_{kr}, and $E_{v\text{-}kr}$, respectively represents the number of vacancy, krypton, and their interaction energy. The calculations were done at constant volume using the 120-atom supercell.

Defect	n_v	n_{kr}	$\delta E_{v\text{-}kr}/n_{kr}$ (eV)
1	0	1	-
2	0	2	1.14
3	0	2	1.21
4	1	1	-0.85
5	1	1	-0.93
6	1	2	-0.57
7	2	2	-0.99
8	1	2	-0.40
9	1	2	-0.74
10	0	2	1.63
11	2	2	-1.04
12	4	2	-1.33
13	4	4	-0.72
14	4	2	-2.36
15	0	11	1.24
16	1	10	-0.63
17	7	10	-2.14
18	9	10	-2.60

of vacancies can stabilize the clusters. This is best illustrated in the case of defect configurations 15 and 16, 9 and 10, and configurations 3 and 8. In these cases, the binding energies become negative (indicating stability) on the addition of a single vacancy to the krypton clusters. The influence of vacancies in the cluster is further underlined if defects 11 and 12 are taken into consideration. Here,

for the same number of krypton atoms, doubling the number of vacancies leads to increased binding between the krypton atoms. The same situation occurs in 17 and 18, where increasing the number of vacancies from seven to nine also increases the binding per krypton in the cluster. Thus, we may conclude that the binding energy per krypton atom increases with increasing number of vacancies. This may be explained by a simple physical argument: the presence of vacancies reduces the strain in the lattice and this leads to increased stability of the defect cluster. The third conclusion concerns how the spatial distribution of vacancies affects the binding energy per krypton atom in a defect cluster. For example, defects 12 and 14 have the same krypton configurations and same vacancy to krypton ratio, but the binding energy of defect 14 is almost double that of 12. Also, in defects 11 and 13, the vacancy to krypton ratio is the same, but the value of the binding energy is higher in the latter defect. However, it will be observed that in defect 12, each of the krypton atoms is associated with two vacancies which are located at the closest possible sites, above and below the plane containing the krypton atoms. In defect 14, the two krypton atoms share two vacancies located at closest sites, in addition to each krypton atom having a vacancy in the second nearest neighbour (in the same plane). In defect 13, each of the two krypton atoms (i.e. in $<\bar{1}2\bar{1}0>$ direction) has two vacancies at nearest neighbour sites (above and below the (0001) plane), while the two other krypton atoms are far from the vacancies. In defect 11, however, each of the vacancy is located at the second nearest neighbour to the krypton atom. We summarise the spatial effects as follows: for a given vacancy to krypton ratio in the cluster, greater cluster stability occurs when each vacancy interacts optimally with the krypton atoms. This observation may be understood in terms of strain-relief argument, whereby the strain fields due to krypton atoms are efficiently reduced when there are optimal interactions between the vacancies and the krypton atoms.

5.2.5 Diffusion of interstitial krypton atoms

After finding the most stable interstitial configuration of a krypton impurity atom in titanium, that is, the octahedral site, we examine its migration which is relevant in post-implantation process, such as in clustering of defects to form various complexes. The climbing image nudged elastic band (NEB) method of Jónsson and co-workers [*104,105*], earlier described in section 2.4, was used to locate the minimum energy pathway and the transition state for the diffusion of a krypton impurity atom. Five intermediate images have been used, and the minimum energy path connecting the endpoints is then determined by minimizing the forces on each image to a tolerance of 0.05 eV/Å. Using the relaxed octahedral sites as the endpoints, we investigated two different pathways for krypton migration, consistent with the symmetry of an h.c.p structure. Due to the anisotropy of diffusion in the h.c.p lattice, an octahedral krypton (*O*-site) atom may diffuse along the *c*-axis (out-of-plane), or along the *a*-axis (in-plane) directions, to the next *O*-site. We utilized the optimized supercell geometry consisting of 65 atoms (64 titanium atoms and a krypton atom in the *O*-site) formation energy calculation combined with identical settings for *k*-point sampling and cutoff energy. Figs. 5.7 (a-b) show the minimum energy path (MEP) for krypton atom migration along the *c*- and *a*-axis respectively. The *O*-*O* path along the *c*-axis is such that the diffusing atom squeezes past two titanium atoms in a configuration that may be described as *basal-plane* crowdion. The migration energy barrier E_c^m for this migration is 0.98 eV. However, along the *a*-axis, the *O*-*O* path's migration barrier for this path, E_a^m = 0.58 eV. Similarly to the migration along the *c*-axis, the krypton atom also squeezes past

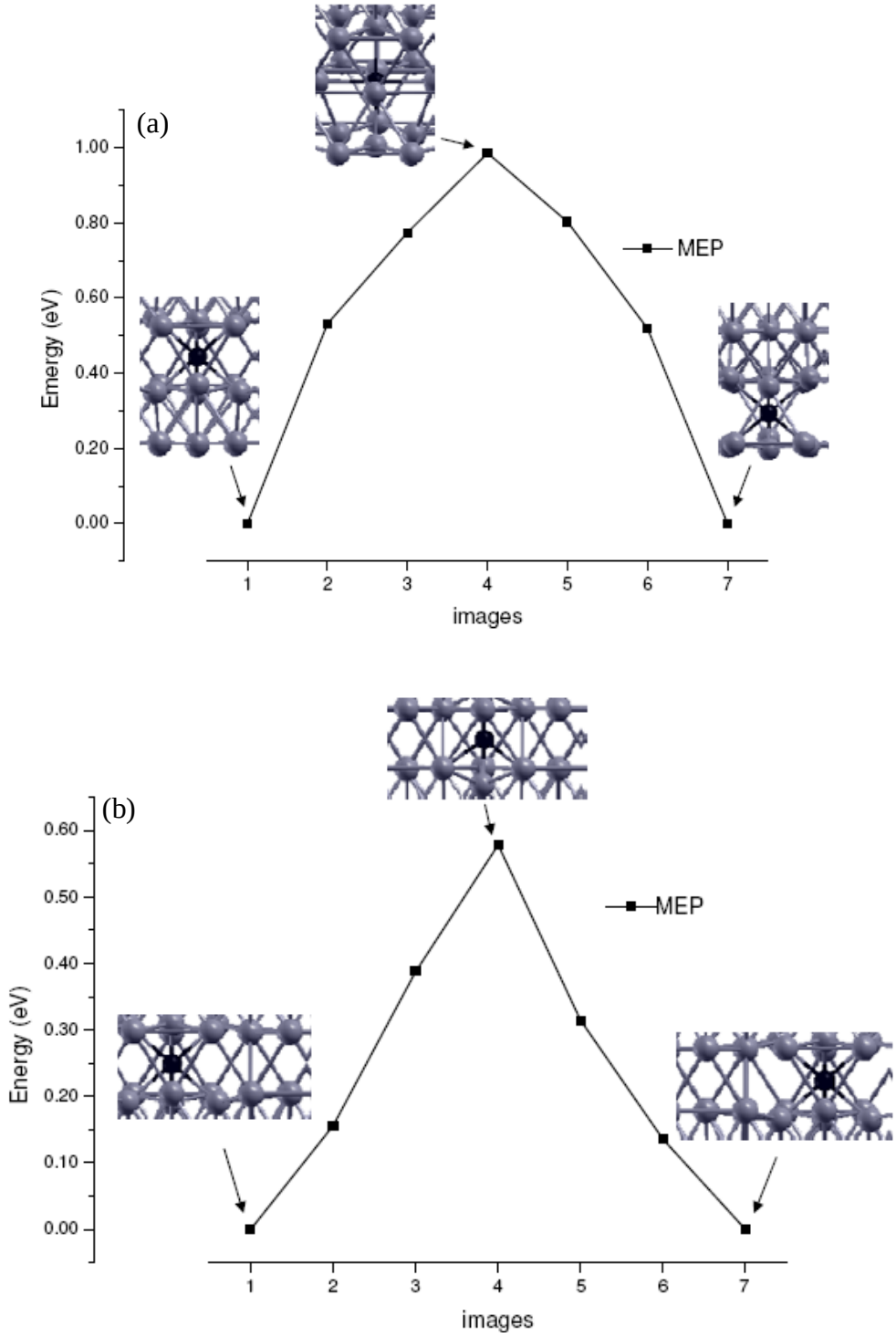

Fig.5.7. Minimum energy path for krypton interstitial migration between two *O*-sites along the (a) *c*-axis (b) *a*-axis, in titanium. The accompanying figures are local structure of the images. Grey spheres represent titanium atoms, while the black sphere is the krypton atom.

through a crowdion configuration, mid-way between two titanium atoms separated by two planes in what may be described as an *off-plane* crowdion configuration. The crowdion configurations thus appear to be the saddle points for krypton impurity diffusion in titanium structure. Further analysis [*247*] will be required to confirm this point.

5.2.6 Diffusion of substitutional krypton atoms

Next, we examine substitutional krypton migration. Substitutional krypton atoms may migrate in titanium via vacancy or dissociation mechanisms. The vacancy mechanism involves the krypton atom exchanging sites with an adjacent vacancy, while the dissociation mechanism involve the krypton atom dissociating from its substitutional lattice position and migrating interstitially until it is trapped in another vacancy. Effective migration energies of substitutional krypton may be estimated depending on the concentration of vacancies in titanium. Of particular relevance is the case of krypton energetically implanted into titanium at low or intermediate temperatures. In this case, implantation-induced vacancies may dominate over thermal vacancies, depending on implantation conditions, such as implanted krypton concentration or the implantation energy. The effective migration energy $E_{eff}^{m,i}(\mathrm{Kr}_{subs})$ for krypton diffusion by dissociation mechanism is given by [*33*]

$$E_{dis}^{m,i}(\mathrm{Kr}_{subs}) = E^{b}(\mathrm{Kr}_{\mathrm{int,}}\mathrm{V}) + E^{m}(\mathrm{Kr}_{\mathrm{int}}), \tag{5.9}$$

that is, the sum of interstitial krypton-vacancy binding $E^{b}(\mathrm{Kr}_{\mathrm{int,}}\mathrm{V})$, and energy barrier for the interstitial krypton migration $E^{m}(\mathrm{Kr}_{\mathrm{int}})$. Using $E^{m}(\mathrm{Kr}_{\mathrm{int}})$ = 0.58eV, $E^{b}(\mathrm{Kr}_{\mathrm{int}},\mathrm{V})$ = 2.71eV and $E_{dis}^{m,i}(\mathrm{Kr}_{subs})$ = 3.29 eV. However, if thermal vacancies prevail, their concentration will be determined

by the vacancy formation energy E_{1v}^{f}. In this case, the effective migration energy by dissociation mechanism, $E_{dis}^{m,t}(\mathrm{Kr}_{subs})$ will be given by [*44*]

$$E_{dis}^{m,t}(\mathrm{Kr}_{subs}) = E^{b}(\mathrm{Kr}_{\mathrm{int}}, \mathrm{V}) + E^{m}(\mathrm{Kr}_{\mathrm{int}}) - E_{1v}^{f} \tag{5.10}$$

with E_{1v}^{f} =1.92 eV, $E_{dis}^{m,t}(\mathrm{Kr}_{subs})$ = 1.37 eV.

We now turn to the migration of substitutional krypton via the vacancy mechanism. This corresponds to a krypton atom previously occupying a vacant lattice position migrating towards another vacancy. We first examine the relaxed configuration of substitutional krypton atom in the presence of first and second neighbour vacancy. This is illustrated using configurations 4 and 5, respectively, in Fig. 5.8a. Defect configuration 4 corresponds to a substitutional krypton in a plane with the vacancy in another plane. Both are separated along the *c*-direction by approximately 2.873Å. In configuration 5, the substitutional krypton atom and the vacancy are in the same plane, and are separated by the lattice parameter *a* = 2.930Å. The vacancy in configurations 4 and 5 thus constitute first and second nearest neighbour to the krypton atom, respectively. After atomic relaxation, configuration 5 is slightly more stable with a negative vacancy to substitutional krypton binding energy of 0.98 eV, compared to 0.85 eV for the configuration 4. The stability of the two configurations (cf. table 5.2) indicates that substitutional krypton can form a substitutional krypton-vacancy pair complex. Concerning the relaxed position of the krypton atom, in the case of configuration 5, it is located at about 0.24 times the distance to the vacancy, while in the case of configuration 4, the krypton atom is located at ~0.19 times the distance to the vacancy. Therefore, in the relaxed krypton-vacancy complex for both configurations, the krypton atom sits asymmetrically between two neighbouring vacant sites.

We now proposed two major routes through which a krypton atom can migrate via the vacancy mechanism, shown in Fig 5.9. The first mechanism is an *in-plane* two-dimensional migration process

(shown in Fig 5.8a), that is, the krypton and the vacancy are located in the same atomic plane. The migration is such that a nearby titanium atom moves towards the vacancy while the krypton atom migrates to occupy the vacant site created by the migrating krypton atom. In this way, the krypton atom has migrated by an atomic distance, within a plane. The second mechanism (Fig 5.8(b)), is an *out-of-plane*, three-dimensional migration process, and is such that the krypton atom migrates to another lattice plane. The titanium atom (located above the plane containing the krypton atom) nearest to the krypton moves to occupy the vacant, while the krypton moves along the *c*-direction to occupy the vacant site left by the titanium atom.

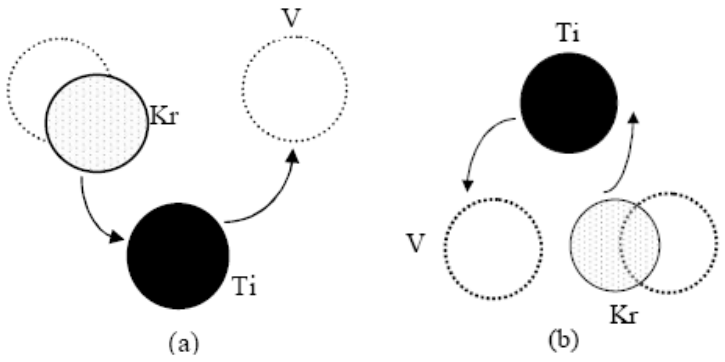

Fig. 5.8. Models showing (a) *in-plane* (top view) (b) *out-of-plane (*side view*)*, Kr-Vacancy (V) migration via vacancy exchange mechanism in the h.c.p. titanium.

The minimum energy paths (MEPs) for the two migration processes have been investigated using the climbing image nudged elastic band method (CI-NEB) [*104,105*]. Supercells containing 63 atomic sites (62 Ti atoms plus a Kr atom), *k*-point grid of 2 × 2 × 2, and cut-off energy of 476 eV were used. It was observed that a denser *k*-point mesh, such as 2 × 2 × 3 does not affect the barrier energy by more than 0.03 eV.

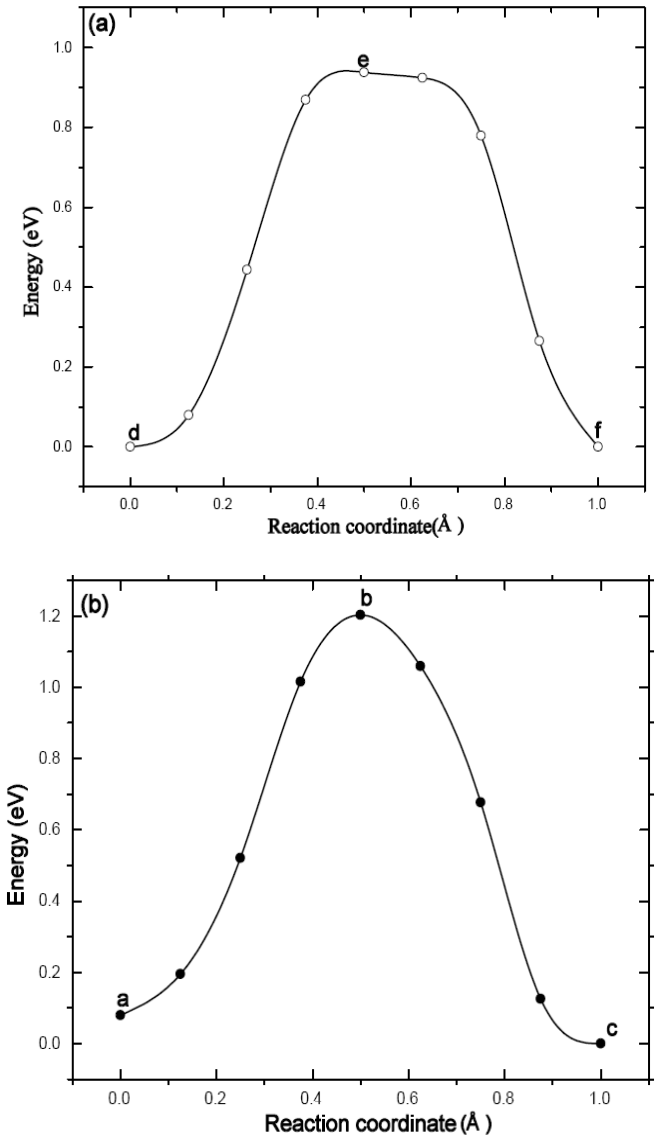

Fig 5.9. Migration barrier for the (a) *in-plane* (b) *out-of-plane*, krypton diffusion via the vacancy mechanism

The MEPs are shown in Fig. 5.9(a-b) and relaxed configurations corresponding to the marked points on the figures are also shown in Fig 5.10(a-f). A total of nine images were used in determining the reaction paths. For the *in-plane* krypton migration, the first (‘*d*’) and the last (‘*f*’’) images are equivalent and correspond to configuration 5 discussed above, hence their energies are equal, as

shown in Fig 5.9*a*. Therefore, in image '*f*'' the diffusing krypton is almost at half the distance between the two vacancies while the migrating titanium atom is already occupying the normal lattice site. For the *out-of-plane* migration, the first and the last images correspond to configuration 5 and 4 respectively, and thus the first image is at slightly lower energy than the last image, as shown in Fig. 5.9*b*. In image '*c*', the diffusing krypton atom is almost at an octahedral position, midway between the vacancies, while the titanium atom is at a regular lattice site. The migration energy barrier for the *in-plane* migration is about 0.94 eV, while for the *out-of-plane* migration, the barrier is about 1.25 eV. These migration energy barriers are lower than the energy required to separate a vacancy from a substitutional krypton-vacancy complex, that is, 1.32 eV or 1.40 eV. The former is estimated from the sum of the vacancy migration energy, i.e. 0.47 eV, and the binding energy of vacancy to substitutional

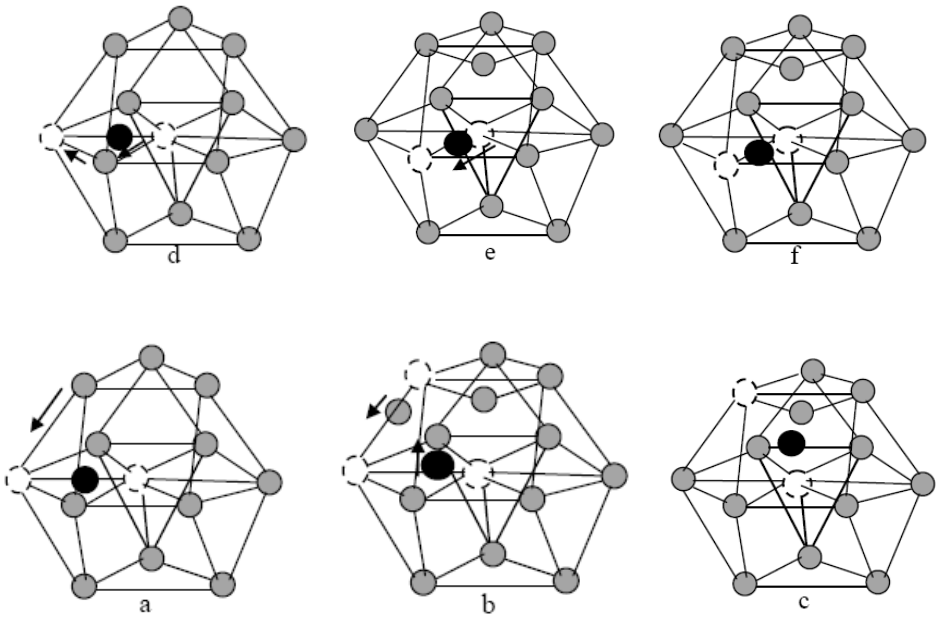

Fig 5.10 Schematics representing the relaxed configurations for the images in the minimum energy path; (d-f) corresponds to images for the in-plane migration, while (a-c) are the images for the out-of-plane migration. Black spheres represent the krypton atoms, grey spheres are the titanium atoms, and the open dotted spheres represent vacancies.

krypton for defect ‘4’ (i.e. 0.85 eV, see Table 5.2). The latter is the sum of the same vacancy migration energy (0.47 eV) and the binding energy of vacancy to substitutional krypton for defect ‘5’ (i.e. 0.93 eV, see Table 5.2). It is therefore expected that the substitutional krypton-vacancy complex is able to migrate over appreciable distance via substitutional krypton-vacancy mechanisms.

The vacancy concentration C_v is thus increased by the amount of krypton-vacancy complexes, the concentration of which may be represented as [*248*]

$$C_v \alpha \exp\{-[E_{1v}^f + E_{\mathrm{KrV,V}}^b]/kT\} \tag{5.11}$$

where E_{1v}^f and $E_{\mathrm{KrV,V}}^b$ are the vacancy formation energy and vacancy-krypton binding energy, respectively. The mobility of krypton-vacancy complex will give rise to an enhanced self-diffusion. It should be mentioned that other impurities atoms such as Fe, Ni, Co and C, which are usually present [*249*], albeit in small quantities, in high purity polycrystalline metals, are fast interstitial diffusers. Therefore, when they form stable vacancy-interstitial impurity complexes, they also contribute to enhanced self-diffusion in the material. The presence of dislocations, twin bands, and other extended defects may result in residual stresses which also enhance self- and foreign impurity defect diffusion [*22,250*]. It should be mentioned however that the direction of migration of defects is dependent on the pre-existing stress profile in the material [*250,251*]. The enhanced diffusion coupled with the low migration barrier energy of divacancy may explain the observed multiple vacancies which form voids beyond the projected range in krypton implanted hcp titanium. The voids introduce additional compressive stress deeper in the titanium sample [*12*]. Furthermore, divacancies may migrate and agglomerate with substitutional krypton-vacancy to form inert gas-filled cavity which may serve as nucleation centres for nanoclusters of krypton atoms.

The effective activation energy for the substitutional krypton migration via the vacancy mechanism, when thermal vacancies dominate, is given by [*252*]

$$\Delta E_{vac}^{m,t}(\mathrm{Kr}_{subs}) = E_v^f - E_{\mathrm{KrV,V}}^b + E_{\mathrm{KrV,V}}^m, \tag{5.12}$$

where $E_{\mathrm{v}}^{\mathrm{f}}$ is the formation energy of a single vacancy, $E_{\mathrm{KrV,V}}^b$ its binding energy to substitutional krypton atom and $E_{\mathrm{KrV,V}}^m$ is the migration energy for this complex. For *in-plane* migration, using E_v^f =1.92 eV, $E_{\mathrm{KrV,V}}^b$ = 0.93 eV and $E_{\mathrm{KrV,V}}^m$ = 0.94 eV, one obtains $\Delta E_{vac}^{m,t}(\mathrm{Kr}_{subs})$ =1.93 eV. For the *out-of-plane* migration, the effective migration energy is higher, i.e. 2.27 eV. However, if implantation induced vacancies prevail, the effective migration barrier for the krypton diffusion via the vacancy mechanism is given by [*252*]

$$\Delta E_{vac}^{m,i}(\mathrm{Kr}_{subs}) = E_{\mathrm{KrV,V}}^m - E_{\mathrm{KrV,V}}^b \tag{5.13}$$

Using $E_{\mathrm{KrV,V}}^m$ =1.25 eV and $E_{\mathrm{KrV,V}}^b$ = 0.85 eV for the *out-of-plane* migration. One obtains $\Delta E_{vac}^{m,i}(\mathrm{Kr}_{subs})$ = 0.40 eV. As for the *in-plane* migration, the effective migration energy is negligible, i.e. $\Delta E_{vac}^{m,i}(\mathrm{Kr}_{subs})$ is ~0.1 eV. If $\Delta E_{vac}^{m,t}(\mathrm{Kr}_{subs})$ = 1.93 eV or 2.27 eV is compared with $\Delta E_{dis}^{m,t}(\mathrm{Kr}_{subs})$ = 1.37eV, we may conclude that if thermal vacancies dominate after implantation, the dissociation mechanism is expected to be dominant. However, if implantation-induced vacancies dominate, the vacancy concentration depends on the initial implantation conditions, and therefore no general conclusion may be drawn. Nevertheless, we may speculate, based on the calculated effective migration energy, $\Delta E_{vac}^{m,i}(\mathrm{Kr}_{subs})$ = 0.35 eV or 0.01 eV and $\Delta E_{dis}^{m,i}(\mathrm{Kr}_{subs})$ = 3.29 eV, that krypton diffusion will proceed via the vacancy mechanism Experimentally, the actual diffusion mechanism governing krypton migration after implantation may be determined from thermal desorption experiments [*253*] or thermal extraction mass-spectrometry [*254*].

CHAPTER 6

Summary and conclusions

Using first-principles electronic structure calculations in the framework of density functional theory (DFT), we have performed computational studies of intrinsic (self) and foreign defect formation, diffusion, and clustering of multiple defects to form complexes in hexagonal closed - packed (h.c.p) titanium. Self-defects that have been studied include the vacancy, divacancy, and the self-interstitial titanium atom, while the foreign defects include incorporated krypton impurity atoms and their combination with vacancy in form of krypton-vacancy complexes. Using the climbing image nudged elastic band method (CI-NEB) as implemented within the DFT, we have investigated the diffusion of vacancy, divacancy, self-interstitial atom, and foreign krypton in titanium. Concerning the kinetics of injected krypton atom in h.c.p titanium, which is relevant in initial stage of post-implantation processes, two types of diffusion mechanisms has been investigated, that is, migration via vacancy diffusion or via dissociation. We have also proposed and investigated possible mechanisms for krypton diffusion in h.c.p titanium under different vacancy concentrations. The major results in this thesis are summarized in the following.

The calculated monovacancy formation energy is in good agreement with other computational studies. However, agreement with the reported experimental data is not very good as the calculated value is much larger. Previous studies have shown that agreement between first-principles calculations of vacancy formation energies and experiment is improved by adding a

correction for the intrinsic surface error, as has been demonstrated for various f.c.c. metals. In our case, and similarly to previous theoretical studies on vacancy formation in h.c.p titanium, the experimental value is already overestimated, and thus surface effects may not result in better agreement with the experiment. This may indicate that the calculations need to be further improved by other theoretical methods.

By calculating the total density of states (DOS) of bulk titanium containing a single vacancy, and comparing with the DOS of a defect free system, a strong peak is observed around the Fermi energy level of the defect system, which is similar to that which has been observed in the study of titanium (0001) surface. This reflects the environment of surface atoms, and may be associated with resonance-like virtual bound states, confirming the internal surface approach for describing vacancies. Nevertheless, we note that such analogy is not without its challenges when density parameters, such as the reduced density gradient and Wigner-Seitz (W-S) radius for bulk closed-packed metals and metallic surfaces is taken into account. For free metallic surfaces, both density parameters increase monotonously toward the vacuum. However, for the bulk metal, the W-S radius increases monotonously towards the centre of the vacancies, whereas the density gradient first increases, reaches a maximum and then falls to zero at the centre of the vacancy.

The low symmetry of the h.c.p lattice is such that two inequivalent migration paths are possible. These are *in-plane* and *off-plane* migration. In the former, the defect migrates along the *a*-direction within an atomic plane, while in the latter, the defect atom migrates along the *c*-direction into another plane. For vacancies, the migration barrier for the two directions differs by ~ 0.15 eV, with the *in-plane* migration having the lower energy barrier. In addition, three divacancy configurations corresponding to first, second and fourth neighbour divacancies have

been studied. It was observed that first and second neighbour divacancies are stable while the fourth neighbour divacancy configuration is not. Furthermore, the migration energy barrier for the two stable divacancy configurations is lower than that of a monovacancy. It may be concluded therefore, that divacancy migration is much faster than single vacancy migration.

Eight configurations of self-interstitials have been examined. The tetrahedral (*T*), basal crowdion (*BC*) and basal tetrahedral (*BT*) are metastable: *T* decays to a split configuration (*S*), while both *BC* and *BT* decay to the basal octahedral (*BO*) configuration. The *BO* and octahedral (*O*) sites appear to be the most stable, and the energy difference between them is small. This small energy difference suggests a possible co-existence of the two configurations. The relative stability is related to structural distortion around the defect: for the most stable configurations the surrounding atoms experience the least structural distortion. This is particularly evidenced in the case of the interstitial at the *O* site. The minimum energy path for the migration of octahedral titanium to a nearest octahedral site (along the *c*-direction) is such that a local minimum exists at the *BO* site. The saddle point appears to be at a site in-between the *O* and *BO* sites. The interstitial atom migration energy barrier is low, i.e. ~ 0.20 eV, compared to 0.47 eV and 0.61 eV for the *in-plane* and *off-plane* vacancy migration, respectively. At this point, the following should be emphasized: the migration energy barrier by the interstitial mechanism in h.c.p titanium is much lower than for the vacancy mechanism. However, self-diffusion in most metals is generally believed to be controlled by the vacancy mechanism at all temperatures. This has been attributed to the fact that equilibrium vacancy concentration is always much larger than the equilibrium interstitial concentration. The predominance of equilibrium vacancy concentration over the interstitial may be explained by the fact that prior has lower formation energy.

Nevertheless, for the h.c.p titanium, the fully relaxed formation energies calculated using 64 atom cell for the interstitial and vacancy are very much close at 1.92 eV and 2.12 eV, respectively. It is therefore possible that self-diffusion may be indeed be dominated by the interstitial mechanism. Recent molecular dynamics studies of self-defects in b.c.c. vanadium [227] predict that self-diffusion may be mediated by interstitial migration. As regards atomic diffusion after ion implantation, self interstitial atoms are produced along with vacancies, and their concentration may be considerably higher than at thermal equilibrium. Thus, in this case, it may not be totally unexpected for self-diffusion to be dominated by self-interstitial atoms.

The krypton impurity locations in titanium have been investigated: two interstitial sites in which the krypton is either located in octahedral (*o*) or in tetrahedral (*t*) positions, and the substitutional site in which the krypton atom occupies a vacant titanium site. Of the interstitials, the *o*-site is found to be the more favourable configuration. However, the substitutional site is the most preferred configuration out of the three sites considered. The relative stability of the interstitial krypton can be understood in term of the free volume available for the krypton atom at the corresponding sites, and the relaxation of the surrounding atoms. For instance, the free volume available at the *o*-site is larger than that of the *t*-site, thereby allowing the krypton atom to fit better than when at the *o*-site. In addition, displacement of the krypton atom, as well as distortions of the surrounding titanium atoms are small. At the *o*-site the krypton atom essentially maintains its initial input configuration, while for relaxation of the *t*-site, the krypton moves completely off from the central position. The relative stability of the krypton atom at the *o*- or *t*-sites can also be understood in terms of underlying electronic density of states (DOS), and the polarization of the neighbouring titanium atoms. For the *o*-site krypton, the DOS of the nearest

neighbour titanium atoms appears to be less distorted (relative to the pure titanium, especially near the Fermi level) compared to the nearest neighbours at the *t*-site. Since krypton is a closed-shell atom, thereby making any hybridization with titanium energetically unfavourable, the larger distortion of the DOS at the metal sites results in corresponding larger formation energy of the *o*-site krypton defect. In addition, at the Fermi energy, the *p* state DOS of the *t*-krypton is higher than that of the *o*-site krypton, an effect that contributes to the instability of the former. Furthermore, neighbouring titanium atoms become more strongly polarized when the krypton atom is present at the *t*-site, in comparison to *o*-krypton where the polarization is negligibly small. This strong polarization of the near neighbour titanium atoms in the case of *t*-krypton is responsible for its higher formation energy, thereby making it less energetically favourable than the *o*-krypton. Interstitial krypton diffusion in h.c.p titanium is anisotropic. An octahedral krypton (*o*-site) atom may diffuse along the *c*-axis (*out-of-plane*), or along the *a*-axis (*in-plane*) directions, to the next *o*-site. The migration energy barrier for the prior migration path is 0.4 eV higher than the later, suggesting that *in-plane* migration is preferred to migration along the *c*-direction. The crowdion configurations appear to be the saddle path for both migrations paths.

We have also showed that defect clusters containing only multiple vacancies or multiple krypton atoms are stable. The stability of the former suggest that implanted krypton impurity atoms (at a concentration of 1–6 at. %) are able to form bubbles in a vacancy-free matrix. Also, small interstitial krypton-vacancy (Kr_nV_m) complexes with $n, m = 1\ldots4$, are a stable in h.c.p titanium. The krypton-vacancy complexes may serve as a nucleation centres for bubble formation, as has been found in similar studies. Furthermore, we determine that greater stability occurs in the krypton-vacancy cluster with fewer vacancies than the krypton atoms, and that krypton atoms

serve to enhance the stability of vacancy type clusters, possibly by reducing vacancy exchange with host lattice atoms. With regards to the stability of substitutional krypton-vacancy clusters, we conclude that multiple substitutional krypton clusters without vacancies, are not stable, and that the stability of multiple krypton atoms decreases with increasing number of krypton atoms, if there are no neighbouring vacancies. Thus, the presence of vacancies serves to stabilize the substitutional krypton clusters. Furthermore, the spatial distribution of vacancies affects the binding energy per krypton atom in a defect cluster. The greatest cluster stability occurs when each vacancy interacts optimally with the krypton atoms. This observation may be understood in terms of strain-relief argument, whereby the strain fields due to krypton atoms are efficiently reduced by interactions with those of vacancies.

As regards the diffusion of krypton atoms after room temperature implantation, based on the consideration of the formation energies, it is logical to assume that most krypton atoms are trapped in vacancies, which means in substitutional positions. Migration may then proceed by two diffusion mechanisms: via the nearby vacancy or dissociation from the substitutional site. The former occurs if substitutional krypton atom becomes mobile by exchanging sites with an adjacent vacancy, while in the latter, the krypton escapes from its substitutional position and migrates interstitially. Effective migration energy barriers have been estimated for the two mechanisms, depending on whether vacancies are present at their thermal equilibrium concentration, or at significantly higher concentration, such as may occur in ion implanted material. We have determined, based on the calculated effective migration energies that, if thermal vacancies prevail, the dissociation mechanism is expected to be dominant. On the other hand, if implantation-induced vacancies dominate, the vacancy concentration depends on the

initial implantation conditions, and therefore no general conclusion may be drawn. Nevertheless, we may speculate, based on the calculated effective migration energy that krypton diffusion will proceed via the vacancy mechanism.

REFERENCES

1. R. E. Stoller and G. R. Odette, *J. Nucl. Mater*. **154**, 286 (1988).

2. T. Seletskaia, Yu. N. Osetsky, R. E. Stoller, and G. M. Stocks, *J. Nucl. Mater*. **351**, 109 (2006).

3. M. Lang, F. Zhang, J. Lian, C. Trautmann, R. Neumann, and R. C. Ewing, *Earth Planet. Sci. Lett.* **269**, 291 (2008).

4. M. Lang, F. Zhang, J. Zhang, J. Wang, B. Schuster, C. Trautmann, R. Neumann, R. Neumann, U. Becker, and R. C. Ewing, *Nat. Mater.* **8**, 793 (2009).

5. S. E. Donnelly and J. H. Evans. (Eds.), *Fundamental Aspects of Inert Gases in Solids* (Plenum Press, New York, 1991).

6. D. J. Bacon and Yu. N. Osetsky, *Mater. Sci. Engrg. A* **365**, 46 (2004).

7. Y. Matsukawa and S. J. Zinkle, *Science*, **318**, 959 (2007).

8. H. Fukushima, M. L. Jenkins, M. A. Kirk, *Phil. Mag. A* **75**, 1583 (1997).

9. K. Nordlund, J. Keinonen, M. Ghaly, and R. S. Averback, *Nature*, **398**, 49 (1999).

10. T. Diaz de la Rubia, G. H. Gilmer, *Phys. Rev. Lett*. **74**, 2507 (1995)

11. M. Ghaly and R. S. Averback, *Phys. Rev. Lett*. **72**, 364 (1994)

12. M. Härting, S. Nsengiyumva, A.T. Raji, G. Dollinger, P. Sperr, S.R. Naidoo, T.E. Derry, C. M. Comrie and D. T. Britton, *Surf. Coat. Tech.* **201**, 8237 (2007).

13. P. Sigmund (Ed.), *Ion beam science*: *Solved and Unsolved Problems* (The Royal Danish Academy of Sciences and Letters, 2006).

14. R. C. Birtcher, S. E. Donnelly, M. Song, K. Furaya, K. Mitsuishi, and C.W. Allen, *Phys. Rev. Lett*. **83**, 1617 (1999).

15. S. E. Donnelly, R.C. Birtcher, C.W. Allen, I. Morrison, K. Furaya, M. Song, K. Mitsuishi, and U. Dahma, *Science*, 296, 507(2002).

16. M. Mitsuishi, M. Kawasaki, M. Takeguchi, and K. Furaya, *Phys. Rev. Lett*. **82**, 3082 (1999).

17. U. Dahmen, S. Q. Xiao, S. Paciornik, E. Johnson, and A. Johansen, *Phys. Rev. Lett*. **78**, 471 (1997).

18. M. Eldrup, B. N. Singh, *J. Nucl. Mater*. **323**, 346 (2003).

19. D.T. Britton, M. Härting, A. Hempel, G. Kögel, P. Sperr, W. Triftshäuser, M. Hempel, D. Knoesen, *J. of Non-Crystalline Sol*. **299–302**, 249 (2002).

20. E. Yagi, Nucl. *Instr. Meth. Phys. Res B*. **39**, 68 (1989).

21. H. H Anderson, J. Bohr, A. Johansen, E. Johnson, L. Sarholt-Kristensen, and V. Surganov, *Phys. Rev. Lett*. **59**, 1589 (1987).

22. M. Härting, M. Yaman, R. Bucher, and D. T Britton, *Adv. Engr. Mater*. **4** (8), 592 (2002).

23. W.K. Liu, E.G. Karpov, S.Zhang, H.S.Park, *Comput. Methods Appl. Mech. Engrg*. **193**, 1529 (2004).

24. J. Hafner, *Acta Mater*. **48**, 71 (2000).

25. G. Lu, E. Kaxiras, *Phys. Rev. Lett*. **94**, 155501(2005).

26. M. Leitner, B. Sepiol, L-M Stadler, B. Pfau, and G. Vogl, *Nature Mater.* **8**, 717 (2009).

27. D. E. Jiang, E. A Carter, *Phys. Rev. B* **67**, 214103 (2003).

28. A. Anderman, W.G. Gehman, *Phys. Stat. Sol*. **30**, 283 (1968).

29. D. E. Rimmer, A. H. Cottrell, *Philos. Mag*. **2**, 1345 (1957).

30. T. Seletskia, Y. N. Osetsky, R. E. Stoller, and G. M. Stocks, *J. Nucl. Mater*. **351**, 109 (2006).

31. F. Willaime, *J. Nucl. Mater*. **323**, 205 (2003).

32. C-C. Fu and F. Willaime, *J. Nucl. Mater*. **367**, 244 (2007).

33. C-C. Fu and F. Willaime, *Phys. Rev.* B **72**, 064117 (2005).

34. S. M. Woodley and R. Catlow, *Nature Mater.* **7**, 937 (2008).

35. C-C. Fu, J. D. Torre, F. Willaime, J-L. Bocquet, and A. Barbu, *Nature Mater.* **4**, 68 (2005).

36. C. Domain and C. S. Becquart, *Phys. Rev. B* **65**, 024103 (2001).

37. C-C. Fu and F. Willaime, *J. Nucl. Mater*, **367-370**, 244 (2007).

38. C-C. Fu, J. D. Torre, F. Willaime, J-L. Bocquet, and A. Barbu, *Nature Mater.* **4**, 68 (2005).

39. T. Diaz de la Rubia, H. M. Zbib, T. A. Khraishi, B. D. Wirth, M. Victoria, and M. J. Caturla, *Nature*, **406**, 871 (2000).

40. W. Kohn and L. J. Sham, *Phys. Rev*. **140**, A1133 (1965).

41. T. Seletskaia, Y. Osetsky, R. E. Stoller, and G. M. Stocks, *Phys. Rev. B* **78**, 134103 (2008).

42. T. Seletskaia, Y. Osetsky, R. E. Stoller, and G. M. Stocks, *Phys. Rev. Lett*. **94**, 046403 (2005).

43. L. Yang, X.T. Zu, and F. Gao, *Physica B* **403**, 2719 (2008).

44. H-Y. Wang, W-J. Zhu, S-J. Liu, Z-F. Song, X-L. Deng, X-R. Chen, and H-L. He, *Nucl. Instr. and Meth. Phys. Res. B* **267**, 849 (2009).

45. C. S. Becquart and C. Domain, *Nucl. Instr. and Meth. Phys. Res. B* **255**, 23 (2007).

46. K. Mitsuishi, M. Kawasaki, M. Takeguchi, and K. Furaya, *Phy. Rev. Lett*. **82**, 3082 (1999).

47. C. W. Allen, R. C. Birtcher, S. E. Donnelly, M. Song, K. Mitsuishi, K. Furaya, and U. Dahmen, *Phil. Mag. Lett*. **83**, 57 (2003).

48. K. Iakoubovskii and K. Mitsuishi, *Phys. Rev. B* **78**, 064105 (2008).

49. A. von Felde, J. Fink, Th. Müller-Heinzerling, J. Pflüger, B. Scheerer, G. Linker, D. Kaletta, *Phys. Rev. Lett*. **53**, 922 (1984).

50. D. L. Smith, P. C. Rice-Evans, D. T. Britton, J. H. Evans, A. Allen, *Phil. Mag. A* **61**, 839 (1990).

51. W. A. Harrison, *Electronic Structure and the Properties of Solids* (Freeman, San Francisco, 1980).

52. H. L. Skriver, *Phys. Rev. B* **31**, 1909 (1985).

53. N. Durand, K. F. Badawi, and Ph. Goudeau, *J. Appl. Phys*. **80**, 502 (1996).

54. M. Harting, S. Nsengiyumva, A.T. Raji, G. Dollinger, P. Sperr, S.R. Naidoo, T.E. Derry, C. M. Comrie and D. T. Britton, *Surf. Coat. Tech.* **201**, 8237 (2007).

55. W. E. Pickett, *Comp. Phys. Rep.* **9**, 115 (1989).

56. R. M. Nieminen in Theory of Defects in Semiconductors, D. A. Drabold, S. K. Estreicher (Eds), *Topics in Applied Physics*, **104**, 29 (2007).

57. R. G. Parr and W. Yang, *Density-Functional Theory of Atoms and Molecules* (Oxford University Press, New York, 1989).

58. M. Levy, *Proc. Natl. Acad. Sci. USA*, **76**, 6062 (1979).

59. H. Hohenberg and W. Kohn, Phys. Rev. Lett. **136**, B864 (1964).

60. D. J. Singh, *Planewaves, Pseudopotentials and the LAPW method* (Kluwer Academic Publishers, 1994).

61. M. Levy, Phys. Rev. A **26**, 1200 (1982).

62. E. H. Lieb, in *Density Functional Methods in Physics*, ed. R. M. Dreizler and J. Da Providencia (Plenum, New York, 1985).

63. W. Kohn and L. J. Sham, *Phys. Rev*. **140**, A1133 (1965).

64. A. Booten and H. van der Vorst, *Comp. Phys.* **10**, 331 (1996).

65. A. P. Seitsonen, M. J. Puska, and R. M. Nieminen, *Phys. Rev. B*, **51**, 14057 (1995).

66. D. Gunnarsson, B. I. Lundqvist, *Phys. Rev. B*, **13**, 4274 (1976).

67. accessible *on http://www.netlib.org/lapack/.*

68. D. Gunnarsson, B. I. Lundqvist, *Phys. Rev. B*, **13**, 4274 (1976).

69. R. K. Nesbet, *Int. J. of Quant. Chem*. **77**, 521 (2000).

70. R. Martin, *Electronic Structure: Basic Theory and Practical Methods* (Cambridge University Press, UK, 2005).

71. R. M. Dreizler, E. K. U. Gross, *Density Functional Theory* (Springer, Berlin, 1990).

72. J. P. Perdew and Y. Wang, *Phys. Rev. B* **451**, 13244 (1992).

73. R. J. Magyar, A. Fleszar, E. K. U. Gross, *Phys. Rev. B* **69**, 04511 (2004).

74. K. Capelle, http://arxiv.org/abs/cond-mat/0211443v5.

75. J. P. Perdew and Y. Wang, *Phys. Rev. B* **33**, 8800 (1986).

76. P. Perdew, in *Electronic Structure of Solids '91*,ed. P. Ziesche and H. Eschrig Akademie (Verlag, Berlin, 1991).

77. M. Levy, *Int. J. Quant. Chem*. **523**, 617 (1989).

78. J. P. Perdew, K. Burke, and M. Ernzerhof, *Phys. Rev. Lett*. **77**, 3865 (1996).

79. C. Filippi, C. J. Umrigar, and M. Taut, J. *Chem. Phys*. **100** (2), 1290 (1984).

80. J. P. Perdew, J. A. Chevary, S. H. Vosko, K. A. Jackson, M. R. Pederson, D. J. Singh, and C. Fiolhais, *Phys. Rev. B* **46**, 6671 (1992); **48**, 4978 (E) (1993).

81. B. Hammer and K.W. Jacobsen, J. K. Nϕrskov, *Phys. Rev. Lett.* **70**, 3971 (1993).

82. B. Hammer and M. Scheffer, *Phys. Rev. Lett*. **74**, 3487 (1995).

83. D. R. Hamann, *Phys. Rev. Lett.* **76**, 660 (1996).

84. R. M. Dreizler and E.K.U. Gross, *Density functional Theory* (Springer, Berlin, 1990).

85. C. Fiolhais, F. Nogueira, and M. A. L. Marques (ed.), *A primer in Density Functional Theory, Vol. 620, of Lecture Notes in Physics.* (Springer, Berlin, 2003).

86. N. W. Ashcroft and N. D. Mermin, *Solid State Physics* (Saunders College Publishing, Philadelphia, 1976).

87. B. Meyer, *Computational Nanoscience: Do it Yourself*, ed. J. Grohendorst, S. Blügel, D. Marx (NIC Series, 31, 71 (2006)).

88. G. P. Francis and M.C. Payne, *J. Phys: Condens. Matt*. **2**, 4395 (1990).

89. D. R. Hamann. M. Schlüter, C. Chiang, *Phys. Rev. Lett*. **43**, 1494 (1976).

90. L. Kleinman, D. M. Bylander, *Phys. Rev. Lett*. **20**, 1425 (1982).

91. X. Gonze, P. Käckell, and M. Scheffler, *Phys. Rev. B* **41**, 12264 (1990).

92. X. Gonze, R. Stumpf, and M. Scheffler, *Phys. Rev. B* **44**, 8503 (1991).

93. D. Vanderbilt, *Phys. Rev. B* **41**, 7892 (1990).

94. S. G. Louie, S. Froyen, and M. L. Cohen, *Phys. Rev. B* **26,** 1738 (1982).

95. A. Pasquarello, K. Laasonen, R. Car, C. Lee, and D. Vanderbilt, Phys. *Rev. Lett.* **69**, 1982 (1992).

96. K. Laasonen, A. Pasquarello, R. Car, C. Lee, and D. Vanderbilt, *Phys. Rev. B* **47**, 10142 (1993).

97. H. J. Monkhorst and J. D. Pack, *Phys. Rev. B* **13**, 5188 (1976).

98. M. Methfessel and A. T. Paxton, *Phys. Rev. B* **40**, 3616 (1989).

99. G. Gilat, *J. Comput. Phys*. **10**, 432 (1972).

100. R. A. Evarestov and V. P. Smirnov, *Phys. Stat. Sol. (b)*, **119**, 9 (1983).

101. A. Dal Corso, in *Quantum-Mechanical Ab-initio Calculation of the Properties of Crystalline Materials*, ed. C. Pisani (Springer-Verlag Berlin Heidelberg, 1996).

102. C. Elsässer, M. Fähnle, C. T. Chan, and K. M. Ho, *Phys. Rev. B* **49**, 3616 (1989).

103. T. S. Chiara, *An introduction to Orthogonal Polynomials* (Gordon and Breach, New York, 1978).

104. G. Henkelman, B. P. Uberuaga, H. Jónsson, *J. Chem. Phys*. **113**, 9901 (2000).

105. G. Henkelman, H. Jónsson, *J. Chem. Phys*. **113**, 9978 (2000).

106. R. Elber and M. Karplus, *Chem. Phys. Lett*. **139**, 375 (1987).

107. R. Czerminski and R. Elber, *Int. J. Quantum Chem*. **24**, 167 (1990).

108. R. Czerminski and R. Elber, *J. Chem. Phys*. **92**, 5580 (1990).

109. D. Sheppard, R. Terrell, G. Henkelman, *J. Chem. Phys.* **128**, 134106 (2008).

110. W. H. Press, S. A. Teukolsky, W. T. Vetterling, and B. P. Flannery, *Numerical Recipes in C: The Art of Scientific Computation*, 2nd ed. (Cambridge University Press, Cambridge, 1992).

111. R. Fletcher, *Practical Methods of Optimization* (John Wiley and Sons, 1987).

112. S. R. Billeter, A. J. Turner, W. Thiel, *Phys. Chem. Chem. Phys*. **2**, 2177 (2000).

113. S. R. Billeter, A. Curioni, and W. Andreoni, *Comp. Mater. Sci*. **27**, 437 (2003).

114. E. F. Koslover and D. J. Wales, *J. Chem. Phys*. **127**, 134102 (2007).

115. S. Trygubenko, D. J. Wales, *J. Chem. Phys*. **120**, 2082 (2004).

116. E. Weinan, W. Ren and E. Vanden-Eijnden, *Phys. Rev. B* **66**, 052301 (2002).

117.B. Peters, A. Heyden, A. Bell, and A. Chakraborty, *J. Chem. Phys*. **120**, 7877 (2004).

118. accessed on: *http://www. quantum-espresso.org*

119. J. Tao, J. P. Perdew, V. N. Staroverov, and G. E. Scuseria, *Phys. Rev. Lett*. **91**, 146401 (2003).

120. A. D. Becke. *J. Chem. Phys*. **98**, 1372 (1993).

121. J. P. Perdew, M. Ernzerhof, and K. Burke, *J. Chem. Phys*. **105**, 9982 (1996).

122. H. Kwee, S. Zhang, and H. Krakauer, *Phys. Rev. Lett*. **100**, 126404 (2008).

123. D. J. Chadi and M. L. Cohen, *Phys. Rev. B* **8**, 5747 (1993).

124. H. J. Monkhorst and J. D. Pack, *Phys. Rev. B* **13**, 5188 (1976).

125. N. Marzari, D. Vanderbilt, A. De Vita and M. C. Payne, *Phys. Rev. Lett*. **82**, 3296 (1999).

126. P. E. Blöchl, O. Jepsen, O. K. Andersen, *Phys. Rev. B* **49**, 16223 (1994).

127. P. Giannozzi, S. Baroni, N. Bonini, M. Calandra, R. Car, C. Cavazzoni, D. Ceresoli, G L. Chiarotti, M. Cococcioni, I. Dabo, A. Dal Corso S. Fabris, G. Fratesi, S. de Gironcoli, R. Gebauer, U. Gerstmann, C. Gougoussis, A. Kokalj, M. Lazzeri, L. Martin-Samos, N. Marzari, F. Mauri, R. Mazzarello, S. Paolini, A. Pasquarello, L. Paulatto, C. Sbraccia, S. Scandolo, G. Sclauzero, A. P. Seitsonen, A. Smogunov, P. Umari, R. M. Wentzcovitch, *J. Phys.: Condens. Mater***. 21**, 395502 (2009).

128. S. Baroni, S. De Gironcoli, A. Dal Corso, and P. Giannozzi, *Rev. Mod. Phys*. **73**, 515, (2001).

129. R. Car. M. Parrinello, *Phys. Rev. Lett*. **55**, 2471 (1985).

130. A. A. Mostofi, J. R. Yates, Y. –S. Lee, I. Souza, D. Vanderbilt, and N. Marzari, *Comp. Phys. Commun.* **178**, 685 (2008).

131. P. G. Partridge, *Metall. Rev*. **118**, 160 (1967).

132.H. Xia, G. Parthasarathy, H. Luo, Y. K. Vohra, and A. L. Ruoff, *Phys. Rev. B*. **42**, 6736 (1990).

133. R. G. Hennig, T. J. Lenosky, D. R. Trinkle, S. P. Rudin, and J. W. Wilkins, *Phys. Rev. B*. **78**, 054121 (2008).

134. K. Joshi, G. Jyoti, S. C. Gupta, and S. K. Sikka, *Phys. Rev. B* **65**, 052106 (2002).

135.Y. Akahama, H. Kawamura, and T. Le Bihan, *Phys. Rev. Lett*. **87**, 275503 (2001).

136. J. C. Jamieson, *Science* **140**, 72 (1963).

137. A. Jayaraman, W. Clement, and G. C. Kennedy, *Phys. Rev*. **131**, 644 (1963).

138. C. Kittel, *Introduction to Solid State Physics* (Wiley, New York, 1976).

139. F.D. Murnaghan, *Proc. Natl. Acad. Sci*. USA **30**, 244, (1944).

140. L. Fast, J. M. Wills, B. Johansson, and O. Eriksson, *Phys. Rev. B*. **51**, 17431 (1995).

141. *Metal Handbook*, p. 10, 8th ed. (America Society of Metals, Cleveland, 1961).

142.J. R. Chelikowsky, C. T. Chan, and S. G. Louie, *Phys. Rev. B* **34**, 6656 (1986).

143.R. M. Welch, E. H. Hygh, *Phys. Rev. B* **9**, 1993 (1974).

144.P. H. Dederichs, H. Schober, and D. J. Sellmyer, in *Phonon states of elements, electron states, and Fermi surface of alloys* (Springer Verlag, 1981).

145. A. T. Raji, Sandro Scandolo, R. Mazzarello, S. Nsengiyumva, M. Härting, *Phil. Mag*. **89 (20)**, 1629(2009).

146. R. B. Tennent Science (ed.) Data Book, (Oliver and Boyd, 1971); C. S. Barrett and T. M. Massalski, *Structure of Metals* (McGraw Hill, New York, 1966).

147.Z.-W. Lu, D. Singh and H. Krakauer, *Phys. Rev. B* **36**, 7335(1987).

148.V. Ozoliņš and M. Körling, *Phys. Rev. B* **48**, 18304(1993).

149.O. Le Bacq, F. Willaime and A. Pasturel, *Phys. Rev. B* **59**, 8508 (1999).

150.Y.K. Vohra and P.T. Spencer, *Phys. Rev. Lett*. **86**, 3068 (2001).

151. D. E. Trinkle, R. G. Hennig, S. G. Srinivasan, D. M. Hatch, M. D. Jones, H. T. Stokes, R. C. Albers and J. W. Wilkins, *Phys. Rev. Lett*. **91**, 025701 (2003).

152. E. S. Fisher and C. J. Renken, *Phys. Rev.* **135**, A482 (1964).

153. N. Benbattouche, G. A. Saunders, E. F. Lambson and W. Honle, *J. Phys. D* **22**, 670, (1989).

154. O. Jepsen, *Phys. Rev. B* **12**, 2988 (1975).

155. P. J. Feibelman, *Phys. Rev. B* **20**, 1433 (1979).

156. E. H. Hygh and R. M. Welch, *Phys. Rev. B* **1**, 2424 (1970).

157. R. M. Welch and E. H. Hygh, *Phys. Rev. B* **9**, 1993 (1974).

158. P. Blaha, K. Schwarz, and P. H. Dederichs, *Phys. Rev. B* **38**, 9368 (1988).

159. G. N. Kamm and J. R. Anderson, *Low Temperature Physics* (Plenum, New York, Vol.4 1974).

160. Y. K. Vohra, S. K. Sikka, and R. Chidambaram, *J. Physics. F. Metal Phys*. **9 (9)**, 1771, (1979).

161. D. E. Eastman, *J. Appl. Phys*. **40**, 1387 (1969).

162. T. Korhonen, M. J. Puska, and R. M. Nieminen, *Phys. Rev. B* **51**, 9526 (1995).

163. K. F. McCarthy, J. A. Nobel, and N. C. Bartlet, *Nature*, **412**, 622 (2001).

164. W. Frank, U. Breier, C. Elsässer, and M. Fähnle, *Phys. Rev. B* **48**, 7676 (1993).

165. C. Domain and A. Legris, *Phil. Mag*. **85**, 569 (2005).

166. K. Nordlund, M. Ghaly, R. S. Averback, M. Caturla, T. Diaz de la Rubia, and J. Tarus, *Phys. Rev. B* **57**, 7556 (1998).

167. M. Wen, C. H. Woo, and H. Huang, *J. Comp. Aided. Mater. Design* **7**, 97 (2000).

168. M. J. Puska, O. Jepsen, O. Gunnarsson, and R. M. Nieminen, *Phys. Rev. B* **34**, 2695 (1986).

169. S. Ögut. H. Kim, and J. R. Chelikowsky, *Phys. Rev. B* **56**, R11353 (1997).

170. P. Söderlind, L. H. Yang, and J. A. Moriarty, *Phys. Rev. B* **61**, 2579 (2000).

171. R. Benedek, L. H. Yang, C. Woodward, B. I. Min, *Phys. Rev. B* **45**, 2607 (1992).

172. B. Puchala, M. L. Falk, and K. Garikipati, *Phys. Rev. B* **77**, 174116 (2008).

173. M. I. J. Probert, M. C. Payne, *Phys. Rev. B* **67**, 075204 (2003).

174. H. Nozaki and S. Itoh, *Phys. Rev. B* **62**, 1390 (2000).

175. P. A. Schultz, *Phys. Rev. B* **60**, 1551 (1999).

176. G. Makov and M.C. Payne, *Phys. Rev. B* **51**, 4014 (1995).

177. D. A. Andersson, and S. I. Simak, *Phys. Rev. B* **70**, 115108 (2004).

178. R. Pawellek, M. Fähnle, C. Elsässer, K-M Ho, and C-T Chan, *J. Phys: Condens. Matter.* **3**, 2451 (1991).

179. W. Frank, U. Breier, C. Elsässer, and M. Fähnle, *Phys. Rev. B* **48**, 7676 (1993).

180. U. Breier, W. Frank, C. Elsässer, M. Fähnle, and A. Seeger, *Phys. Rev. B* **50**, 5928 (1994).

181. J. R. Hardy, *J. Phys. Chem. Solids*, **29**, 2009 (1968).

182. R. A. Johnson and J. R. Beeler, *Point Defects in Titanium*, in Interatomic Potentials and Crystalline Defects, ed. J. K. Lee (AIME, New York, 1981), p. 165

183. A. P. Seitsonen, R. Virkkunen, M. J. Puska, and R. M. Nieminen, *Phys. Rev. B* **49**, 5253 (1994).

184. A. Chroneos, H. Bracht, R. W. Grimes, and B. P. Uberuaga, *Appl. Phys. Lett*. **92**, 172103 (2008).

185. A. M. Monti, Savino E. J, *Phys. Rev. B* **23**, 6494 (1981).

186. E. Steiner, H. Mehrer, and A. Seeger, *Phys. Stat. Sol. (b)* **75**, 361 (1976).

187. V. O. Shestopal, *Sov. Phys. Solid State* **7**, 2798 (1966).

188. E. Hashimoto, E. A. Smirnov, and T. Kino, *J. Phys F: Met. Phys*. **14**, L215 (1984).

189. O. Le Bacq, F. Willaime, and A. Pasturel, *Phys. Rev. B* **59**, 8508 (1999).

190. B. Drittler, M. Weinert, R. Zeller, and P. H. Dederichs, *Solid. State. Comm*. **79**, 31, (1991).

191. D. E. Trinkle, M. D. Jones, R. G. Hennig, S. P. Rudin, R. C. Albers, and J. W. Wilkins, *Phys. Rev. B* **73**, 094123 (2006).

192. G. M. Hood, *J. Nucl. Mater*. **139**, 179 (1986).

193. R. M. Tennet (ed.), *Science Data Book* (Oliver and Boyd, Edinburgh, 1978).

194. K. Carling and G. Wahnström, *Phys. Rev. Lett.* **85**, 3862 (2000).

195. A. Satta, F. Willaime, S. de Gironcoli, *Phys. Rev. B* **57**, 11184 (1998).

196. G. J. Ackland, *Phil. Mag. A* **66**, 917 (1992).

197. P. G. Partridge, *Met. Rev*. **118**, 169 (1967).

198. J. R. Fernández and A. M. Monti, *Phys. Stat. Sol. (b)* **179**, 337 (1993).

199. K. M. Carling, G. Wahnström, T. R. Mattsson, N. Sandberg, and G. Grimvall, *Phys. Rev. B* **67**, 054101 (2003).

200. O. Jepsen and O. K. Anderson, *Solid State Commun*. **9**, 1763 (1971).

201. S-L Weng, E. W. Plummer, and T. Gustafsson, *Phys. Rev. B* **18**, 1718 (1978).

202. M. Posternak, H. Krakauer, A. J. Freeman, and D. D. Koelling, *Phys. Rev. B* **21**, 5601 (1980).

203. P. J. Feibelman, J. A. Appelbaum, and D. R. Hamann, *Phys. Rev. B* **20**, 1433 (1979).

204. J. Friedel, *J. Phys F: Met. Phys*. **3**, 785 (1973).

205. K. Carling, G. Wahnström. T. R. Mattsson, A. E. Mattsson, N. Sandberg, and G. Grimvall, *Phys Rev. Lett*. **85**, 3862 (2000).

206. L. Delczeg, E. K. Delczeg-Czirjak, B. Johansson, and L. Vitos, *Phy. Rev. B* **80**, 205121 (2009).

207. G. M. Hood, H. Zhou, D. Gupta, and R. J. Shultz., J. *Nucl. Mater*. **223**, 122 (1995).

208. R. R. Zope, Y Mishin, *Phys. Rev. B* **68**, 024102 (2003).

209. J. R. Fernández, A. M. Monti, R. C. Pasianot, *J. Nucl. Mater*. **229**, 1 (1996).

210. W. Hu, Z. Zhang, B. Huang, F. Gao, D. J. Bacon, *J. Phys.: Cond. Matter*. **13**, 1193 (2001).

211. C. M. Libanti, S. F. Dyment, *Acta Metall*. **11**, 1263 (1963).

212. M. Köppers, C. Herzig, M. Friesel, Y. Mishin. *Acta Mater*. **45**, 4181 (1997).

213. R. A. Johnson, *Philos. Mag. A* **63**, 865 (1991).

214. C. Domain, C. S. Becquart, *Phys. Rev. B* **71**, 214109 (2004).

215. F. Willaime, A. Satta, M. Nastar, O. Le Bacq, *Int. Jour. Quant. Chem*. **77**, 927 (2000).

216. D. Nguyen-Mahn, A. P. Horsfield and S. L. Dudarev, *Phys. Rev. B* **73**, 020101 (2006).

217. W. Frank, U. Breir, C. Elsässer, M. Fähnle, *Phys. Rev. Lett*. **77**, 518 (1996).

218. D. J. Bacon, *J. Nucl. Mater*. **159**, 176 (1988).

219. D. J. Bacon, *J. Nucl. Mater.* **206**, 249 (1993).

220. A. G. Mikihin, Y. N. Osetsky, and V. G. Kapinos, *Phil. Mag. A* **70**, 25 (1994).

221. M. Igarashi, M. Khantha, and V. Vitek, *Phil. Mag. B* **63**, 603 (1991).

222. D. J. Oh and R. A. Johnson, *J. Mater. Res*. **3**, 471 (1988).

223.R. C. Pasianot and A. M. Monti, *J. Nucl. Mater*. **264**, 198 (1999).

224. F. Willaime and C. Massobrio, *Phys. Rev. B* **43**, 11653 (1999).

225. R. Pichon, E. Bisogni and P. Moser, *Radiat. Eff*. **22**, 173 (1974).

226. R. Pichon, E. Bisogni and P. Moser, *Radiat. Eff*. **22**, 159 (1973).

227. M. I. Mendelev, S. Han, W-j. Son, G. J. Ackland, D. J. Srolovitz, *Phys. Rev. B* **76**, 214105 (2007).

228. accessible on *http://www.quantum-espresso.org/pseudo.php*

229. M. H. F. Sluiter, *Phys. Rev. B* **80**, 220102 (2009).

230.V. J. Keast, S. Harris, and D.K. Smith, *Phys. Rev. B* **80**, 214113 (2009).

231. A. J. Morris, C. J. Pickard, and R. J. Needs, *Phys. Rev. B* **80**, 144112 (2009).

232. T. Seletskaia, Y. Osetsky, R. E. Stoller, and G.M. Stocks, *Phys. Rev. Lett.* **94**, 046403 (2005).

233. D. Simonovic and M.H.F. Sluiter, *Phys. Rev. B* **79**, 054304 (2009).

234. D. Muller, D. J. Singh, J. Silcox, *Phys. Rev. B* **57**, 8181 (1998).

235. A. P. Sutton, *Electronic Structure of Materials* (Clarendon, Oxford, 1993)

236. J. Friedel, *Philos. Mag*. **43**, 153 (1952).

237. D. J. Siegel and J. C. Hamilton, *Phys. Rev. B* **68**, 094105 (2003).

238. L. Yang, X.T. Zu, and F. Gao, *Physica B* **403**, 2719 (2008)

239. K. Morishita, R. Sugano, B.D. Wirth, T. Diaz de la Rubia, *Nucl. Instrum. Meth. Phys. Res.* **B** 202, 76 (2003).

240. P. G. Silvestrelli, *Phys. Rev. Lett.* **100**, 053002 (2008).

241. A.T. Raji, S. Scandolo, R. Mazzarello, S. Nsengiyumva, M. Härting and D.T. Britton, *Nucl. Instrum. and Meth. Phys. Res.* **B** 267, 2991 (2009).

242. accessed on *http://www.webelements.com/krypton/atom_sizes.html*.

243. D. L. Smith, P.C. Rice-Evans, and D. T. Britton, *Phil. Mag. A*. **61** (6), 839 (1990).

244. E. Yagi, *Phy. Rev. Lett.* **67**, 3804 (1991).

245. M. Eldrup and J. H. Evans, *J. Phys. F: Met. Phys* **12**, 1265 (1982).

246. K. O. Jensen, M. Eldrup, N. J. Pedersen, and J. H. Evans, J. *Phys. F: Met. Phys*. **18**, 1703 (1988).

247. D. E. Jiang and E. A. Carter, *Phys. Rev. B* **70**, 064102 (2004).

248. C. Herzig, Y. Mishin, and M. Divinski, *Met. Mater. Tran.* **33A**, 765 (2002).

249. M. Behar, F. Dyment, R. A. Perez, J. H. R. Dos Santos, R. L. Maltez, and E. J. Savino, *Phil. Mag. A* **63 (5)**, 967 (1991).

250.W.G. Wolfer and M. Ashkin, *Scripta Met*. **7**, 1175 (1973)

251. D.T. Britton and M. Harting, Adv. Eng. Mater. **4**, 629 (2002).

252. V. Sciani and P. Jung, *Rad. Eff.* **78**, 87 (1983).

253. R. Vassen, H. Trinkaus, and P. Jung, *Phys. Rev. B* **44**, 4206 (1991).

254. K. Takaishi, T. Kikuchi, K. Furuya, I. Hashimoto, H. Yamaguchi, E. Yagi, and M. Iwaki, *Phys. Stat. Sol.(a)* **95**, 135 (1986).

Acknowledgments

My intellectual debts are to the following people and institutions: my supervisors, Professors David Britton and Margit Härting who planted the ideas, set the level for aspirations, provided the financial supports, and showed unwavering belief in my ability, even when I started to doubt myself; Prof. Sandro Scandolo for making the CINECA high-performance computer facilities accessible and for his guidance in making my research ideas come to fruition; Prof. Dr. Riccardo Mazzarello for always making himself available to help with the nitty-gritty of most of the computations; the University of Cape Town (UCT) and the Department of Physics for providing me with the opportunity to pursue the research as a post-graduate student, and for sponsoring my travels to conferences; the National Institute for Theoretical Physics (NITheP) for the bursary awards; and the Abdus Salam International Centre for Theoretical Physics (ICTP) for the award of sandwich training programme fellowships. I am also indebted to my colleagues at the Solid State and Materials Physics Research Group who through their dedication and brilliance have provided a stimulating, vibrant and challenging research environment. Appreciation is due to other academic and non-academic members of staff of the Department of Physics of the UCT. My eternal appreciation goes to my father, Alhaji Abbass Afolabi Raji, who inspired, encouraged and made available his life savings for me to pursue postgraduate studies. Only Allah (SWT) can sufficiently reward him. I am deeply grateful to my mother, Mrs. Aolat Oluremi Raji, for her prayers, patience and perseverance. No man has been given a better woman as a mother. To my wife and my '*jewel of inestimable value*'; Olabisi, my children; Naeemah, Nasir-Llah and Mariam, may Allah (SWT) favours you all above many of His creations, in all circumstances. Thanks for your patience, endurance and prayers. Your supports are invaluable. Inshallah, you shall all live long to be great citizens and sources of blessings to your respective communities.

Thank you for evaluating AnyBizSoft PDF Merger! To remove this page, please register your program!

Go to Purchase Now>>

AnyBizSoft

PDF Merger

- ✓ Merge multiple PDF files into one
- ✓ Select page range of PDF to merge
- ✓ Select specific page(s) to merge
- ✓ Extract page(s) from different PDF files and merge into one